UNIVERSITÀ DEGLI STUDI DI MILANO

SCUOLA DI DOTTORATO DI RICERCA IN SCIENZE BIOCHIMICHE, NUTRIZIONALI E METABOLICHE

DOTTORATO DI RICERCA IN BIOCHIMICA
CICLO XXIII

TESI DI DOTTORATO DI RICERCA

STRUCTURE-FUNCTION STUDIES OF NOVEL MEDICALLY-RELEVANT FLAVOENZYMES

DANIELA ZUCCHINI

Matricola R07793

TUTOR: Prof. MARIA ANTONIETTA VANONI

ANNO ACCADEMICO 2009/2010

ABSTRACT

Flavoproteins are involved in a wide range of biological processes, with a variety of catalytic reactions performed, which range from typical redox catalyses such as the dehydrogenation of an amino acid, or activation of dioxygen, to photochemistry; from DNA damage repair to light emission. Recently, genomics trascriptomic and proteomic approaches led to the identification of new flavoproteins playing a key role in the metabolism of many organisms. Several of these new enzymes are involved in fundamental processes, such as cellular differentiation, apoptosis, protein folding and pathologies. The production and biochemical characterization of two medically-relevant flavoenzymes will be discussed. In a last section we will address a combined computational and experimental study on flavocytochrome b2, a well-characterised flavoenzyme, whose catalytic mechanism is stillat the center of a lively debate.

Seladin-1/DHCR24 is a novel antiapoptotic factor, whose expression levels vary in neurons susceptible of degeneration typical of Alzheimer disease, in certain cancer cell lines and during differentiation. Seladin-1 was shown to be identical to the putative human 3-β-hydroxysterol Δ^{24} reductase (DHCR24), the mutations of which are associated with desmosterolosis, a severe recessive disease that causes multiple congenital anomalies and mental development delays. Sequence analyses and activity assays in whole cell extracts suggested that Seladin-1/DHCR24 may be a FAD-containing NADPH-dependent enzyme that catalyzes the last step of cholesterol biosynthesis from desmosterol. To provide key information for the interpretation of the biological role of the protein, a project aiming to overproduce, purify Seladin-1/DHCR24 was initiated as a prelude to its biochemical characterization. However, in spite of efforts, none of the constructs for protein production in *E. coli* or *S. cerevisiae* cells we generated so far led to protein forms suitable for purification. On the contrary, several forms of the N-terminal putative FAD-dependent monooxygenase domain of MICAL (from the Macromolecule Interacting with CasL) have been produced in *E.coli* and were purified to homogeneity in a stable form and in quantities sufficient to initiate its biochemical characterization. MICAL indicates a family of multidomain proteins involved in the transduction of signals initiated by semaphorins that result in cytoskeletal rearrangements linked to axon steering, cell-cell junctions formation, cell migration and vesicular trafficking by interacting with a number of proteins critical for signaling events to the cytoskeleton. The N-terminal monoxygenase-like domain (MICAL-MO), structurally similar to p-hydroxybenzoate hydroxylase (PHBH), the prototype of FAD-containing monooxygenases, has been shown to be essential for MICAL function, but its catalytic activity has not been defined yet. At variance with PHBH, MICAL-MO exhibits a detectable NADPH oxidase activity. The rate of the overall reaction is fully determined by that of enzyme reduction by NADPH, which takes place

at 25°C and pH 7.0 without detection of spectroscopically distinguishable intermediates. However, MICAL shares with enzymes of the PHBH family NADPH binding the high sensitivity to the ionic strength of the medium and to specific anions suggesting that NADPH binding is governed by electrostatics. Solvent viscosity effects revealed the presence of conformational changes taking place during the catalytic cycle, another property shared with enzymes of the PHBH family that avoid waste of reducing power and release of reactive oxygen species through conformational changes triggered by the redox state of the flavin cofactor and binding of the substrate to be hydroxylated. The search of the physiological activity of MICAL-MO has been initiated by studying its reactivity with actin. We here confirm the proposal that MICAL promotes depolymerization of actin filaments and present preliminary data that support the hypothesis that MICAL may use actin as its second substrate.

Flavocytochrome b2 (Fcb2) is the prototype of a family of α-hydroxyacid dehydrogenases, composed by enzymes supposed to share a common mechanism for the oxidation of the substrate in the enzyme reductive half reaction. Computational studies were carried out to contribute to the understanding of the mechanism of substrate dehydrogenation, which is still debated. These studies demonstrated that lactate oxidation takes place with direct transfer of L-lactate αH to the FMN N(5) position as a hydride anion, as opposed to a two step mechanism that implies α-OH hydrogen abstraction (as a proton) by the active site H373 followed by two-electron transfer to the flavin. The same studies revealed the presence of a water molecule (Wat609), conserved in all enzymes of the Fcb2 family and belonging to third shell residues, which may modulate the acid-base properties of the catalytic residue H373, through a Ser371-Wat609-Asp282-His373 hydrogen bond network.. To experimentally test this hypothesis we produced S371A variants of the isolated flavo-dehydrogenase domain as well as of the full-length enzyme. As previously observed for other Fcb2 active site mutants, the S/A substitution clearly impaired protein folding preventing FMN insertion into the isolated flavoprotein domain and allowing us to obtain partially flavinylated full-length forms. Kinetic experiments on full length enzymes demonstrated that the S/A substitution led to a 20-fold decrease of k_{cat} completely attributable to a decrease of the rate of enzyme reductive half reaction, a 10-fold increase of the value of the dissociation constant of the enzyme-sulfite complex but the pH profile and the K_m(K_d) for L-lactate were unchanged. Although we cannot rule out that the observed effects of the S/A substitution are due to a change of the overall geometry of the active site, the results are fully consistent with the prediction made through computational studies that removal of Wat609 through the S/A substitution lowers the H373 proton affinity in the reduced enzyme impairing lactate oxidation and concomitant flavin reduction.

1. FLAVOPROTEINS

Flavoproteins are involved in a wide range of biological processes, with a variety of catalytic reactions performed, which range from typical redox catalyses such as the dehydrogenation of an amino acid, or activation of dioxygen, to photochemistry; from DNA damage repair to light emission (Figure 1.1). This variety of reactions is due to the extraordinary chemical versatility of their flavin cofactors, that are typically non-covalently bound to the apoprotein. The chemistry of the flavin is restricted to the amphipathic isoalloxazine nucleus, a tricyclic ring system formed by the fusion of the hydrophobic dimethylbenzene moiety with the hydrophilic pyrimidine ring (Fraaije and Mattevi, 2000). This group can exists in an oxidized state and in a fully reduced one (Figure 1.2, Ghisla and Massey, 1989). Reduction of the flavin occurs reversibly by two one-electron steps, ore one two-electron step and the redox potential for the two-electron reduction is around -200 mV. However, this value can greatly vary in flavoenzymes, spanning a range from approximately -400 mV and + 600 mV (Fraajie and Mattevi, 2000). The isoalloxazine ring present also side-chain functions that are not involved in the catalysis, but serve in anchoring the coenzyme at the active site. In some flavoenzymes the isoalloxazine ring of the falvin is covalently linked to a His, Cys or Tyr residue of the polypeptide chain. This attachment is an autocatalytic process that might be beneficial for saturating the active site, cofactor economy, protein stability, preventing flavin modification and inactivation, facilitating electron transfer, oxygen reactivity and tuning the flavin redox potential (Joosten and van Berkel, 2007). In agreement with the beneficial effects of the covalent binding of flavin cofactor to flavoenzymes is the increasing number of oxidoreductases of the vanillyl-alcohol oxidase (VAO) family (Fraaije et al, 1998; Leferink et al, 2008). Members of this family share a conserved flavin-binding domain that favours the covalent attachment of the cofactor.

Three types of flavin cofactors exist in flavoproteins: the riboflavin, or vitamin B2, which contains a ribityl chain at the N^{10} of the isoalloxazine group, and its derivatives flavin mononucleotide (FMN), and flavin adenine dinucleotide (FAD). The phosphorylation in ester linkage at the terminal hydroxyl group of the ribityl side chain of riboflavin leads to the formation of FMN, and the reaction is catalyzed by riboflavin kinase. The adenylation of FMN by FAD synthetase leads to the FAD molecule (Figure 1.2).

As already mentioned, flavins can participate in one-electron transfer reactions, which automatically implies the existence of semiquinone oxidation states. In free solution, i.e. when not enzyme-bound, a mixture of oxidized and reduced flavin very rapidly sets up an equilibrium in which a certain amount of flavin radical is formed. This equilibrium is very much to the left, so that

only about 5% radical is stabilized in an equimolar mixture of oxidized and reduced flavin (Figure 1.4 panel A, Massey, 2000). The semiquinone can exist in a neutral or an anionic form (Figure 1.3). On binding to a specific protein, this equilibrium can change dramatically. Some enzymes show essentially no stabilization of semiquinone, while others give almost 100% stabilization. Flavins show a typical absorption spectrum between 300 nm and 700 nm, with maxima at 380 nm and 450 nm for the oxidized flavin. The various flavin oxidation states show large spectral differences (Figure 1.3, Massey, 2000) that are influenced also by the solvent and the protein environment. Thus, it is possible to monitor the events occurring in catalyses using the flavin itself as a reporter. The anionic form can be stabilized by the presence of positive charge conserved residues at the flavin binding site, such as Lys and Arg, or by the N-terminus of an α helix or a cluster of peptides nitrogens (Fraajie and Mattevi, 2000).

All flavoprotein reactions involve two separate half-reactions (Figure 1.4 panel B, Massey, 2000). The majority of flavoprotein-reducing substrates are dehydrogenated in a two-electron reduction step. The resulting reduced flavin is then re-oxidized by its oxidizing substrate, either in a two-electron step, as shown in Figure 1.4, or in single one-electron steps, in which the flavin semiquinone would be observed as an intermediate. In some enzymes, molecular oxygen is the physiological substrate. Figure 1.4 panel C (Massey, 2000) shows the chemical reactions that occur in the reaction of reduced flavin with oxygen. The initial reaction is a one-electron reduction of O_2 by the reduced flavin (I) to yield a caged radical pair of neutral flavin radical and superoxide (II). This radical pair can collapse into a flavin C4a-peroxide (IV), a nucleophile, which on protonation becomes the electrophilic hydroperoxide (V). The peroxide species may eliminate hydrogen peroxide to yield oxidized flavin (VI), or there may be a second electron transfer from the radical pair (II) to give the same products (VI). The third alternative route is the dissociation of the radical pair into its components, flavin radical and superoxide (III).

Several attempts have been made to achieve a rational classification of the different types of flavoproteins, depending on the type of chemical reactions catalyzed, the nature of the reducing and oxidizing substrates, the physicochemical properties of the enzymes and, more recently, their structural motifs as determined by X-ray crystallography. None of these attempts has been entirely satisfactory. Nevertheless, it is clear that enzymes catalyzing similar chemical reactions tend to have common characteristics which are particular to that group.

Simple flavoproteins are conveniently classified on the basis of the reactivity of the reduced enzyme with molecular oxygen. The oxidases, such as D-amino acid oxidase, glucose oxidase, glycolate oxidase, react very rapidly with O_2 to yield H_2O_2 and oxidized flavoprotein in what appears to be a simple second-order process without observable intermediates (Massey, 1995). Hydrogen peroxide

produced is very useful in diagnostic and food applications and for the high-throughput selection of improved enzyme variants produced by laboratory evolution (Joosten and van Berkel, 2007).

The second class of simple flavoproteins is characterized by flavoprotein monooxygenases. The reduced enzyme reacts with O_2 to form readily observable flavin C4a hydroperoxide intermediates (Figure 1.4 and Figure 1.5). With all enzymes of this class the physiological reductant is NADH or NADPH. In the absence of further substrate, the flavin hydroperoxide decays non-productively to H_2O_2 and oxidiezed flavin. However, in the presence of the physiological substrate the flavin hydroperoxide reacts to transfer an oxygen atom to the substrate, resulting in a C4a-hydroxyflavin, which upon dehydration returns the flavin to its oxidized state for the next catalytic cycle (Figure 1.5 and Figure 3.1.4). Based on fold and function, a reclassification of monooxygenases into six subfamilies (A-F) has been proposed (Table 1.1; Joosten and van Berkel, 2007; van Berkel et al, 2006). p-hydroxybenzoate hydroxylase is the prototype of class A, where the aromatic substrate is hydroxylated at the position ortho to the activating para-substituent. This enzyme is the most thoroughly studied mechanistically and work from two separate groups has presented evidence for substantial movement of the flavin within the protein during catalysis (Chapter 3).

Enzymes of the electron transferases class are all involved in single-electron transfers, e.g. flavodoxin, ferredoxin-$NADP^+$ reductase and NADPH-cytochrome P-450 reductase. These enzymes all react sluggishly with O_2 and in the process produce O_2^- and the flavin semiquinone. This is somewhat unsatisfactory categorization, since many enzymes that function in one-electron transfers also dehydrogenate an organic substrate. This is the case of acyl-CoA dehydrogenases, whose reaction with the acyl-CoA substrate involves the formation of an unsaturated C=C structure by concerted proton abstraction from the substrate α-carbon to the flavin N(5) (Massey, 2000).

Finally, there are flavoproteins containing auxiliary redox centers, as flavoprotein disulfite reductases, metal-containing flavoproteins and heme-containing flavoporteins. The best-known example of the latter class is yeast lactate dehydrogenase (flavocytochrome b2), the prototype of a family of enzymes catalyzing the oxidation of α-hydroxy acids to α-keto acids. Components of this extended family play important roles in the metabolism and some of them are also of significant interest for industrial and medical purposes. As described in detail in Chapter 4, the mechanism of reaction catalyzed by flavocytochrome b2 is still a debated issue and computational approaches have been shown to be a powerful tool for the understanding of the mechanistic features.

Recently, genomics, trascriptomics and proteomics approaches led to the identification of new flavoproteins playing a key role in the metabolism of many organisms. Many of these new enzymes are involved in fundamental processes, such as cellular differentiation, apoptosis, protein folding and pathologies. Two of these novel medically-relevant flavoenzymes will be discussed in Chapter

2 and Chapter 3, respectively, namely Seladin-1/DHCR24, the putative flavoprotein member of the VAO family proposed to play a key role in the cholesterol biosynthesis pathway, and the human MICAL, a multidomain flavoprotein monooxygenase involved in axon guidance.

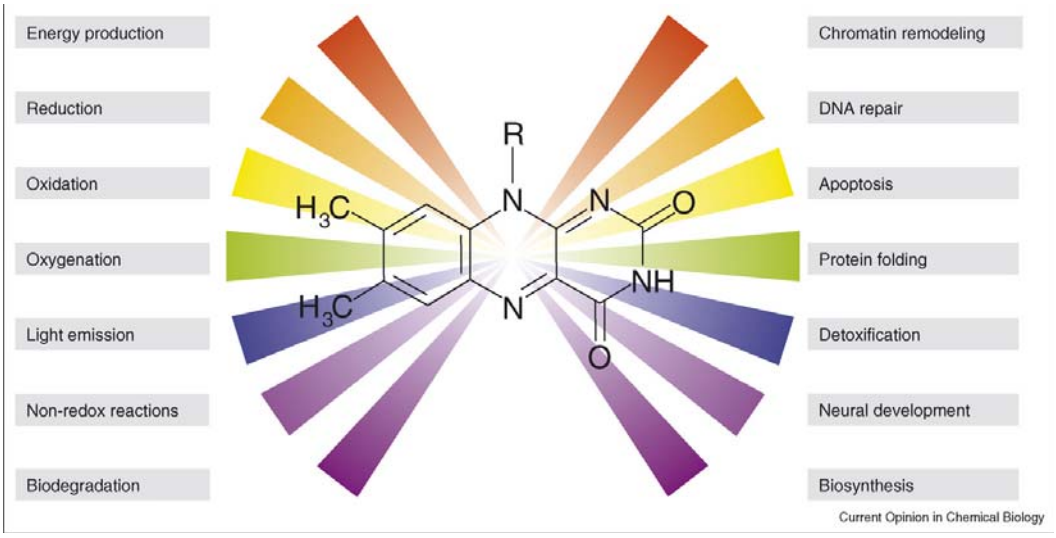

Figure 1.1: Biological functions of flavoenzymes (Joosten and van Berkel, 2007)

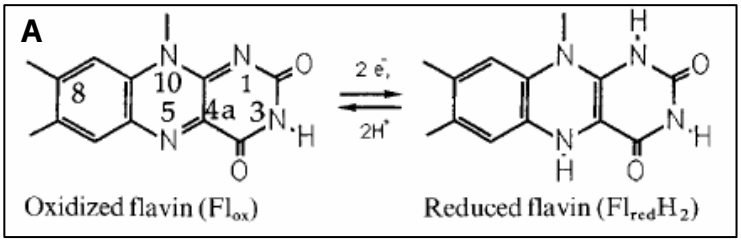

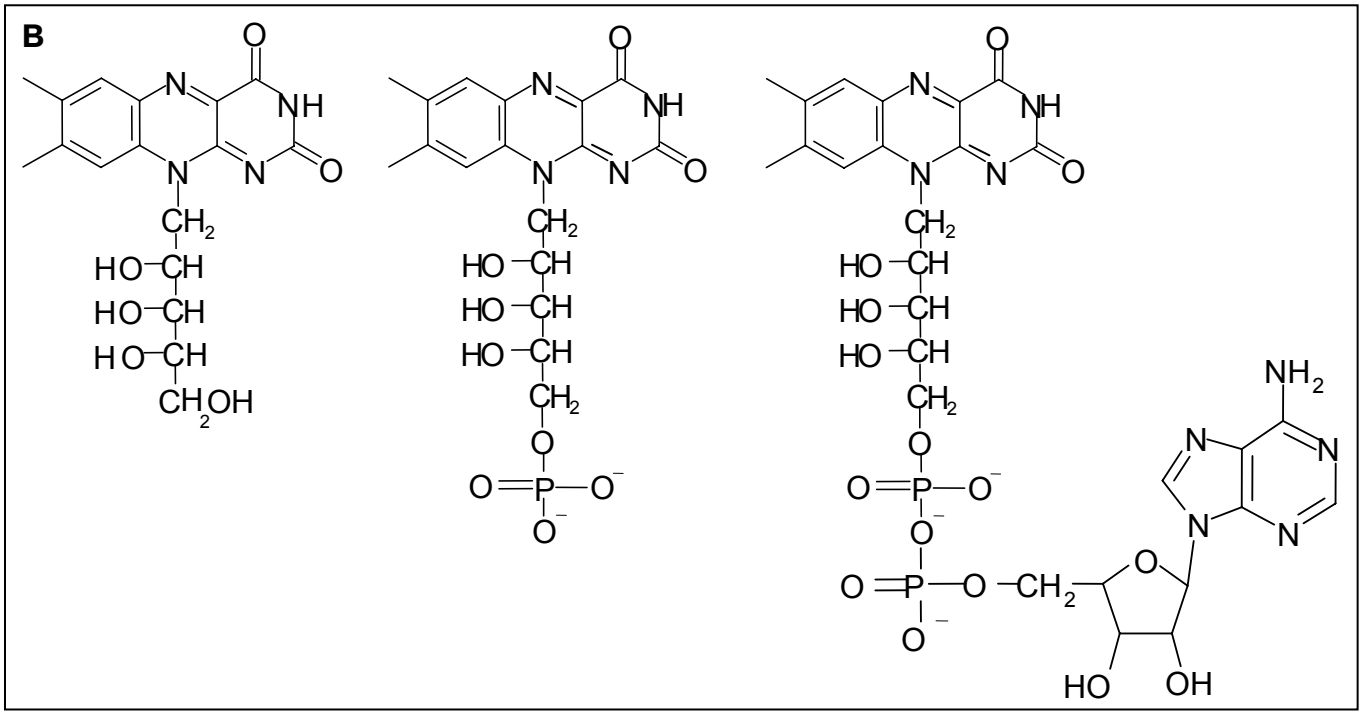

Figure 1.2: Panel A: Isoalloxazine nucleus in the oxidized and reduced forms (Ghisla and Massey, 1989). Panel B: structure of riboflavin (left), FMN (centre) and FAD (right) cofactors.

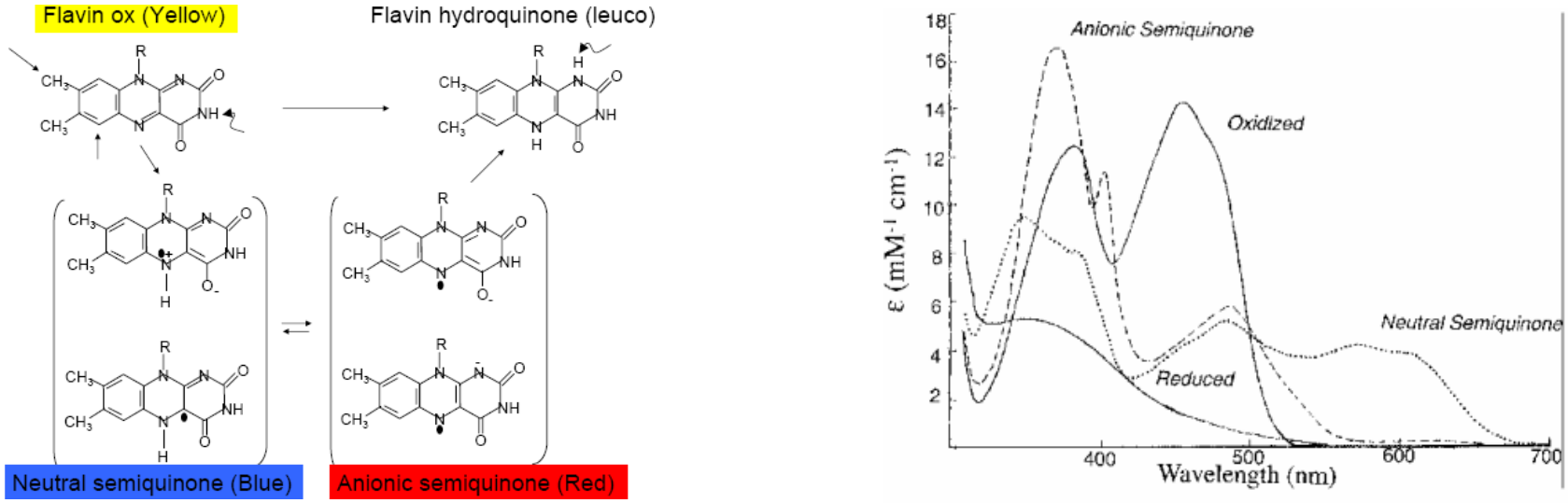

Figure 1.3: Structures (Panel A) and Spectra (Panel B) of the isoalloxazine group in the oxidized, semiquinones and hydroquinone forms (Massey, 2000).

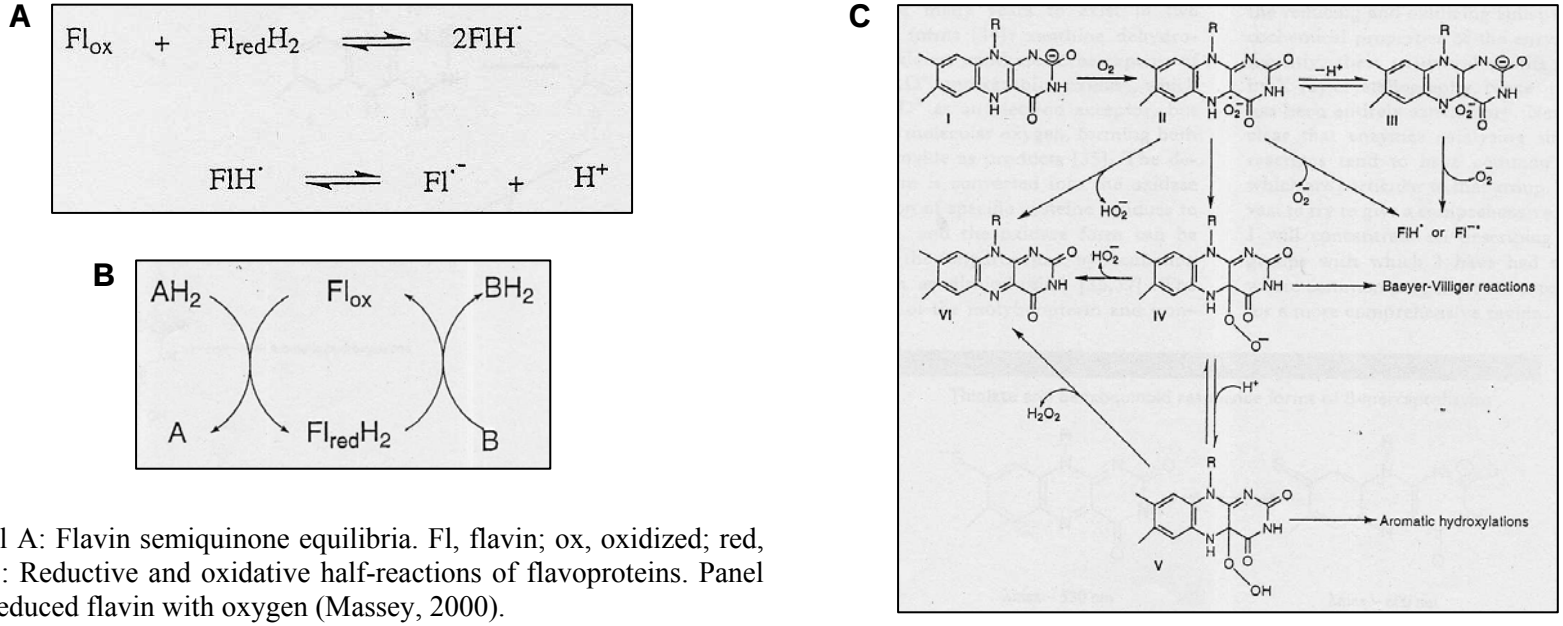

Figure 1.4: Panel A: Flavin semiquinone equilibria. Fl, flavin; ox, oxidized; red, reduced. Panel B: Reductive and oxidative half-reactions of flavoproteins. Panel C: Reactions of reduced flavin with oxygen (Massey, 2000).

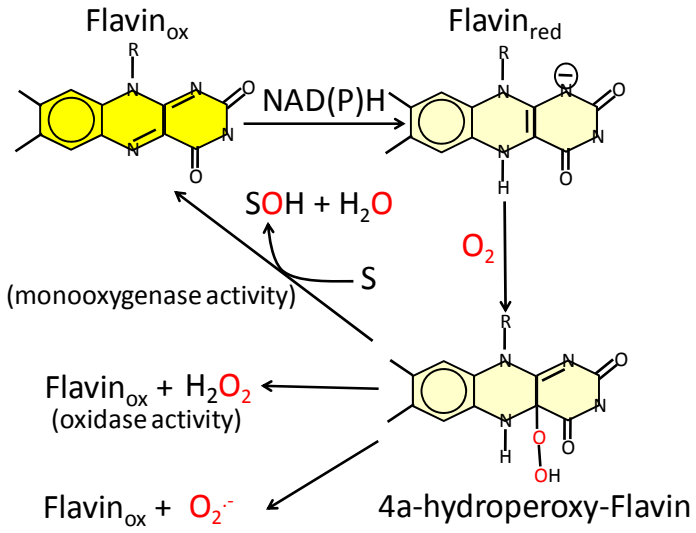

Figure 1.5: FAD-dependent monoxygenases reactions.

Table 1.1: Classification of external flavoprotein monoxygenases (van Berkel et al, 2006)

Sub-class	Prototype	Reactions[a]	Subunits	Cofactor	Coenzyme
A	4-OH-benzoate hydroxylase	Hydroxylation epoxidation	α	FAD	NAD(P)H
B	Cyclohexanone monooxygenase	Baeyer–Villiger; N-oxidation	α	FAD	NADPH
C	Luciferase	*Light emission*; S-oxidation; Baeyer–Villiger	α+β	–	FMN NAD(P)H
D	4-OH-phenylacetate hydroxylase	Hydroxylation	α+β	–	FAD NAD(P)H
E	Styrene monooxygenase	Epoxidation	α+β	–	FAD NAD(P)H
F	Tryptophan 7-halogenase	Halogenation	α+β	–	FAD NAD(P)H

[a] The most commonly found in vivo oxidation activities are given

Table 1.2: Classification of flavoproteins

Class	**Reaction**
Oxidase	$S_{red} + O_2 \leftrightarrow S_{ox} + H_2O_2$
Monooxygenase	$S + NAD(P)H + O_2 \leftrightarrow SOH + NAD(P)^+ + H_20$
Electron-transferase	$S_{red} + Aox \leftrightarrow S_{ox} + A_{rid}$
Dehydrogenase	$S_{rid} + NADP^+ \leftrightarrow S_{ox} + NADPH$

2. SELADIN-1, THE PUTATIVE 3-β-HYDROXYSTEROL-Δ^{24} REDUCTASE

2.1 INTRODUCTION

Alzheimer's disease (AD) is characterized by a substantial loss of neurons and synapses in selective brain regions, by the generation of intracellular neurofibrillary tangles and extracellular deposits of Aβ-amyloids (Figure 2.1.1). Severe degeneration of neurons occurs predominantly in selectively vulnerable neuronal population, such as the large pyramidal neurons of the inferior temporal cortex, the hippocampus, the amygdale and the entorhinal cortex. The pathology is associated to a decreased level of acetylcholine in neurons, a fundamental neurotransmitter. Furthermore, Aβ-amyloid aggregates led to an inflammatory response, with the accumulation of cytokynine, interleukins and TNF by macrophages, and consequent cell damage. Studies aimed to understand the pathological conditions underlying this selective vulnerability led to the identification of a novel gene, Seladin-1, from Selective Alzheimer Disease Indicator Protein-1, that was shown to be underexpressed in neurons undergoing Alzheimer degeneration (Greeve et al, 2000). Furthermore, studies on the expression level of this protein were extended to other tissues, revealing that Seladin-1 is also expressed in liver, spleen, ovary and adrenal gland (Greeve et al, 2000). Seladin-1 is mainly localized in the endoplasmic reticulum, and to a lesser extent in the Golgi complex. (Figure 2.1.2). The overexpression of Seladin-1 in neuroglioma cells protected cells from apoptosis induced by oxidative stress and increased resistance against Aβ-induced toxicity. The anti-apoptotic activity of Seladin-1 may be related to its inhibitory effect on caspase-3 activity (Greeve et al, 2000).

Seladin-1 expression was also found to vary in certain cancer cell lines, for example in adrenocortical adenomas and carcinomas, where the protein levels decreased during the tumor progression (Luciani et al, 2004). On the contrary, Seladin-1 gene expression is upregulated in melanoma metastases (Di Stasi et al, 2005) and in pituitary adenomas (Luciani et al, 2005), protecting cells from apoptosis induced by oxidative stress. Seladin-1 expression levels were shown to increase in neuronal cells treated with estrogens, explaining, at least in part, the beneficial effects of estrogens in preventing neurodegenerative diseases (Benvenuti et al, 2004). Furthermore, it was demonstrated that Seladin-1 expression is significantly reduced during human mesenchymal stem cells differentiation into neurons, suggesting that the defective Seladin-1 expression detected in AD vulnerable brain regions may be linked to an impaired neuronal stem cell compartment that could be a potential risk factor to develop the disease (Benvenuti et al, 2006). Thus, it has been proposed that reinforced Seladin-1 expression might be an additional point to be raised in favor of a stem cell-based therapy in AD.

Seladin-1 was shown to be identical to the putative human 3-β-hydroxysterol Δ^{24} reductase (DHCR24) (Waterham et al, 2001). Mutations on this gene are associated to desmosterolosis, an autosomic recessive disease that causes multiple congenital anomalies and mental development delays. Patients affected by this pathology showed altered plasma levels of desmosterol, the precursor of cholesterol in the cholesterol synthesis pathway (Figure 2.1.3). Cholesterol is an important structural component of cellular membranes and myelin, and the precursor of oxysterols, steroid hormones and bile acids. The identification of a number of inherited disorders due to a defect in cholesterol biosynthesis has made clear that cholesterol plays an important role in human embryogenesis and development (Waterham, 2006; Figure 2.1.3). Seladin-1 was proposed to be the enzyme that catalyzes the conversion of desmosterol into cholesterol, by reducing the Δ^{24} double bond of the substrate. All studies available indicate that the enzyme is rather promiscuous being able to reduce the same unsaturated function in cholesterol precursors other than desmosterol, leading to the conclusion that the increased level of desmosterol and the low cholesterol levels observed in patients may result from the funnelling of lanosterol towards desmosterol, which cannot be converted into cholesterol (Figure 2.1.3).

By searching for the putative human DHCR24 gene, Waterham et al (2001) located it to chromosome 1 (position 1p31.1-p33). The cDNA was found to encode a protein of 516 residues (Figure 2.1.4 panel A), corresponding to a mass of 60.1 kDa. Analyses of the primary structure of DHCR24 revealed that the N-terminal region of Seladin-1 presents a putative signal sequence (residues 1-21) for the localization of the protein in the endoplasmic reticulum (ER). Two putative transmembrane helices should anchor the protein to the ER membrane (residues 23-65), as reported by Greeve et al (2000). They are followed by a putative soluble domain. It has been proposed that the catalytic activity of the enzyme is associated to this domain, and that the enzyme contains a bound FAD cofactor on the basis of the finding of a (actually rather weak) similarity with the FAD-binding region of a class of flavoenzymes, which comprise oxidases, monooxygenases and reductases (Mushegian et al, 1995; Fraaije et al, 1998; Mattevi et al, 1998). Among similar proteins, Seladin-1 shows a marked sequence similarity to *Arabidopsis thaliana* DWARF1/DIMINUTO protein. This protein, also believed to be associated to the endoplasmic reticulum, has been proposed to participate in the synthesis of plant sterols and of brassinosteroids (Figure 2.1.5 panel B). Indeed, in DWARF1/DIMINUTO mutants altered levels of campesterol, the brassinolide precursor, were found and they led to severe growth defects (Klahre et al, 1998; Choe et al,1999). The similarity of Seladin-1 with DWARF1 supports the hypothesis that Seladin-1 is implicated in sterol methabolism (Figure 2.1.5; Waterham et al, 2001; Greeve et al, 2000). Another important evidence in line with the proposed catalytic activity of Seladin-1, is that expression of DHCR24 in

Saccaromyces cerevisiae cells led to measuring conversion of desmosterol into cholesterol in the presence of NADPH in whole cell extracts (Waterham et al, 2001). Interestingly, the activity doubled when the assays included FAD, a fact that was interpreted in support of the hypothesis that DHCR24 is a flavoenzyme.

Very recently, a model of DHCR24 in complex with FAD, desmosterol or cholesterol was built using the 3D structure of cytokinine dehydrogenase (Pedretti et al, 2008), a flavoprotein with structural similarities with the enzymes of the vanillyl alcohol oxidase (VAO) family (for a recent review see Leferink et al, 2008) (Figure 2.1.4 panel B). However, this model may not fully reflect the actual properties of DHCR24. During molecular dynamics simulation of the reduced enzyme in complex with desmosterol, FAD and desmosterol are tightly bound and close to each other. However, the sterol Δ^{24} double bond is too far from the flavin to be reduced by the postulated hydride transfer from the flavin N(5) to the C24 or C25 position. Simulations of the oxidized enzyme/cholesterol couple also led to puzzling results: FAD and cholesterol are very loosely bound to the enzyme model, leading (Pedretti et al, 2008) to imply that oxidized FAD will exit the active site at the end of the catalytic cycle acting as substrate rather than a co-enzyme. Finally, no obvious NADPH binding site was observed. The possibility that DHCR24 may not bind NADPH should not be disregarded, in fact the enzyme flavin may be reduced by a protein partner (e.g: a reduced cytochrome or ferredoxin).

Whether under some conditions DHCR24 may produce reactive oxygen species (ROS) is not known, but it has been proposed as a possibility on the basis of: (i) the known reactivity of reduced flavins with molecular oxygen as either part of their physiological activity (oxidases) or in the absence of the physiological substrate (monooxygenase) or following proteolytic or (oxidative) damage (Massey, 1995; Palfey and Massey, 1998; Massey, 2000) and (ii) the known roles of ROS in the cells. It has been proposed that DHCR24 may actually scavenge H_2O_2 (Lu et al, 2008).

The possible link between defects of sterol metabolism and the observed effect on cells, which include the severe developmental disorders observed in desmosterolosis, AD and cancer, is still not understood and is an open and controversial issue. There is accumulating evidence indicating a potentially important link between cholesterol, Aβ and AD. High levels of cholesterol in membranes was initially proposed to be a risk factor for AD. Thus, inhibiting cholesterol production in the brain might inhibit Aβ production, as supported by the fact that therapy with statins that reduce cholesterol synthesis appears to protect from AD (Wolozin, 2001; Fassbender et al, 2001). This theory is questioned by the proposed neuroprotective and antiapoptotic function of Seladin-1, which may protect cells from oxidative stress and from Aβ amyloid toxicity by degradation of H_2O_2 produced during inflammatory response to Aβ amyloid accumulation. Alternatively, the

antiapoptotic effect of DHCR24 may be linked to its enzymatic activity as a 24-dehydrocholesterol reductase, with the consequent increase of cholesterol in membranes, whose levels are very tightly controlled. Cholesterol plays multiple roles in cell metabolism being: (i) a component of cell membranes and, especially, (ii) lipid rafts, (iii) a hormone, (iv) an intracellular signalling molecule and (v) an essential player in the correct activation and function of hedgehog proteins, the secreted signalling proteins implicated in different embryonic patterning processes (Waterham, 2006). It as been proposed that the amount of cell cholesterol may affect amyloidogenesis, and, in particular, that the link between cholesterol and β-amyloid production is related to the membrane localization of the enzymes involved in the processing of the APP.

Seladin-1/DHCR24 has been found to be expressed in several tissues, and its levels vary in different situations with patterns that are sometimes difficult to interpret because the link between the DHCR24 enzymatic activity and its function as an antiapoptotic factor is unclear. The relation between the location and the function of Seladin-1 is also unclear. In the cells it is found associated with ER, the Golgi apparatus, but also with the nucleus (Battista et al, 2007; Battista et al, 2009). However it has not been established if the observed localization determines the function, if the localization is accompanied (due to) interaction with other proteins, posttranslational modifications or to production of different protein forms through alternative splicing events. All information on DHCR24 properties are indirect deriving from cell biology experiments, activity measurements in whole cell extracts or microsomes and from sequence analyses and (in silico) structural models. The fact that DHCR24 or its plant homolog have not been isolated yet in a homogeneous form results in no information being actually available on the actual structural and kinetic properties of the enzyme.

In order to gain information about the role of DHCR24 in the cell, the reaction(s) catalyzed and the nature of the protein, which are essential to complement cell biology studies, attempts to produce and characterize soluble forms of Seladin-1/DHCR24 were initiated with the production in *E. coli* of truncated forms of the enzyme in which N-terminal fragments were removed in order to produce the soluble catalytically active domain (Figure 2.1.4 panel A).

2.2 METHODS

Construction of plasmids for the production of DHCR24Δ26, - Δ33, -Δ41 and –Δ50 variants

Construction of pUC18DHCR24Δ26 vector: Amplification of the DHCR24Δ26 encoding fragment was done with the oligonucleotides "*Eco*RI-*Nhe*I Δ26" and "*Xho*I-*Hind*III reverse"

*Eco*RI-*Nhe*I Δ26 5'–GAAGGGGCTG*GAATTC*GTGGCTAGCCACCAGCGCTGGGTG–3'

*Xho*I-*Hind*III reverse 5'–GTACAAGAAAGC**TTA**TCA*CTCGAG*CCTGGCGGCCTTGCAG–3'

*Eco*RI-*Nhe*I Δ26 introduces an *Eco*RI (italic) and a *Nhe*I (underlined) restriction site. *Xho*I-*Hind*III reverse introduces *Xho*I *(italic)* and *Hind*III (underlined) sites and a stop codon (bold). The amplification was carried out with 0.4 μM oligonucletides, Platinum Taq High Fidelity DNA polymerase (Invitrogen, 1 U), dNTPs (0.2 mM each), pDEST15DHCR24, the polymerase buffer and 2 mM $MgSO_4$ in a final volume of 50 μl. PCR conditions were as follows: initial denaturation, 2 min at 94°C; cycle 1-30, 30 s at 94°C, 30 s at 55°C and 2 min at 68°C; final extension, 15 min at 72°C. The amplified fragment was digested with *Eco*RI and *Hind*III, purified by agarose gel electrophoresis followed by extraction and purification with the Wizard SV Gel and Clean-up system kit (Promega). The fragment was cloned into pUC18 plasmid digested and purified in the same way.

Construction of pCRII-TOPODHCR24Δ33, -Δ41 and –Δ50 vectors: Amplification of DHCR24Δ33, -Δ41 and –Δ50 encoding fragments from pDEST15DHCR24 was carried out using conditions described for the DHCR24Δ26 fragment and the following forward oligonucleotides

*Eco*RI-*Nhe*I Δ33 5'- CGTGCTCATCCAC*GAATTC*TGGGCTAGCGTGTGCCTCTTCC-3'

*Eco*RI-*Nhe*I Δ41 5'- GTTCGTGTGC*GAATTC*CTCCTGCCGGCTAGCCTTATCTTCG-3'

*Eco*RI-*Nhe*I Δ50 5'- GCTCTCGCTT*GAATTC*GATATGGCTAGCTACTACTACGTGCG-3'

The "*Xho*I-*Hind*III reverse" primer was used in combination with each one of the forward oligonucleotides. The amplification reaction was directly used to set up TOPO cloning reactions using the "TOPO-TA Cloning kit" (Invitrogen) as follows: 2 μl of fresh PCR product; 1 μl of salt solution; 1 μl of pCRII-TOPO vector in a final volume of 6 μl. Mixture was incubated 5 min at

room temperature and used to transform *E. coli* Mach T1 cells included in the TOPO-TA cloning kit. Transformants were selected on LB plates supplemented with 50 μg/ml kanamicin (Kan). The resulting plasmids *pTOPODHCR24Δ33, -Δ41 and –Δ50* from one of the resulting clones were sequenced (by Primm s.r.l., Milano, Italy) and used for the subcloning of the region encoding the truncated forms of DHCR24 into expression vectors.

Construction of plasmids for the expression of DHCR24 truncated forms: The DHCR24Δ26, -Δ33, -Δ41 and -Δ50 encoding fragments were excised from pUC18DHCR24Δ26 and pCRII-TOPODHCR24Δ33, -Δ41 and –Δ50 as *Nhe*I-*Xho*I, *Nhe*I-*Hind*III, *Eco*RI-*Hind*III and *Eco*RI-*Xho*I fragments and purified by agarose gel electrophoresis and Wizard SV Gel and Clean-up system kit (Promega). The fragments were inserted into pET23b and pETSUMO, pET28b, pMAL-c and pGEX-4T-1, respectively. Ligation was carried out with T4 ligase (Fermentas) at 16°C for 16 hours, using vector:insert ratios value of 1:3 and1:6. The ligation mixture was directly used to transform *E. coli* DH5α competent cells by the heat shock method. Transformants were selected on LB plates supplemented with 100 μg/ml ampicillin (Amp, for pUC18, pET23b, pETSUMO, pMAL and pGEX-4T-1 derivatives) and with 50 μg/ml kanamicin (for pET28b derivatives). DNA plasmid from one of the resulting clones was purified with QIAGEN® Plasmid Midi Kit (Qiagen), analyzed by restriction digestions and sequenced.

All manipulations were done using standard protocols (*Molecular cloning, a laboratory manual,* 1982; Sambrook et al, 2001; Current Protocols in Molecular Biology, 2005).

Expression of Seladin-1/DHCR24 variants

E. coli Rosetta (DE3) competent cells were transformed with the heat-shock method with ~ 100 ng of the plasmid of interest and selected on LB plates containing 25 μg/ml cloramphenicol (Clm) and 100 μg/ml Amp or 50 μg/ml Kan. Expression was carried out in Falcon tubes or in flasks. LB (50 or 100 ml) containing antibiotics was inoculated with ~20 colonies of transformants and the culture was grown at 25°C. The OD_{600} value was measured using a Uvikon810 (Kontron) spectrophotometer. When the OD_{600} reached a value of approximately 1, 100 μg/ml Amp was added (if the plasmid conferred Amp resistance) and the culture was transferred at 4°C overnight. The following day, the culture was transferred in a sterile 50 ml Falcon tube and the cells were harvested at 3500xg for 10 min, at 4°C in a swing-out centrifuge (Labofuge 400, Haereus). The supernatant was discarded and the cellular pellet was resuspended in LB (10 or 20 ml). Aliquots of the cellular suspension were used to inoculate 10 ml (in Falcon tubes) or 500 ml (in flasks) of selective LB, in order to obtain an initial OD_{600} value of 0.05. Cultures were grown at 25°C at 220 rpm, and Amp was added, if necessary, when the OD_{600} reached a value of 0.5. Induction of the expression of the

target protein was achieved by adding 0.1 mM IPTG (from a 100 mM sterile stock solution, in water). Cultures were maintained at 25°C or transferred at 15°C, after addition of Amp, if requested. Growth was monitored by OD_{600} measurement. Cells were harvested after 16 or 40 hours after IPTG addition at 5000 rpm for 10 min at 4°C in Sorvall centrifuges (Sorvall RC5C, GS3 rotor; Sorvall RC6 plus, SLA300 rotor). The cell pellet was then resuspended in cold 0.9% NaCl solution and centrifuged at 6000 rpm for 15 min. The supernatant was discarded and pellet was stored at -20°C.

Culture aliquots used for the OD_{600} measurement were also used to prepare total cell extracts for SDS-PAGE analysis. Cells were harvested in a microfuge at 13000 rpm for 1-2 min and the pellet was resuspended in a volume of SB1X determined as OD_{600} * 100 * ml of culture. Denaturation was carried out at 100°C for 10 minutes.

Cells (0.5 g) were used for the analysis of the soluble fraction by homogenization with glass beads. Cells are transferred in a glass tube (Ø=1 cm) and resuspendend in 1 ml of cold buffer (50 mM sodium phosphate, pH 8.0, 0.1 M NaCl). 3 g of glass beads (Ø=0.25-0.3 mm) were mixed to the suspension. Homogenization was carried out by applying 5 cycles of 1 minute on vortex and 1 min on ice. 2 ml of cold buffer were added and the homogenate was transferred in a 10 ml centrifuge tube. Glass beads were washed with an additional 1 ml of buffer and the sample was centrifuged at 18000 rpm for 1 hour at 4°C (SS34 rotor). 75 µl of crude extract were denatured for SDS-PAGE by adding 25 µl of SB4X (0.25 M Trs/HCl, pH 6.8, 8% SDS, 40% glycerol, 0.004% Bromophenol Blue, 29% β-Mercaptoethanol). The SDS-PAGE sample for the insoluble fraction was prepared by resuspending 20 mg of the pellet obtained after centrifugation of the homogenate with 400 µl of SB1X. Denaturation was done at 100°C for 10 minutes.

Analytical purification of DHCR24 truncated forms with N- or C- terminal His-tag.

Affinity chromatography on Ni-NTA Sepharose: DHCR24Δn variants of Seladin-1/DHCR24 with a N- or C-terminal His-tag were purified by affinity chromatography on Ni-NTA Sepharose. Buffers used for purification were: buffer A) 50 mM sodium phosphate pH 8.0, 0.1 M NaCl; buffer B) 50 mM sodium phosphate pH 8.0, 0.1 M NaCl, 10 mM imidazole; buffer C) 50 mM sodium phosphate pH 8.0, 0.1 M NaCl, 100 mM imidazole; buffer D) 50 mM sodium phosphate pH 8.0, 0.1 M NaCl, 500 mM imidazole. For analytical purification, *E. coli* Rosetta (DE3) cells (4 g) that had produced DHCR24 truncated variants were homogenized by sonication (six 30 s cycles with a Branson Sonifier with temperature controlled by immersion in a ice-salt bath). The crude extract was loaded on 2 ml of Ni-NTA Sepharose column, that had been equilibrated with 5 volumes of buffer A.

Elution was carried out by gravity with discontinuous gradient of imidazole (10-100-500 mM, 5 volumes each).

Extraction of membrane-bound His-Δ41 or solubilization of aggregates was attempted in the presence of detergents at concentrations (from 10% stocks prepared in buffer A) reported below.

Detergent	**(%)**	
	CMC[a]	**Concentration**
TRITON-100X	0.02	0.2
CHAPS	0.6	0.6, 2
Octylglucoside	0.7	0.7, 2
Deoxycholate	0.2	0.2

[a] CMC, critical micellar concentration

Aliquots of cells (1 g) were homogenized using the glass beads method in buffer A containing the indicated detergents; alternatively 5 g of cells were sonicated in buffer A and the detergents were added to aliquots of the homogenate. In both cases, samples were incubated in the presence of detergents for 1 hour at 4°C at 10 rpm on a wheel in order to enhance the extraction of proteins bound to *E. coli* membranes or dissolve aggregates. Samples were then centrifuged at 15000 rpm for 1 h and crude extracts were incubated with 1 ml Ni-NTA Sepharose resin equilibrated in buffer A for 1 h on a wheel. A 3 min centrifugation at 900 g in a swing-out rotor (Labofuge 400, Heraeus) was carried out to pellet the resin after each incubation. The supernatant (unbound material) was discarded and additional unbound material was removed in batch by washing the resin with buffer A containing detergents (2 ml each, 10 min). The resin was then washed twice with 2 ml buffer B containing the detergent. It was resuspended in 2 ml of the buffer and packed in a small column. Elution of bound proteins was obtained by applying buffer A containing detergent and 250 mM imidazole (6 column volumes) and 2 ml fractions were collected.

Anionic exchange chromatography: The crude extract from 1 g of *E. coli* cells that had produced His-DHCR24Δ41 was loaded on 1 ml Q-Sepharose column, equilibrated in 20 mM sodium phosphate buffer, pH 8.0 (buffer E). The column was developed by gravity flow with a discontinuous NaCl gradient (100 mM, 500 mM and 1 M; 5, 7 and 4 column volumes, respectively) and 1 ml fractions were collected.

Cationic exchange chromatography: The crude extract from *E. coli* cells (1 g) that had produced His-DHCR24Δ41 was loaded on 2 ml SP-Sepharose resin equilibrated with buffer E, pH 7.0. A discontinuous NaCl gradient was applied (0.1, 0.2, 0.3, 0.4 and 0.5 M NaCl, 2 volumes each) to elute bound proteins. Column was developed by gravity flow and 2 ml fractions were collected.

Preparative purification of His-tagged DHCR24Δn mutants.

For the preparative purification, the crude extract from 40 g of cells that had produced DHCR24Δ50-His was loaded on 20 ml of Ni-NTA Sepharose resin (in a XK16 column, GE Healthcare) equilibrated in buffer 50 mM sodium phosphate pH 8.0, 0.1 M NaCl (buffer A), connected to a FPLC Akta system. Elution of weakly bound proteins was obtained with buffer B (100 ml). A gradient from 10 mM to 500 mM imidazole (in 200 ml) was applied to elute bound proteins.

Gel filtration was carried on using a Superose-12 HR 10/30 column (GE Healthcare), equilibrated with buffer A, with a FPLC system. Gel filtration was carried out in the same buffer (0.5 ml/min) and 0.5 ml fractions were collected. The eluted sample was then chromatographated on anionic exchange Mono-Q HR 5/5 column, equilibrated with 20 mM sodium phosphate buffer, pH 8.0 (buffer E). Elution was obtained with salt gradient (0-500 mM NaCl, in 20 ml), applying a 0.5 ml/min flow and collecting 0.5 ml fractions.

After each purification step, the sample was concentrated by ultrafiltration in a Amicon concentrator equipped with a YM10 membrane, with 0.5-1 atm pressure.

According to methods reported by (Magnusdottir et al, 2009), osmotic shock on cells expressing the His-DHCR24Δ41 variant was performed in order to increase the amount of protein able to bind the Ni-NTA functional groups. It is reported that the presence of periplasmic low molecular weight compounds could interfere with the bound of poorly expressed His-tagged proteins to the functional groups of the resin. Thus, periplsmic environment was removed by osmotic shock. Fresh harvested cells were resuspended with 50 mM Hepes buffer, pH 7.9, 20% sucrose, 1 mM EDTA with a ratio of 5 ml buffer/g cells. The sample was centrifuged for 30 min 7000g and pellet resuspended in 5 ml/g of cell of 5 mM $Mg(SO)_4$, taking care to maintain cells on ice. Cells were incubated for 10 min on ice, harvested by centrifuging for 20 min at 4500g at 4°C and finally resuspended in 1.5 ml/g of cells of lysis buffer (100 mM Hepes buffer, pH 8.0, 500 mM NaCl, 10% glycerol, 10 mM imidazole, 0.5 mM β-Me, 1 mM PMSF, DNase). Resuspention can be stored at -20°C or directly homogenized for the further purification.

Analytical purification of DHCR24 truncated forms with N- terminal GST and MBP tags.

Affinity chromatography on Glutathionyl Sepharose resin: Glutathionyl Sepharose resin was equilibrated with 10mM sodium phosphate, 1.8mM potassium phosphate buffer, pH 7.2, 140 mM NaCl, 2.7 mM KCl (PBS buffer). Crude extracts in PBS buffer containing 1 mM EDTA, 1 mM PMSF, 1 mM DTT were loaded by gravity on a 1 ml column. Alternatively, 1 ml resin was incubated with the sample for 30 minutes at 4°C at 10 rpm. The resin was packed into a column. In

both cases the resin was washed with 5 volumes of PBS buffer containing 1 mM EDTA and 1 mM PMSF. Elution of bound proteins was carried out by gravity with PBS buffer containing 10 mM glutathione. 1 ml fractions were collected and analyzed spectrophotometrically and by SDS-PAGE.

Affinity chromatography on amylose resin: 1 ml of amylose resin was used for the purification on analytical scale of MBP-DHCR24Δn proteins. The resin was equilibrated with 20 mM Tris/HCl buffer, pH 7.4, 0.2 M NaCl, 1 mM EDTA (CB buffer), containing 5 mM β-Me, 1 mM PMSF. The column was washed with 5 volumes of CB buffer and elution was carried out by flowing CB buffer containing 10 mM maltose (5 volumes). 1 ml and 0.5 ml fractions were collected for the washing and elution steps, respectively. A 0.1% SDS solution was used to elute proteins precipitated on the resin.

2.3 RESULTS

Preliminary results on the expression of Seladin-1/DHCR24 and its Δ20, Δ60 and Δ90 variants

Preliminary expression experiments were carried out in a small scale in order to rapidly identify the conditions for the production of soluble Seladin-1/DHCR24 forms. pDEST15DHCR24, pBAD49DHCR24 and pDEST17-18DHCR24 Gateway plasmids encoding the full-length human Seladin-1/DHCR24 and forms carrying N-terminal tags (from RZPD, Germany) have been used for these trials and different *E. coli* strains, BL21 (DE3), C41, and Rosetta (DE3), were tested as the host. In all cases no protein was produced.

DHCR24 has been proposed to be a flavin-dependent enzyme, associated with the endoplasmic reticulum membrane through two predicted N-terminal transmembrane helices. Therefore, pDEST15DHCR24 plasmid was used to generate truncated forms of the enzyme with a C-terminal His-tag (cloning into pET23b) by removing N-terminal fragments (Δ20, Δ60 and Δ90) in order to produce the catalytic domain in a soluble form. The Δ20 enzyme could not be produced in *E. coli* cells, resulting very toxic even at low temperature (15°C). For the other two variants, Δ60 and Δ90, best results were obtained expressing proteins in *E. coli* Rosetta (DE3) at 15°C and a small fraction of soluble protein could be isolated thanks to the presence of His-tags, but had no cofactor bound.

On the basis of sequence analyses and inspection of a three-dimensional homology model of Seladin-1 based on plant cytokinin dehydrogenase (Pedretti et al, 2008), the production of a novel series of plasmids was planned for the production of soluble forms of the enzyme, in fusion with different tags (Fig 2.3.1).

Production and purification of DHCR24 His-tagged truncated forms

Expression of DHCR24Δ26 and Δ41 variants with N- and C-terminal His-tag.

Taking into account the results obtained for the expression of DHCR24Δ60 and Δ90 in *E. coli* strains, preliminary expression experiments were carried out firstly with the His-tagged Δ26 and Δ41 variants.

E. coli Rosetta (DE3) cells were transformed with the plasmids encoding His-DHCR24Δ26 (His-Δ26), DHCR24Δ26-His (Δ26-His), His-DHCR24Δ41 (His-Δ41) and DHCR24Δ41-His (Δ41-His). 50 ml cultures of transformants were grown in LB medium containing 25 μg/ml Clm and 100 μg/ml Amp or 50 μg /ml Kan (for the pET23b and pET28b derivatives, respectively) at 25 °C, 220 rpm. When the OD_{600} reached value of approximately 1, cultures were transferred at 4°C overnight. 20 ml of cultures were harvested at 3500xg for 10 min at 4°C and pellets were resuspended into 40 ml

of fresh LB. Two aliquots of 9 ml of LBClmAmp/Kan (in falcon) for each mutant were inoculated with 1 ml of cellular resuspension, and cultures were grown at 25°C, until OD_{600} reached value of approximately 1. Protein expression was induced adding 0.1 mM IPTG. A this point, for each mutant, one 10 ml culture was maintained at 25°C, and the other was transferred at 15°C. 16 hours after induction, cells were harvested and total, soluble and insoluble protein fractions were investigated. As shown in Figure 2.3.2, His-Δ26 and Δ26-His forms had a very low or even absent level of expression at both temperatures, thus, they were abandoned. On the contrary, His-Δ41 and Δ41-His variants showed good expression levels, higher than those observed previously for the Δ60-His and Δ90-His variants. An appreciable amount of soluble protein was present only in cells grown at 15°C, in spite of the fact that most of it was in inclusion bodies.

These first encouraging results led us to experiment the expression of the Δ41 His-tagged mutants in a larger scale, in order to obtain sufficient grams of cell for the further purification trials. *E. coli* Rosetta (DE3) cells expressing Δ41 truncated forms with His-tag at the C-terminal (pET23b derivatives) and N-terminal (pET28b derivatives) were grown as previously described, in 1-2 litres of culture, that were incubated at 15°C for 16 or 41 hours after induction with 0.1 mM IPTG. The total amount of expressed proteins was similar to that obtained in the previous experiment, with no significant increase after 41 hours induction. It was confirmed that most of the protein was produced as insoluble fraction and only a small part was soluble.

Analytical purification of DHCR24Δ41 variants: affinity chromatography on Ni-NTA-Sepharose

Analytical purification trials on NiNTA Sepharose were carried out firstly for Δ41 His tagged forms. *E. Coli* cells that had produced the His-Δ41 and Δ41-His (4 g) were resuspended in 2.5 ml/g cells of buffer A containing 1 mM β-mercaptoethanol and they were homogenized by sonication. The homogenate was then diluted with 2.5 ml/g cells with buffer A and centrifuged. The crude extract was directly loaded on a 2 ml column of Ni-NTA Sepharose pre-equilibrated with 5 volumes of buffer A. The resin was washed with 3 volumes of buffer A and elution of bound proteins was obtained with a discontinuous gradient of imidazole (buffers B, C, D; 3 column volumes each). Fractions (1 ml) were analyzed by SDS-PAGE and spectrophotometrically. A flavin signal was observed for the first time in fractions eluted with 100 mM imidazole, as confirmed by fluorescence analysis (Figure 2.3.3). As shown in figure 2.3.4 (panel A and C) the fractions contained several protein species, so that it was not possible to identify the band corresponding to His-Δ41 and Δ41-His. Thus, western-blot was necessary to verify the actual presence of His-Δ41 and Δ41-His which might be responsible for the flavin signal we observed. Western blot detection with antibodies directed against Seladin N- or C-terminal peptides (Figure 2.3.4 panel B and D) confirmed that His-Δ41 and Δ41-His were present in large amounts in the whole cell extracts and in the insoluble

fraction. Only a small fraction of soluble DHCR24 bound to the resin and eluted with 100 mM imidazole (Figure 2.3.4 panel B and D).

In order to increase the amount of protein able to bind the Ni-NTA resin, a pre-treatment of the cell by osmotic shock was attempted, as described in (Magnusdottir et al, 2009) using 17 g of cells grown at 15°C for 16 hours after IPTG induction. After the osmotic shock, the preparative purification of His-Δ41 was carried out. Cells were homogenized by sonicaton (45 cycles of 4 sec) and sample was centrifuged 15 min at 20000 rpm at 4°C. The crude extract (18 ml, 15 mg/ml) appeared cloudy, so it was filtered with 0.2 μm membrane. It was loaded by gravity on a 5 ml Ni-NTA Sepharose column equilibrated with the lysis buffer and 2 ml fractions were collected. The column was then connected to a Akta system (GE Healthcare) and developed with continuous 10-500 mM imidazole gradient (1 ml/min flow). Spectrophotometric analyses of fractions showed a flavin signal coeluting with His-Δ41, as confirmed by western blot, but, also in this case, the amount of unbound protein was the same as that observed before, indicating that the osmotic shock treatment did not increase the amount of bound protein. N-terminal sequencing of the His-Δ41 variant from the insoluble fraction (Figure 2.3.2 panel D) confirmed the presence of the His-tag at the N-terminus of the protein produced in *E. coli*. Thus, we could suggest that the low adsorption of the protein to Ni-NTA Sepharose may be a consequence of a modification at the N-terminus occurring during the purification procedure, or that the soluble fraction of the enzyme is actually characterized by large aggregates that prevent the His-tag recognition of the Ni-NTA Sepharose functional group.

The production of DHCR24Δ41 in *E. coli* cells showed a poor recovery of soluble protein from cell homogenates, so that one can suppose that the protein is accumulated in inclusion bodies and/or is associated with *E. coli* membranes. Attempts to increase the soluble fraction of the enzyme were done using different detergents during the purification. In a pilot experiment, 5 g of *E. coli* cells containing His-Δ41 were homogenized in buffer A. Aliquots of the homogenate were incubated for 1 h at 4°C in the presence of the following detergents (%, w/v): sodium deoxicholate (DOC; 0.2 and 2%); octylglucoside (OGL; 0.7 and 2%) and CHAPS (0.6 and 2%). A negative control with no detergent was also analyzed. During incubation at 4°C 2% DOC precipitated, so this sample was abandoned. The crude extracts obtained after centrifugation of the homogenate were incubated on a wheel with 1 ml of Ni-NTA Sepharose resin equilibrated with the same homogenization buffer for 1 hour. The resin was packed in a column. The elution of bound proteins was carried out with a discontinuous gradient of imidazole (10-250 mM) in buffer A in the presence of detergents at the same concentration. SDS-PAGE analysis revealed that detergents did not significantly alter the SDS-PAGE pattern of *E. coli* proteins and decreased the soluble level of His-Δ41 in the crude

extract. Very similar results were obtained when 2% CHAPS, 2% OGL and 0.2% Triton were added directly in the homogenization buffer. Also in this case, CHAPS and OGL affected the solubility of His-Δ41, while the level of soluble protein in the presence of Triton X100 was comparable to the control (Fig 2.3.5). Thus, we can suppose that the poor recovery of soluble protein from cell homogenates was not due to its association with the *E. coli* membranes and its levels could not be significantly increased using detergents.

Analytical purification of DHCR24Δ41 variants: ionic exchange chromatography

In order to circumvent the problem of the low binding to the metal affinity column, small scale purifications on anionic and cationic exchange resins were attempted with cells that had produced His-DHCR24Δ41. Homogenization of 1 g of cells was carried out using glass beads in buffer E. Crude extract obtained after centrifugation at 18000 rpm for 1 hour was directly loaded on a 2 ml Q-Sepharose column, equilibrated with buffer E. The column was developed with a discontinuous gradient of NaCl (0.1, 0.5 and 1M) in buffer E and 1 ml fractions were collected. Western blot analysis of fractions showed that also in this case the enzyme did not bind to the resin, eluting totally in the flow-through (Fig 2.3.6 panel A and B) of the column. Furthermore, no flavin signal was detected in any fraction.

Analytical purification on a cationic exchange resin was also attempted. Crude extract from 1 g of cells was loaded on a 2 ml SP-Sepharose column, equilibrated with buffer E, pH 7.0 and proteins were eluted with steps by increasing the concentration of NaCl (0-1M) stepwise. Also in this case the protein did not bind the resin, indicating that large aggregates are formed that cannot interact with the functional groups of the resins (Fig 2.3.6 panel C and D).

Although His-Δ41 and 41-His could not be successfully purified, the flavin signal observed for the first time, which coeluted with the enzymes, was very encouraging. Thus we tried to produce other protein mutants, in order to improve the solubility of the protein by identifying the boundary of the soluble (catalytic) domain.

Expression and analytical purification of Δ33 and Δ50 His-tagged variants

E. coli Rosetta (DE3) cells were transformed with pET23b and pET28b derivatives encoding the Δ33 and Δ50 enzyme forms. For protein expression cells were grown as described for the Δ41 variants. His-Δ33 and His-Δ50 showed expression levels similar to those observed for His-Δ41 and Δ41-His, with an considerable amount of soluble protein (Fig 2.3.7 panel A). On the contrary, plasmids encoding the protein forms with C-terminal His-tags were mildly toxic for *E. coli* cells (Figure 2.3.7 panel B). The amount of protein detected in total extracts was lower than that

observed for N-terminal His-tagged forms, but the soluble fraction was similar. In all cases 3-4 g of cells per litre of culture were obtained.

Purification of His-Δ33, Δ33-His, His-Δ50 and Δ50-His on Ni-NTA Sepharose resin was carried out from cells grown at 15°C as described for the Δ41 mutants, with essentially identical results. In particular, we confirmed that most of the protein did not bind to the resin, in spite of the fact that also His-Δ33 and His-Δ50 carry their N-terminus, as indicated by N-terminal sequencing. As observed for the Δ41 variant, also in this case the bound DHCR24 eluted with 100 mM imidazole (Figure 2.3.7 panel C and D), associated with a flavin signal.

Preparative purification of DHCR24Δ50-His variant.

In order to verify whether the flavin signal was actually associated with DHCR24 rather than to one of the contaminants that elute with 100 mM imidazole, we carried out a complete purification of the protein associated to the flavin, using cells that had overproduced DHCR24Δ50-His, one of the forms showing good solubility.

The crude extract from 20 g cells was chromatographed on a 20 ml Ni-NTA Sepharose column, which was developed with a 10 to 500 mM imidazole linear gradient (10 columns volumes, Figure 2.3.8 panel A). Spectrophotometric analysis revealed that fractions 96-104 contain a flavoprotein. SDS-PAGE showed that these fractions contained several protein species (Figure 2.3.8 panel B). Thus western-blot was necessary to confirm the presence of Δ50-His. As shown in fig 2.3.8 panel C, DHCR24Δ50 was actually present in these fractions. Therefore they were pooled and concentrated. After concentration, the sample still showed the flavin signal (Figure 2.3.8 panel D). The sample was gel filtered on a Superose12 column, pre-equilibrated with buffer A (Figure 2.3.9 panel A). A flavin signal coeluted with fractions 25-27, which contain three main protein species, one of which had the expected mass for Δ50-His (Figure 2.3.9 panel C). Thus, these fractions were pooled, concentrated (spectrum of the sample in Figure 2.3.9 panel B) and chromatographed on a Mono-Q column (in 20 mM sodium phosphate buffer, pH 8.0), which was eluted with a gradient of NaCl from 0 to 500 mM (Figure 2.3.10 panel A). Fractions collected during the initial wash and the 0-500 mM NaCl gradient were analyzed by absorbance spectroscopy and SDS-PAGE. These analyses showed that the flavin signal was associated with a protein of 55 kDa, i.e. the expected mass of Δ50-His (Figure 2.3.10 panel B and C). However, this protein was not recognized by the anti-Seladin-1 antibodies (Figure 2.3.11 panel A). Further analyses showed that Δ50-His eluted from the gel filtration column at a mass higher than 100 kDa as a colourless protein. (Figure 2.3.11 panel B and figure 2.3.9 panel A).

This result may suggest that or DHCR24 is not a flavoprotein, or, more likely, that the produced forms do not correspond to the domain of the holoenzyme. N-terminal sequencing confirmed that the 50 kDa flavin-associated protein is the *E. coli* alchil-hydroperoxide reductase (56 kDa).

Production of GST- and MBP-DHCR24Δn derivatives

Expression of GST-DHCR24 truncated forms in E. coli and purification on glutathionyl (GSH)-Sepharose

Plasmids encoding DHCR24Δ26, -Δ33, -Δ41 and -Δ50 forms in fusion with GST tag at N-terminus were used to transform *E. coli* Rosetta (DE3) competent cells. Cells containing pGEX-4T-1 vector were grown as negative control to monitor the toxicity effect due to the plasmid or to the heterologous proteins expression. 500 ml cultures were grown as described for the pET derivatives. As shown in figure 2.3.12, the expression of GST-Δ26 at 15°C for 42 hours after induction with 0.1 mM IPTG was not toxic. A higher protein level was observed in total cell extracts, compared to that observed with pET vectors, but the amount of soluble protein was not significantly increased. Expression of GST-Δ33, GST-Δ41 and GST-Δ50 for 17 hours after induction showed similar results.

Purification attempts on an analytical scale were carried out for all the GSTDHCR24 derivatives and for the negative control expressing GST. 2 or 4 g of cells were resuspended in 2.5 volumes of PBS buffer, containing 1 mM EDTA, 1 mM PMSF, 1 mM DTT and homogenized with glass beads or by sonication (6 cycles of 30 sec) in the presence of DNase. In all cases the crude extract was clear and appeared pale yellow after centrifugation at 18000 rpm for 1 h. The rude extracts obtained from 2 g of cells that had produced GST-Δ26 GSTΔ33 –Δ41 and -Δ50 were incubated with GSH-Sepharose resin for 30 min at 4°C. GST protein produced in positive control cells was also purified. After incubation with the crude extract, the resin was washed in batch with PBS buffer, containing 1 mM EDTA, 1 mM PMSF, 1 mM DTT (6 column volumes) and packed into a column. The elution of bound proteins was done by flowing PBS buffer containing 10 mM glutathione (5 column volumes). SDS-PAGE analysis of fractions revealed that the DHCR24 proteins did not bind the resin (see, e.g. the case of GST- Δ33 in Figure 2.3.12 panel B), while GST was successfully purified (Figure 2.3.12 panel C).

Production and analytical purification on amylose resin of MBP-DHCR24Δn enzymes

The expression of MBP-DHCR24Δ26, -Δ33, Δ41 and Δ50 forms in *E. coli* was carried out as previously described. *E. coli* expressing MBP alone was used as positive control. SDS-PAGE of total cell extracts showed a similar degree of expression 41 hours after induction (Figure 2.3.13

panel B), except for the Δ26 form, whose level was lower then that of the other constructs (Figure 2.3.13 panel A). Proteins were extracted by sonication in CB buffer containing 5 mM β-Me, 1 mM PMSF. The crude extracts were characterized by a significantly higher amount of soluble MBP-DHCR24 protein, as compared to the corresponding His-tagged forms, in particular for the Δ41 (Figure 2.3.13 panel B and C) and Δ50 forms. This result indicates that MBP increased the solubility of the heterologous proteins. The MBP-DHCR24 forms were purified to near homogeneity by affinity chromatography on a 1 ml of amylose column, equilibrated with CB buffer. The fractions eluted with CB buffer containing 10 mM maltose were characterized by the presence of a species with the expected mass of ~ 98 kDa (Figure 2.3.13 panel C). Western-blot with anti Seladin C-terminal antibodies confirmed the proteins to be MBP-DHCR24 variants (Figure 2.3.13 panel D). No flavin signal was associated to these fractions. Dynamic light scattering (DLS) measurements on fractions containing MBPDHCR24Δn variants were performed (20-30 acquisitions, at 15°C). As shown in figure 2.3.13 panel E, a radius of 47 nm was obtained, which corresponds to a molecular mass of 20 MDa. This indicates that the MBPDHCR24Δn proteins all form high molecular mass aggregates.

Denaturation of fractions containing MBPΔ26 by a 5 hours dialysis in the presence of 6 M Urea followed by refolding in buffer containing 0.1 mM FAD led to the obtainment of very low amount of soluble protein that did not contain FAD.

Fluorescence analyses on fractions containing MBPΔ33, -Δ41 and Δ50 did not show any flavin signal (see, e.g. the MBPΔ33 case in Figure 2.3.14), suggesting that these variants do not contain any cofactor or that the flavin signal is quenched. Thus, heat denaturation of fractions containing these proteins was carried out by incubation at 100°C for 15 min in the dark in order to release the cofactor, if present. As shown in Figure 2.3.14, denaturation of the MBPDHCR24Δ33 led small amounts of flavin released and similar results were obtained with the other constructs. To identify the nature of the flavin, samples were reacted with phosphodiesterase (PDE) that converts FAD in FMN (Aliverti et al, 1999). Emission spectrum of FMN at 530 nm is 10 folds higher than that of FAD. A Cary Eclipse (Varian) fluorimeter was used, measuring emission spectra between 500 and 600 nm and exciting samples at 450 nm. The emission spectrum of 2 ml of CB buffer, 10 mM maltose, 20 mM $MgCl_2$ was recorded in a 3 ml cuvette. 100 µl of the denatured fractions were added and fluorescence emission spectrum registered. The observed flavin signal was greater than 80% FAD, but it accounted for less than 1% of the expected amount estimated from the quantity of DHCR24 present in the sample if DHCR24 is a properly folded protein.

Production of His-SUMODHCR24Δn mutants

Construction of plasmids for the expression of His-SUMODHCR24 truncated forms.

Attempts to purify the His-DHCR24 truncated forms by chromatography on Ni-NTA Sepharose resulted in a low binding to the metal affinity column, with the most of the protein eluting in the flow-through of the column. This result may suggest that proteins are expressed as aggregates that may interfere with the recognition of the His-tag with the functional groups of the resin. The adopted strategy was then to interpose a linker between the His-tag and the DHCR24 protein that could enhance the correct folding and the subsequent binding of the His-tag to the resin.

Using the same cloning strategy adopted for the other constructs, fragments encoding for DHCR24Δ26, -Δ33, -Δ41 and -Δ50 proteins were excised from donor vectors with *Nhe*I/*Xho*I digestions and inserted into pETSUMO vector, previously mutagenized to delete the *Nhe*I restriction site present at the 5' of the SUMO gene. Expression of the target protein with His-SUMO protein fused at the N-terminus has been shown to be a powerful tool to increase solubility and folding levels of several proteins (Butt et al, 2005; Malakhov et al, 2004; Marblestone et al, 2006) and should facilitate their purification by mean of affinity chromatography. Furthermore, the presence of a specific SUMO-protease cleavage site just at the starting point of the target protein should allow the subsequent purification of the native protein, without any added residues.

The expression of His-SUMODHCR24Δn proteins was carried out as described for the pET derivatives. Cultures of E. *coli* Rosetta (DE3) cells expressing the pETSUMODHCR24 mutants (500 ml each) were grown at 25°C until the OD_{600} reached a value of 1. Then, they were transferred at 15°C after induction with 0.1 mM IPTG for 16 hours. Cells were harvested (4.5 g of cells per culture) and 0.5 g were used to analyze the expression levels and the solubility of the protein forms. As shown for the His-SUMOΔ26 (Figure 2.3.15 panel A), the fusion with the His-SUMO tag led to an increased amount of protein in cell total extracts, but, as observed for the His-tagged variants, most of the protein was present in the insoluble fraction. Identical results were obtained also for Δ26, Δ33 and Δ41.

The cells were used to carry out an analytical affinity chromatography on Ni-NTA Sepharose, as described in detail for the His-Δ41 variant. His-SUMODHCR24Δ26 purification (Fig 2.3.15 panel B) was done eluting proteins with a discontinuous gradient of imidazole and, as observed for the pET derivatives, also in this case the most of the DHCR24 protein form did not bind to the resin and eluted in the flow-through, as confirmed by western blot (Figure 2.3.15 panel C). Similar results were obtained for the other DHCR24 variants. A protein species with the expected mass of approximately 70 kDa was present in the fractions eluted with 0.5 M imidazole, but no flavin signal was associated to it.

Screening for activity of the expressed DHCR24 forms

It has been proposed that Seladin-1/DHCR24 catalyzes the reduction of the Δ^{24} double bond of the precursors of the cholesterol in its biosynthesis pathways. DHCR24 should convert desmosterol in cholesterol (Figure 2.1.3), using NADPH as reductant (Waterham et al, 2001). Attempts were done to measure the NADPH oxidation reaction in the presence of the crude extract from *E. coli* cells producing the His-DHCR24Δ41 variant. NADPH consumption was monitored at 340 nm in 25 mM sodium phosphate buffer, pH 8.0 at 25°C. No activity was detected, even at the presence of 105 μM desmosterol.

Alternatively, enzymatically produced cholesterol could be coupled with the cholesterol oxidase reaction. Cholesterol oxidase converts cholesterol in cholest-4-ene-3-one producing H_2O_2 in the presence of O_2. Thus, the DHCR24 reaction could be monitored spectrophotometrically by measuring the oxidation of a chromogen, such as o-dianisidine, catalyzed by the horse radish peroxidase (HRP), with consumption of H_2O_2 (Fig 2.3.16). In the set up of these assays, cholesterol and desmosterol solutions (420 μM stock) were prepared in 1.25% β-cyclodextrin. Assays were carried out using 5 μg of HRP. The o-dianisidine (0.4 mM) oxidation was monitored at 436 nm (ε = 11.6 mM^{-1} cm^{-1}; Vanoni and Curti, 2007) in 50 mM Tris/HCl buffer, pH 7.2 (Waterham et al, 2001), at 25°C, in the presence of 44 μM H_2O_2. In these conditions, o-dianisidine is completely oxidized within 1 min (Figure 2.3.17 panel A). The effect of β-cyclodextrin and of cholesterol (105 μM) on the HRP reaction was also monitored. Cholesterol did not affect the HRP reaction (Figure 2.3.17 panel B), except for an initial variation in the absorbance due to β-cyclodextrin. The coupled cholesterol oxidase (CO) activity was monitored in the presence of HRP, o-dianisidine and 105 μM cholesterol and desmosterol. As shown in figure 2.3.17 also desmosterol is an excellent substrate of cholesterol oxidase ruling out the possibility to use this enzyme to detect the desmosterol oxidase activity of DHCR24.

For this reason, the gas-chromatography detection of the enzyme-catalysed conversion of desmosterol to cholesterol was studied. Preliminary experiments were done by adding known amounts of desmosterol or cholesterol to crude extracts of *E. coli* Rosetta cells transformed with the pET vector and grown under the same conditions as those used to produce the soluble DHCR24Δ41. After extraction with petroleum ether, sterols were derivatised with N,O-Bistrimethylsilyl) trifluoroacetamide (BSTFA):pyridine. The samples were analysed by GC/MS. Recovery (50-70%) and sensitivity (2 pmol) were satisfactory and there was no interference from the *E. coli* extracts. Conversion of desmosterol to cholesterol was assayed on homogenates and crude extracts of cells containing His-DHCR24Δ41 using a NADPH-regenerating system formed by glucose 6-phosphate and glucose 6-phosphate dehydrogenase. Control experiments were done in

the absence of the reducing system, and samples were analysed after 1 and 6 h of incubation. Essentially, no cholesterol production was observed. Due to the fact that GC analyses are very labour intensive, similar assays with the other DHCR24 truncated forms were not carried out. However, this assay will be soon performed with *S. cerevisiae* extracts as a starting point for new experiments.

2.4 CONCLUSIONS

The expression in *E. coli* and the purification of soluble forms of the novel human antiapoptotic factor Seladin-1/DHCR24 were attempted in order to obtain sufficient amount of homogeneous protein for its biochemical characterization. The DNA fragments that encoded protein forms missing the N-terminal putative transmembrane domain (Figure 2.1.4) were cloned into different expression vectors for the production of the enzyme forms in fusion with various tags and protein domains known to enhance production levels, folding and solubility of the target protein (Figure 2.3.1).

Preliminary expression experiments were carried out in a small scale in order to rapidly identify the conditions for the production of soluble Seladin-1/DHCR24 forms. After an initial screening of different strains, *E. coli Rosetta (DE3)* cells were selected as the host of various constructs. *E. coli* Rosetta (DE3) cells were transformed with the plasmid of interest and growth was done at 25°C until OD_{600} reached a value of 1. 0.1 mM IPTG was added and the culture was transferred at 15°C for 16 or 42 h..

His-DHCR24Δ26 and DHCR24Δ26-His forms had a very low or even no detectable level of protein, thus they were abandoned. On the contrary, His-DHCR24Δ41 and DHCR24Δ41-His variants showed good expression levels, with a detectable amount of soluble protein, in spite of the fact that most of the protein present was in inclusion bodies. The analytical purification of these two DHCR24 forms by Ni-NTA Sepharose chromatography showed that only a small fraction of soluble DHCR24 bound to the resin and eluted with 100 mM imidazole, in association to a flavin signal. In order to increase the amount of protein able to bind the Ni-NTA resin, a pre-treatment of the cells by osmotic shock was attempted (Magnusdottir et al, 2009), with no substantial improvement of the amount of bound DHCR24. The N-terminal sequencing of the His-Δ41 variant confirmed the presence of the His-tag at the N-terminus of the protein produced in *E. coli*, suggesting that either the protein undergoes modifications at the N-terminus during the purification procedure, or that the soluble fraction of the enzyme is actually characterized by large aggregates, that could not be solubilized even using detergents. Similar results were obtained with small scale purifications on anionic and cationic exchange resins. Also in these cases the DHCR24 forms did not bind the resin, indicating that large aggregates are formed that cannot interact with the functional groups of the resins.

The coelution of DHCR24Δ41 His-tagged forms with a flavin signal led us to produce other protein variants, in order to improve the solubility of the protein by identifying the boundary of the soluble (catalytic) domain. Expression of His-tagged forms of DHCR24Δ33 and –Δ50 were carried out using the same strategy as that adopted for Δ41. N-terminal His-tagged forms showed expression

levels similar to those observed for His-Δ41 and Δ41-His, with a detectable amount of soluble protein. On the contrary, plasmids encoding the protein forms with C-terminal His-tags were mildly toxic for *E. coli* cells, and the amount of protein detected in total extracts was very low. The purification of these DHCR24 variants was carried out as for His-DHCR24Δ41, with essentially identical results. In particular, we confirmed that most of the protein did not bind to the resin and that a flavin signal coeluted with the enzyme. A complete purification of the 50 kDa flavin-associated protein was carried out using that had overproduced DHCR24Δ50. The purified protein was identified as the flavoprotein subunit of *E. coli* alchil-hydroperoxide reductase (AhpF, 56 kDa), while the DHCR24Δ50 variant was obtained as a greater than 100 kDa colourless protein. This result may suggest that or DHCR24 is not a flavoprotein, or, more likely, that the forms we producd so far do not correspond to the complete soluble catalytic domain of the holoenzyme.

Alternative strategies for the expression of soluble DHCR24 forms were tested. The production of DHCR24 variants as pGEX-4T-1 and pMAL-c derivatives led to the obtainment of higher protein level in total cell extracts and an increase of solubility, the latter for constructs in fusion with MBP. Small scale affinity chromatography of extracts on glutathionyl-Sepharose showed that the GST-DHCR24 variants did not bind to the resin. On the contrary, the MBP-DHCR24 forms were purified to near homogeneity by affinity chromatography on amylose column, but no flavin signal was associated to the native proteins that eluted from the column as a 20 MDa aggregates. The denaturation of MBP-DHCR24 solutions by incubation at 100°C for 15 min in the dark led to the realese of a small amount of flavin that was confirmed to be 80% FAD fluorimetrically. However, it accounted for less than 1% of the expected amount estimated from the quantity of DHCR24 present in the sample if DHCR24 was a properly folded protein.

Expression of DHCR24 truncated forms in fusion with His-SUMO protein at the N-terminus was done in order to increase the solubility and the folding levels of the proteins, as reported in (Butt et al, 2005; Malakhov et al, 2004; Marblestone et al, 2006). This strategy could also facilitate the subsequent protein purification by mean of Nickel chelate affinity chromatography. The presence of a correctly folded linker (the SUMO protein) between the N-terminal His-tag and the DHCR24 form should avoid masking of the His-tag by DHCR24 and should decrease the probability to form high molecular aggregates. The expression of His-SUMODHCR24Δn proteins in *E. coli* led to an increased amount of protein in cell total extracts, but, as observed for the His-tagged variants, most of the protein was present in the insoluble fraction. Also in this case most of the DHCR24 protein forms did not bind to the resin and eluted in the flow-through.

Experiments aimed to set up activity assays for Seladin-1 and its truncated variants have been initiated. First of all, to test if NADPH is a substrate of DHCR24, NADPH oxidation assays on

crude extracts containing His-DHCR24Δ41 were carried out in 20 mM Hepes/KOH buffer, pH 7.0, at 25°C. In the presence of 100 μM NAPDH, the observed activity was very low, probably due to the *E. coli* background, and no effects were observed upon addition of 420 μM desmosterol. Attempts to set up desmosterol reduction assays have also been done. In theory, the synthesis of cholesterol by Seladin-1 could be monitored by coupling this reaction with that of cholesterol oxidase, which produces H_2O_2. The oxidation of H_2O_2 to H_2O catalyzed by horse radish peroxidase in the presence of o-dianisidine could be monitored at 436 nm. However, we showed that it is not a possible assay, because desmosterol is also an excellent substrate of cholesterol oxidase. For this reason, the gas-chromatography detection of the enzyme-catalysed conversion of desmosterol to cholesterol was tested on homogenates and crude extracts of cells containing His-DHCR24Δ41 using a NADPH-regenerating system formed by glucose 6-phosphate and glucose 6-phosphate dehydrogenase. However, no cholesterol production was observed.

The results obtained for the production of human Seladin-1 highlighted the difficulties that often are encountered with the heterologous expression of membrane proteins in prokaryotic systems. Adopting strategies aimed to improve the correct folding of the protein, such as removal of transmembrane portions, fusion with soluble tags and circumventing the codon bias by expression in *E. coli* Rosetta (DE3) cells, led to the obtainment of low amount of soluble protein, that however was produced in an aggregate form. For this reason, experiments aimed at the production of Seladin-1/DHCR24 in a eukaryotic system, such as yeast, have been initiated in our laboratory, with the optimization of methods to carry out expression in different *S. cerevisiae* background and to analyze the resulting material. Furthermore, *S. cerevisiae* extracts will be used to perform activity assays to reproduce Waterham et al. results (Waterham et al, 2001). Together with this line of research, the study of another human medically-relevant human flavoenzyme has been initiated in our laboratory. The production , kinetic and spectroscopic characterization of MICAL N-terminal flavoprotein domain will be discussed in the next chapter.

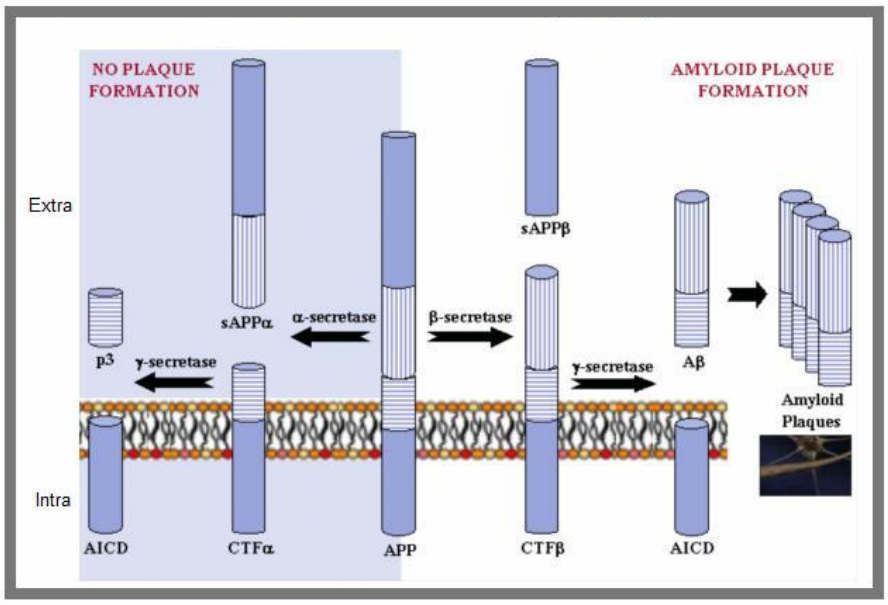

Figure 2.1.1: Secretase mediate APP processing. In non-amyloidogenic pathaway, α-secretase and γ-secretase produce the p3 soluble peptide and a membrane-bond domain (AICD). In the amyloidogenic pathway, the β-secretase and γ-secretase combined action leads to Aβ-amyloids formation (from www.ebi.ac.uk/interpro/potm/2006_7/Page2.htm).

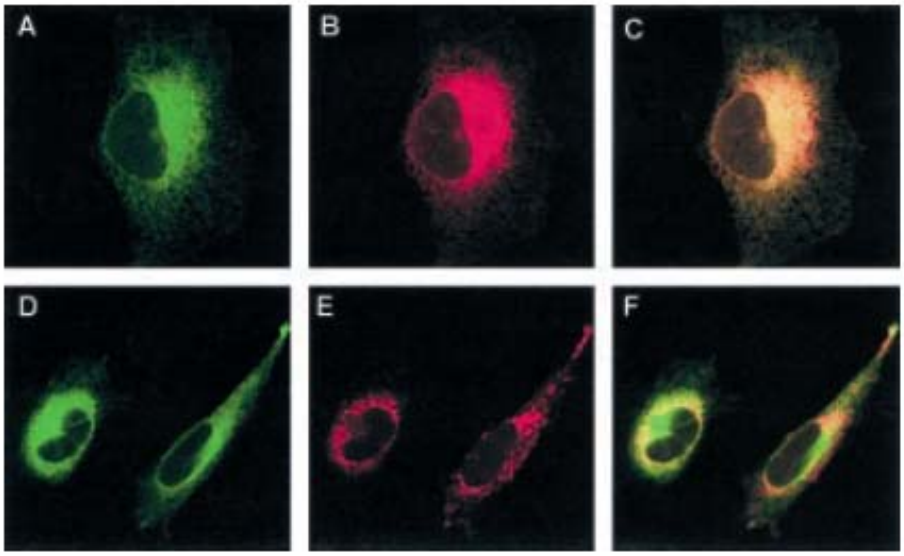

Figure 2.1.2: Subcellular localization of Seladin-1 in human neuroglioma cells. Panel A and D: Subcellular distribution of the Seladin-1/enhanced green fluorescent protein (EGFP) fusion protein. Panel B: Staining of the endoplasmic reticulum. Panel C: Overlay from A and B shows the colocalization of Seladin-1 with the ER marker, indicated by yellow fluorescence. Panel E: Staining of the mitochondria. Panel F: Overlay of D and E (Greeve et al, 2000).

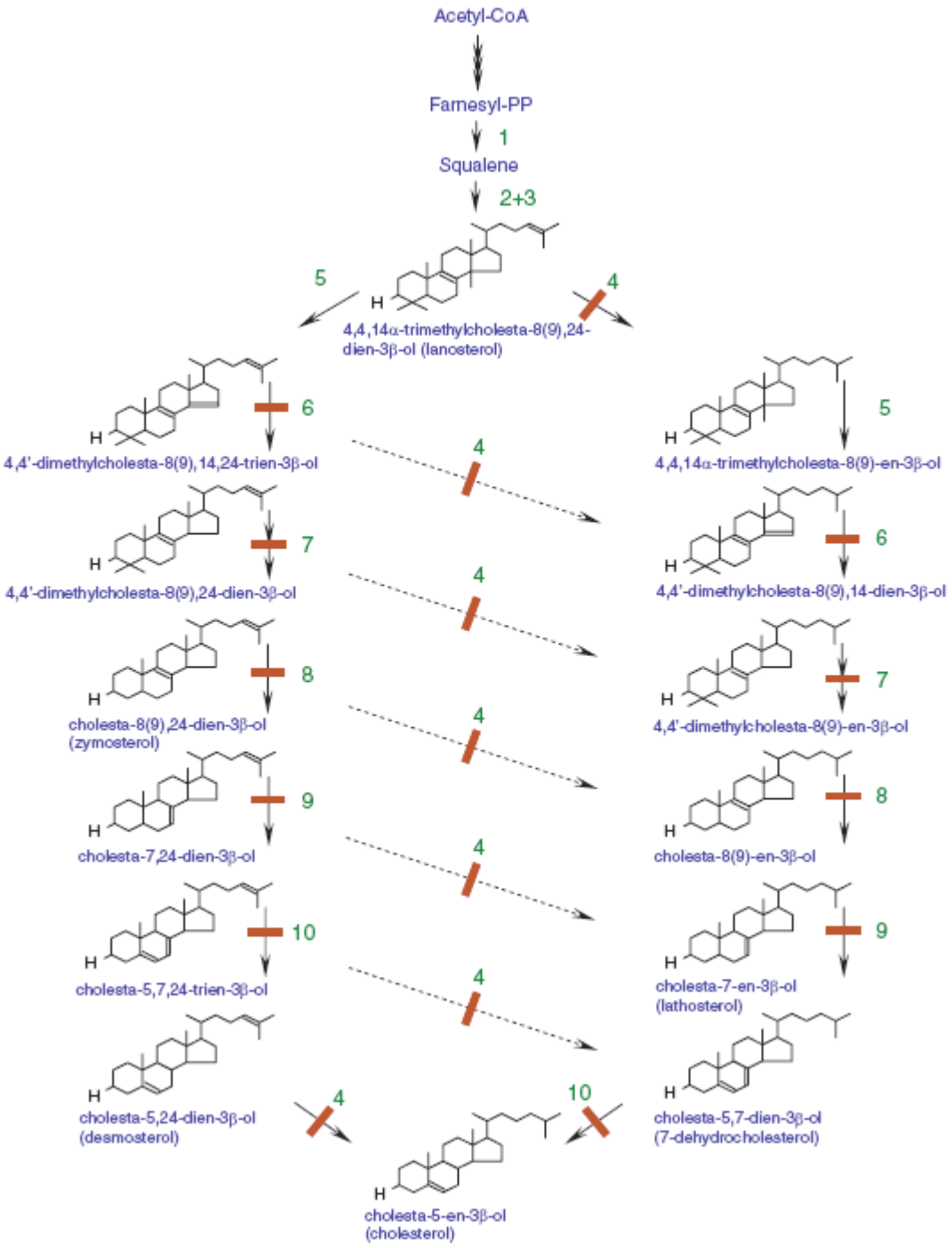

Figure 2.1.3: Cholesterol biosynthesis. After cyclization of squalene (composed of six isoprene units) lanosterol is synthesized. It is converted into cholesterol in a series of enzyme reactions requiring one demethylation at C-14, two demethylations at C-4, one isomerization of the $\Delta^{8(9)}$ double bond to Δ^{7}, three reductions of the Δ^{24}, Δ^{14} and Δ^{7} double bonds, and one desaturation between C-5 and C-6. indicated are two major routes involved in cholesterol synthesis. In this segment of the pathway six inherited disorders have been linked to specific enzyme deficiencies (indicated by red solid bars in the scheme and indicated in parenthesis below). Numbering of the enzymes: 1, squalene synthase; 2, squalene epoxidase; 3, 2,3-oxidosqualene sterol cyclase; 4, sterol Δ^{24}-reductase (DHCR24, desmosterolosis); 5, sterol C-14 demethylase; 6, sterol Δ^{14}-reductase (hydrops-ectopic calcificatio-moth-eaten skeletal dysplasia, HEM); 7, sterol C-4 demethylase complex (including 3β-hydroxysterol dehydrogenase defective in CHILD syndrome); 8, sterol Δ^{8}- Δ^{7} isomerase (X-linked dominated chondrodyslasia punctata 2, CDPX2); 9, sterol Δ^{5}-desaturase (lathosterolosis); 10, sterol Δ^{7}-reductase (Smith-Lemli-Opitz syndrome syndrome, SLO).

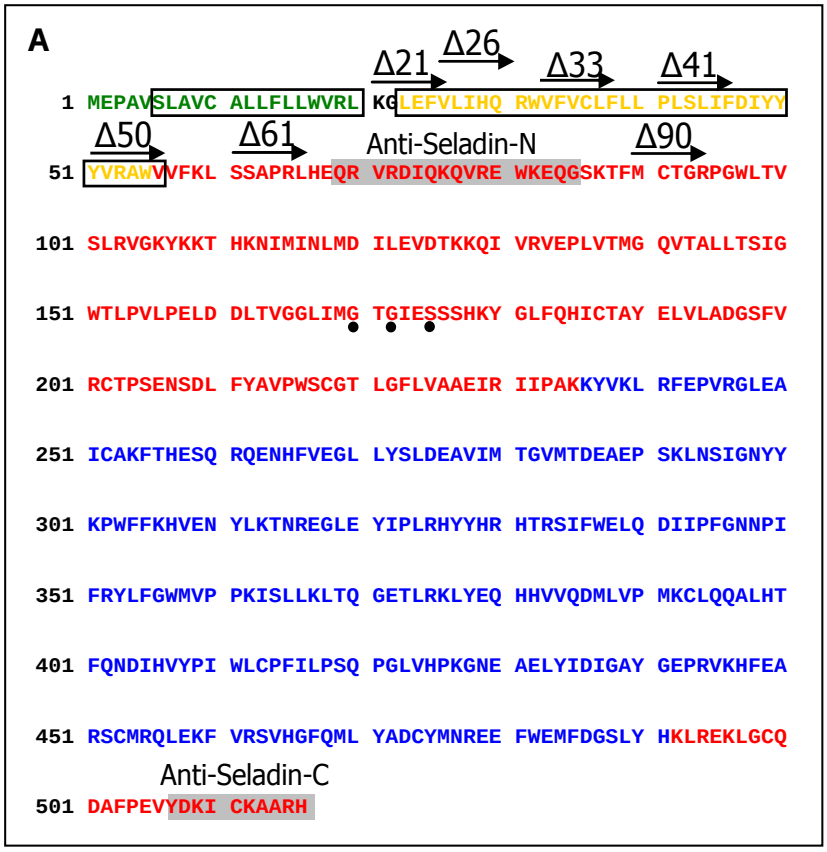

Figure 2.1.4: Primary structure and in silico model of human Seladin-1/DHCR24. Panel A: Green, putative signal peptide overlapping with the first transmembrane helix (boxed); yellow and boxed, putative second transmembrane helix; red, N- and C-terminal parts of the putative FAD-binding domain. The GXGXXS motif identifying the putative adenylate-binding site is marked with dots. The sequences recognized by the commercial Anti-Seladin-N and –C antibodies are highlighted in grey. The arrows indicate the starting point of truncated mutants generated for the production in *E. coli* (see also figure 2.3.1). Panel B: Seladin-1 model built using as template the structure of cytokinine dehydrogenase (Pedretti et al, 2008). Red, FAD-binding domain; blue, substrate binding domain; yellow, putative transmembrane region.

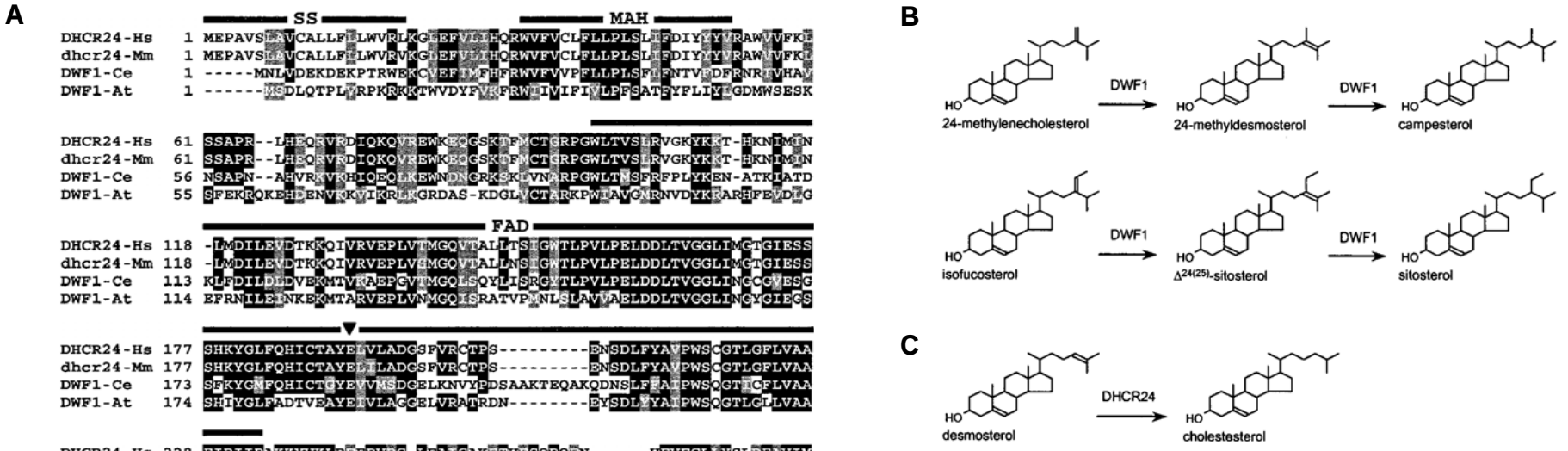

Figure 2.1.5 Panel A: Sequence alignment of human (Hs) DHCR24 and its orthologs in mouse (Mm), *C. elegans* (Ce) and *A. thaliana* (At). Only amino acids that are identical and conserved in at least three sequences are indicated, by black boxes and gray boxes, respectively. Indicated above the DHCR24 sequence are conserved domains predicted to encode a secretory-signal sequence (SS), and FAD-binding domain characteristics of the family of FAD-dependent oxidoreductases (FAD) and a membrane-associated helix (MAH). Panel B and C: Sterol/steroid biosynthesis in plant and human. Panel B: DIMINUTO/DWARF1 (DWF1) function in the biosynthetic pathway for plant sterols and steroids (brassinolide). The enzyme catalyzes both the isomerisation of $\Delta^{24(28)}$ bond into a $\Delta^{24(25)}$ bond and the subsequent reduction of $\Delta^{24(25)}$ bond from plant-sterol intermediates 24-methylenecholesterol and isofucosterol, to produce campesterol (plant-steroid precursor) and sitosterol (major plant sterol), respectively. Panel C: DHCR24 catalyzes the reduction of Δ^{24} bond of desmosterol to produce of cholesterol (Waterham, 2001).

PROTEIN	Kb	AA	kDa	Construct	Expressed	Soluble		Flavin
DHCR24	1551	516	60.1					
GST-DHCR24	2268	755	87.8		±, mildly toxic	NO	abandoned	
Trx-DHCR24	1953	659	74.3		NO, toxic	N/A	abandoned	
His-DHCR24	1620	539	62.8		NO, toxic	N/A	abandoned	
DHCR24-His	1578	525	61.2		NO, toxic	N/A	abandoned	
DHCR24Δ21-His	1518	505	58.9		NO, very toxic	N/A	abandoned	
DHCR24Δ26-His	1497	498	58.2		NO	N/A	abandoned	
His-DHCR24Δ26	1539	512	59.5		YES	-	abandoned	
MBP-DHCR24Δ26	2631	878	99.4		YES	±	purified on amylose resin	NO
GST-DHCR24Δ26	2181	726	84.6		YES	+	does not bind to GSH seph	
His-SUMO-DHCR24Δ26	1848	615	71.1		YES	++	partially purified on Ni-NTA	NO
DHCR24Δ33-His	1476	492	57.3		YES, mildly toxic	±	partially purified on Ni-NTA	YES
His-DHCR24Δ33	1521	506	58.7		YES	±	partially purified on Ni-NTA	YES
MBP-DHCR24Δ33	2613	870	98.6		YES	+	purified on amylose resin	YES
GST-DHCR24Δ33	2163	720	83.8		YES	±	does not bind to GSH seph	
His-SUMO-DHCR24Δ33	1830	609	70.3		YES	+	partially purified on Ni-NTA	NO
DHCR24Δ41-His	1452	483	56.3		YES, mildly toxic	+	partially purified on Ni-NTA	YES
His-DHCR24Δ41	1494	497	57.7		YES	+	partially purified on Ni-NTA	YES
MBP-DHCR24Δ41	2592	863	97.8		YES	++	purified on amylose resin	YES
GST-DHCR24Δ41	2142	713	83		YES	±	does not bind to GSH seph	
His-SUMO-DHCR24Δ41	1803	600	69.3		YES	++	partially purified on Ni-NTA	NO
DHCR24Δ50-His	1425	474	55.1		YES, mildly toxic	±	partially purified on Ni-NTA	YES
His-DHCR24Δ50	1467	488	56.5		YES	±	partially purified on Ni-NTA	YES
MBP-DHCR24Δ50	2562	853	96.6		YES	++	purified on amylose resin	YES
GST-DHCR24Δ50	2112	703	81.8		YES	+	does not bind to GSH seph	
His-SUMO-DHCR24Δ50	1776	591	68.1		YES	+	partially purified on Ni-NTA	NO
DHCR24Δ61-His	1398	465	54		YES	±	purified on Ni-NTA	NO
DHCR24Δ90-His	1311	436	50.5		YES	-	abandoned	

Figure 2.3.1: Summary of experiments for the expression of DHCR24 forms in *E. coli*. The putative transmembrane regions of DHCR24 are in red, the putative soluble domain in yellow. Colour code of fused peptides or domains: GST, green; Trx, light blue; His-tag, grey; MBP, orange; SUMO protein, blue.

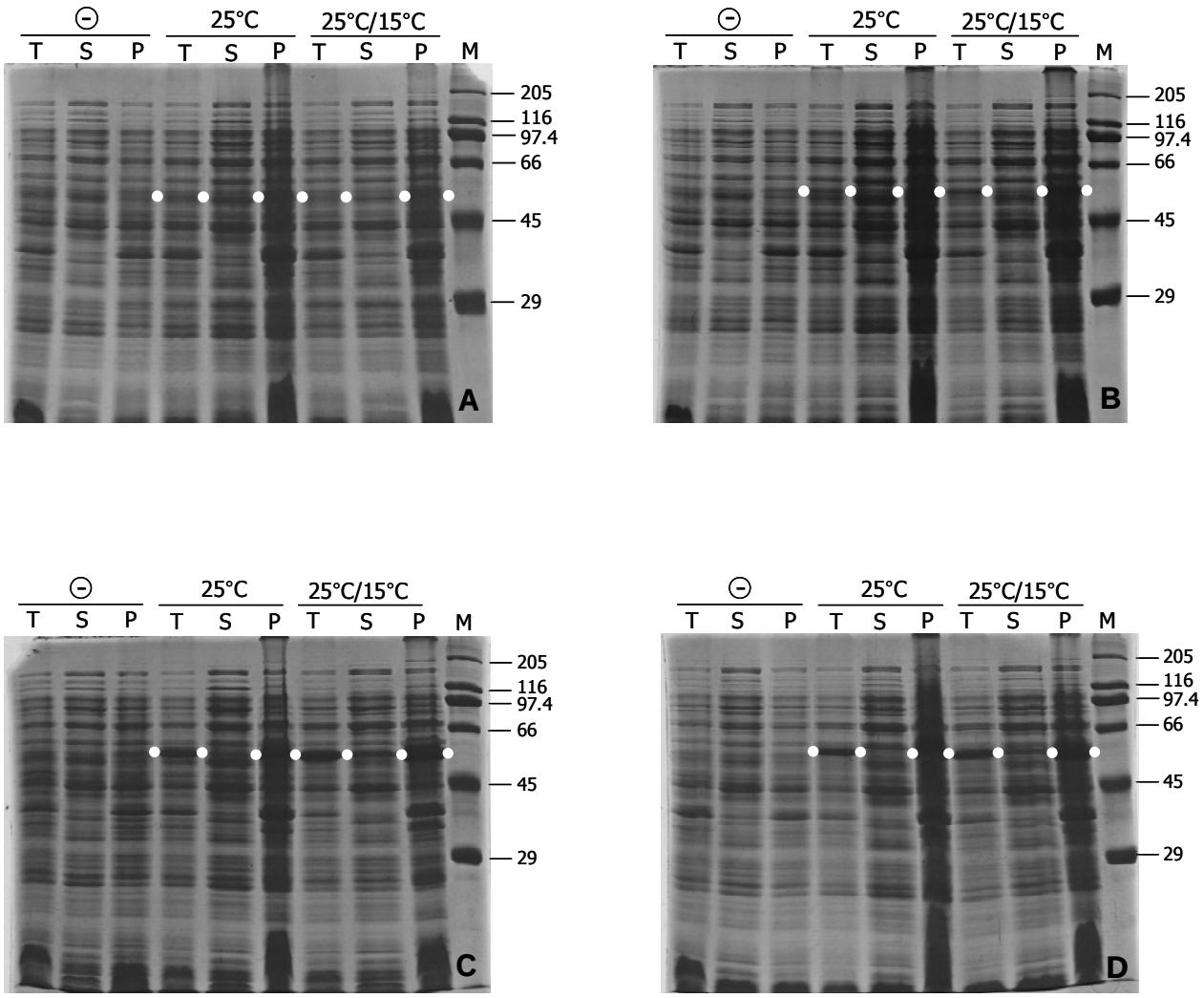

Figure 2.3.2: SDS-PAGE of total extracts (T), soluble (S) and insoluble (P) fractions of *E. coli* Rosetta (DE3) cells transformed with: pET23b (panel A and C; -) pET28b (panel B and D; -); pET23bDHCR24Δ26 (panel A); pET28bDHCR24Δ26 (panel B); pET23bDHCR24Δ41 (panel C); pET28bDHCR24Δ41 (panel D). Cells were grown at 25°C until the OD_{600} reached a valued of 1. IPTG (0.1 mM) was added to the cultures that were maintained at 25°C or shifted at 15°C. Cells were harvested after 16 h. M: markers. White dots indicate the expected position for the Δ26-His (58.2 kDa), His-Δ26 (59.5 kDa), Δ41-His (56.3 kDa) and His-Δ41 (57.7 kDa) proteins.

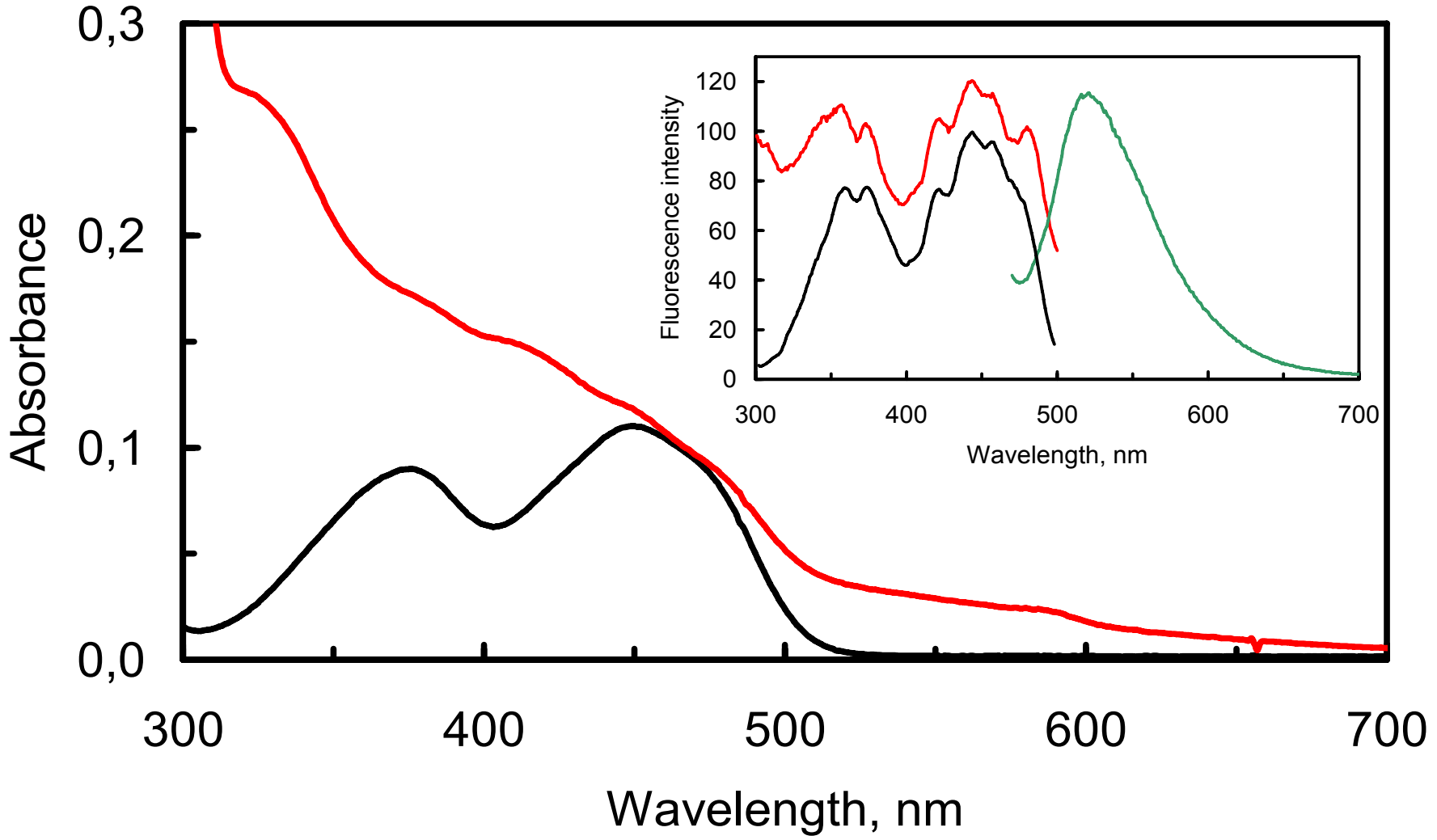

Figure 2.3.3: **Analytical purification of His-Δ41 on Ni-NTA Sepharose.** Main panel: Absorbance spectrum of the fraction eluted with 100 mM imidazole and containing His-DHCR24Δ41 (Red) and absorbance spectrum of 1 μM FAD (Black). Inset: exctitation (λ_{ex}, 300-500 nm; λ_{em}, 520 nm) and emission (λ_{ex} 450 nm; λ_{em}, 470-700 nm) spectra of the sample.

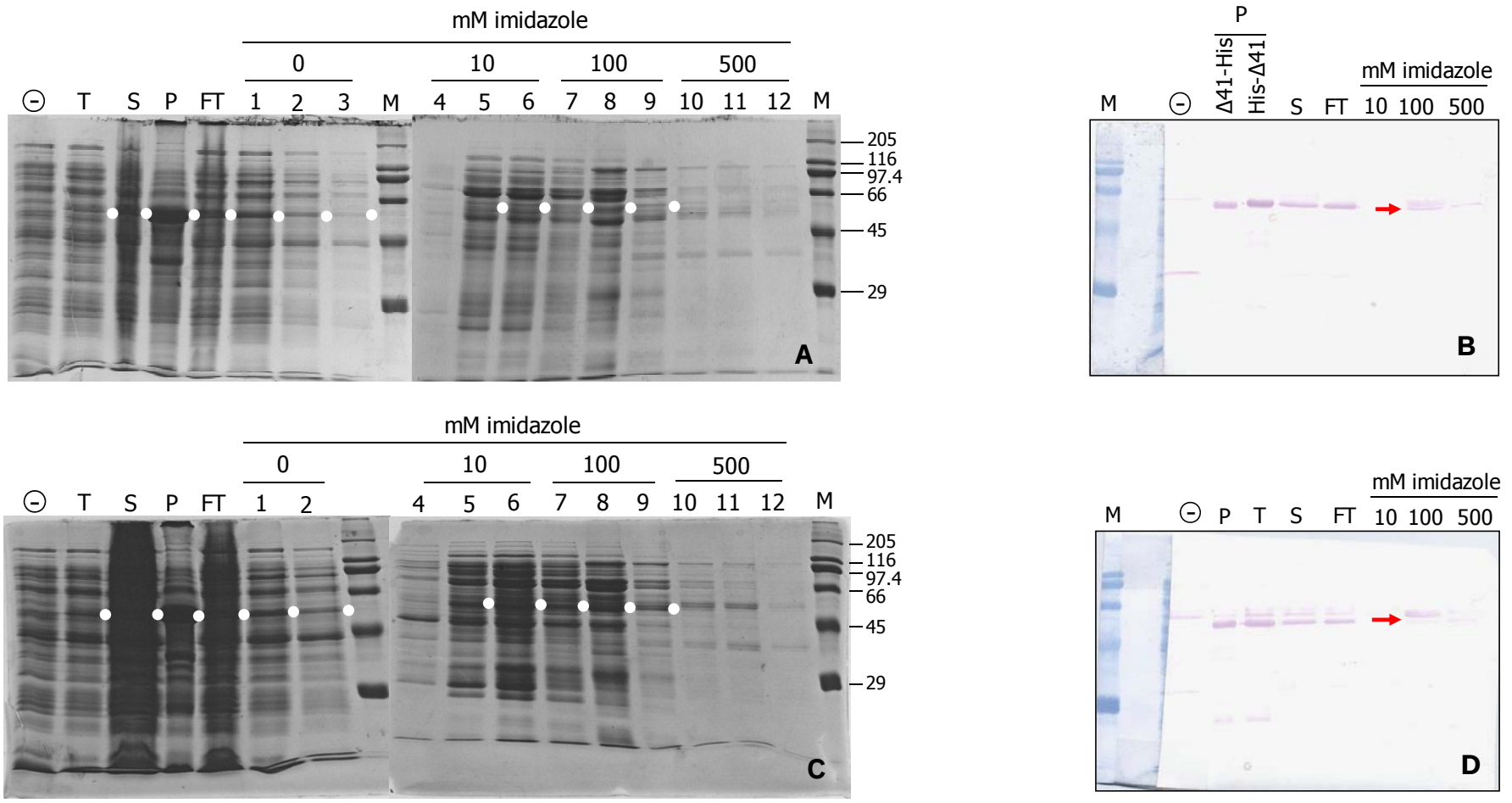

Figure 2.3.4: Analytical purification of His-Δ41 and Δ41-His on Ni-NTA Sepharose. SDS-PAGE of total extracts (T), soluble (S, 40 µg) and insoluble fractions of *E. coli* Rosetta (DE3) cells transformed with pET28DHCR24Δ41 (panel A) and pET23DHCR24Δ41 (panel C). Cells were grown at 25°C, induced with 0.1 mM IPTG (-) and transferred at 15°C. After 41 hours cells were harvested. Crude extracts were loaded on a 1 ml Ni-NTA Sepharose column equilibrated in buffer A and the flow-through (FT) was collected. Proteins were eluted with discontinuous gradient of imidazole (0, 10, 100 and 500 mM). Numbers indicate the corresponding fractions (20 µl each). White dots indicate the expected position for His-Δ41 (57.7 kDa) and Δ41-His and (56.3 kDa). Western-blot with immunodecoration with anti Seladin N-terminal antibodies. Arrows indicate the bands corresponding to the His-Δ41 (panel B) and Δ41-His (panel D). M: markers.

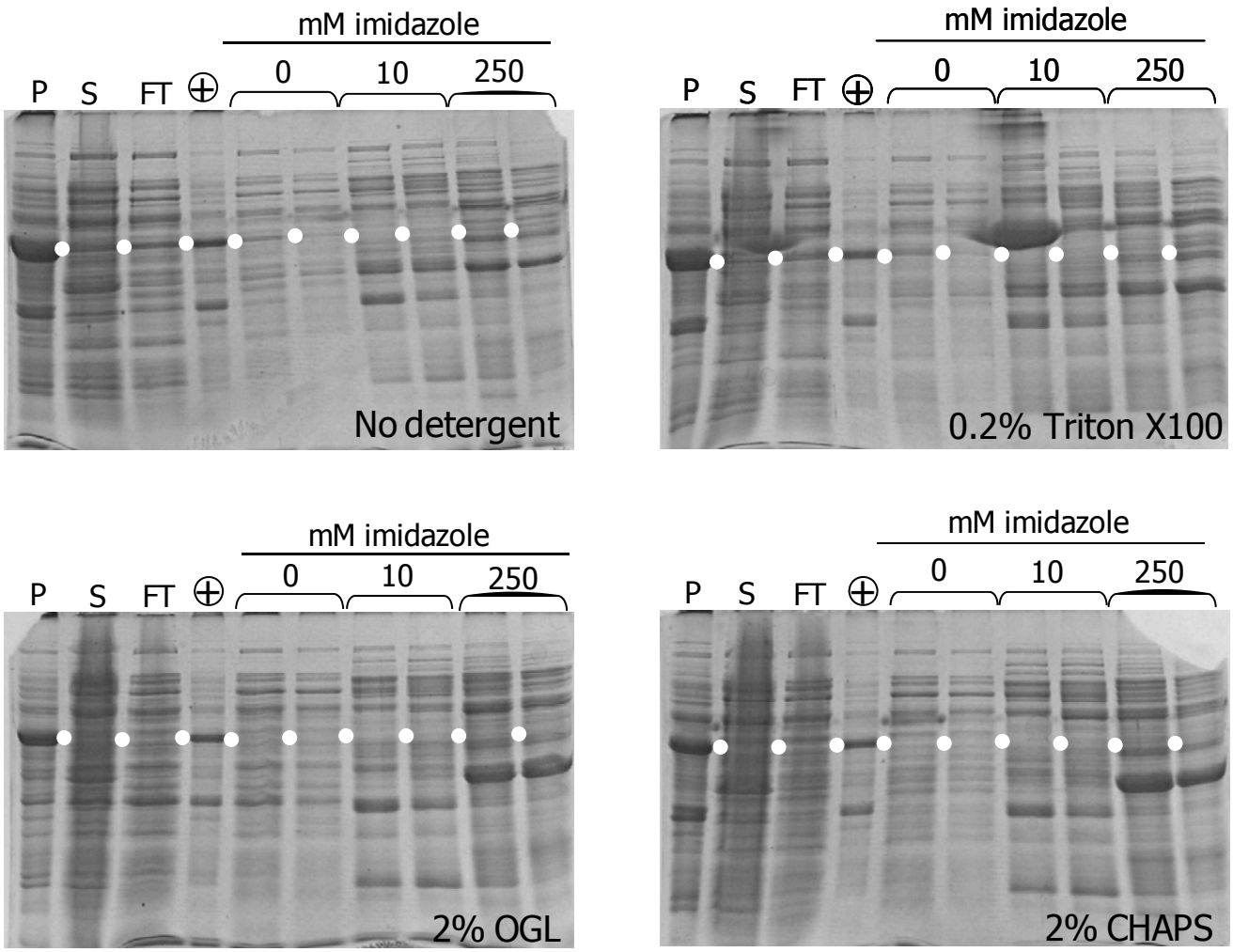

Figure 2.3.5: Analytical purification of His-DHCR24Δ41 on Ni-NTA Sepharose in the presence of detergents. SDS-PAGE of fractions eluted with a discontinuous gradient of imidazole (0, 10, 250 mM) from a 1 ml Ni-NTA Sepahrose column after incubation of crude extract with no detergent, 0.2% Triton X100, 2% octylglucoside (OGL) and 2% CHAPS. P: insoluble fraction; S: soluble fraction (40 µg); FT: flow-through (40 µg); +: insoluble fraction of cells expressing the His-Δ41 used as positive control; 0, 10, 250: peak fractions eluted with 0, 10 and 250 mM imidazole. White dots indicate the expected position for the His-DHCR24Δ41.

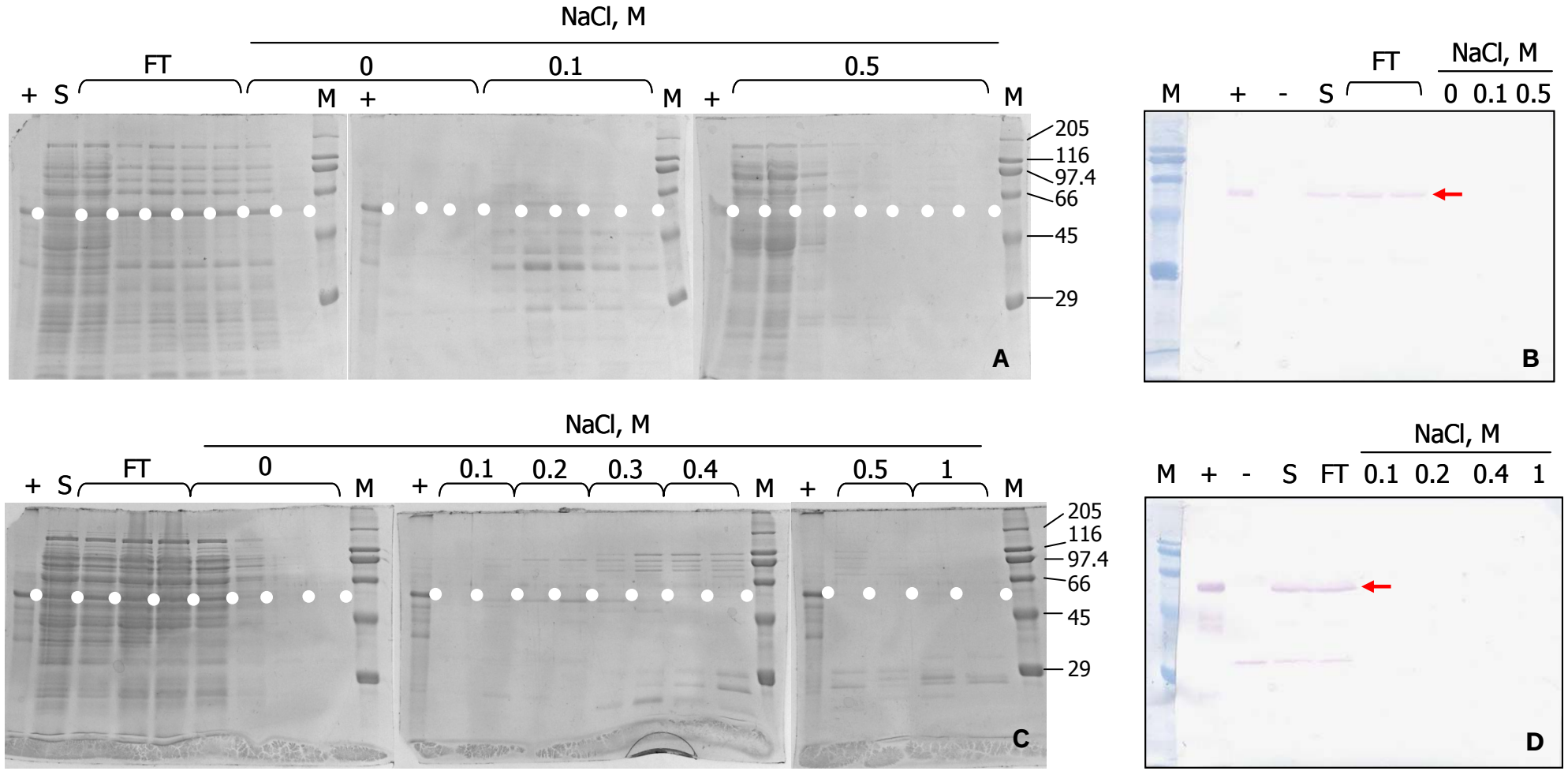

Figure 2.3.6: Purification of His-DHCR24Δ41 by ionic exchange chromatography. SDS-PAGE and Western-blot of fractions eluted from a 2 ml Q-Sepharose column (Panels A and B) and from a 2 ml SP-Sepharose column (Panel C and D) equilibrated in 20 mM phosphate, pH 8.0 and 20 mM phosphate, pH 7.0 buffers, respectively, and eluted with a discontinuous salt gradient. 1 gr of *E. coli* Rosetta (DE3) that had produced the His-DHCR24Δ41 was used for both purifications. Western-blots were decorated with anti-Seladin N-terminal antibodies. White dots indicate the expected position of His-Δ41; red arrow indicate the corresponding His-Δ41 band recognized by antibodies. +: insoluble fraction of cells expressing His-Δ41 used as a positive control; S: soluble fraction (40 µg); FT: flow-through; -: negative control; M: markers.

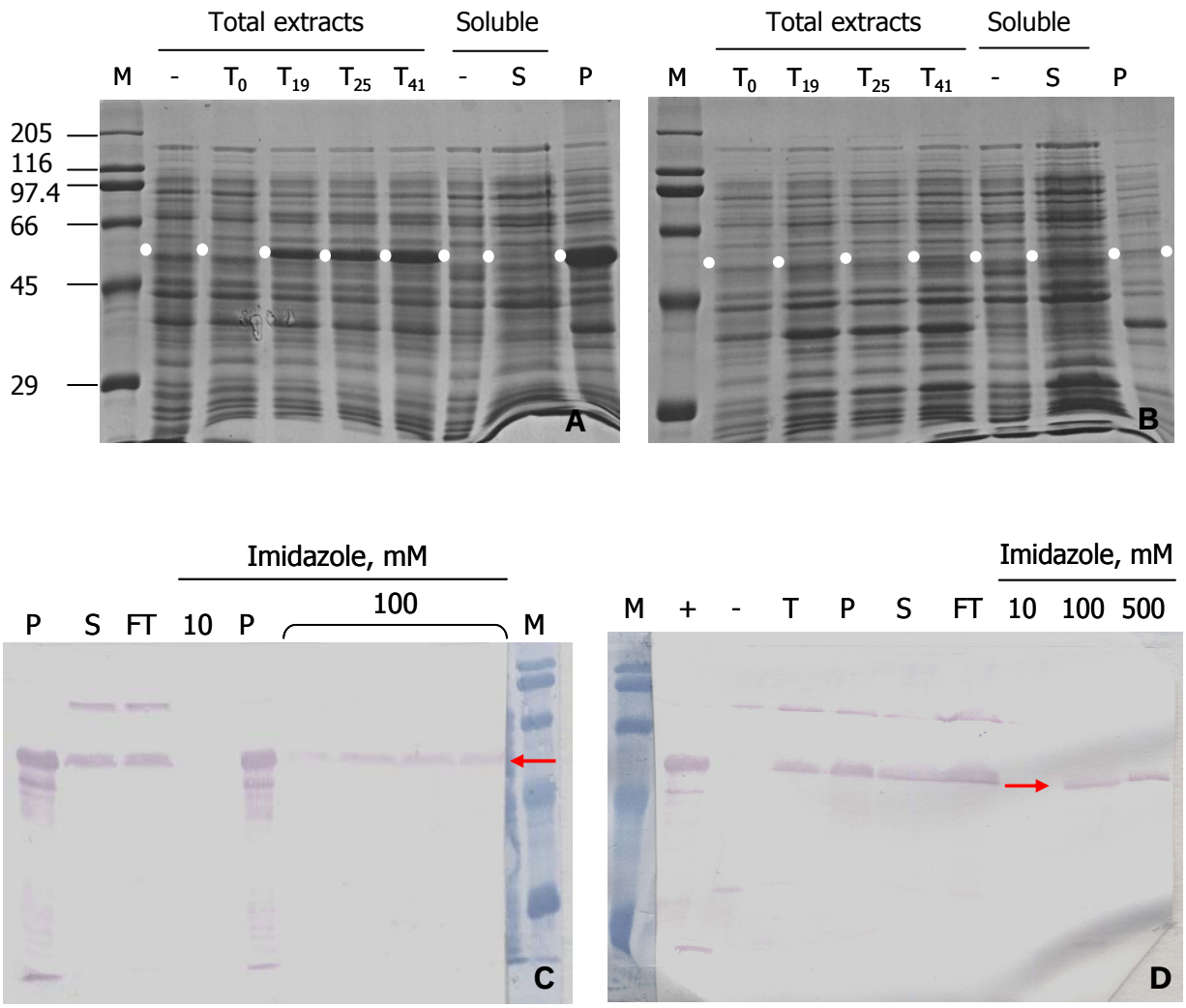

Figure 2.3.7: Expression of His-tagged forms of DHCR24Δ50 in *E. coli* Rosetta (DE3) cells and their analytical purification on Ni-NTA Sepharose column. SDS-PAGE of total and soluble extracts of cells containing pET28b (negative control, -), pET28bDHCR24Δ50 (Panel A) and pET23bDHCR24Δ50 (Panel B) grown at 25°C until OD_{600} reached a value of 1. 0.1 mM IPTG was added (T_0) and cells were transferred at 15°C. Cells aliquots were harvested at 19 (T_{19}), 25 (T_{25}) and 41 (T_{41}) hours after induction. S: soluble fraction; P: insoluble fraction. White dots indicate the expected position of His-Δ50 (56.5 kDa) and Δ50-His (55.1 kDa). Panels C and D: Western blot with anti-Seladin C-terminal antibodies of fractions collected during the analytical purification of His-Δ50 (panel C) and Δ50-His (panel D) on a 1 ml Ni-NTA Sepharose column. Elution was achieved with the indicated concentration of imidazole. FT: flow-through; +: insoluble fraction of cells expressing His-Δ41 used as positive control. The red arrows indicate the DHCR24Δ50 band.

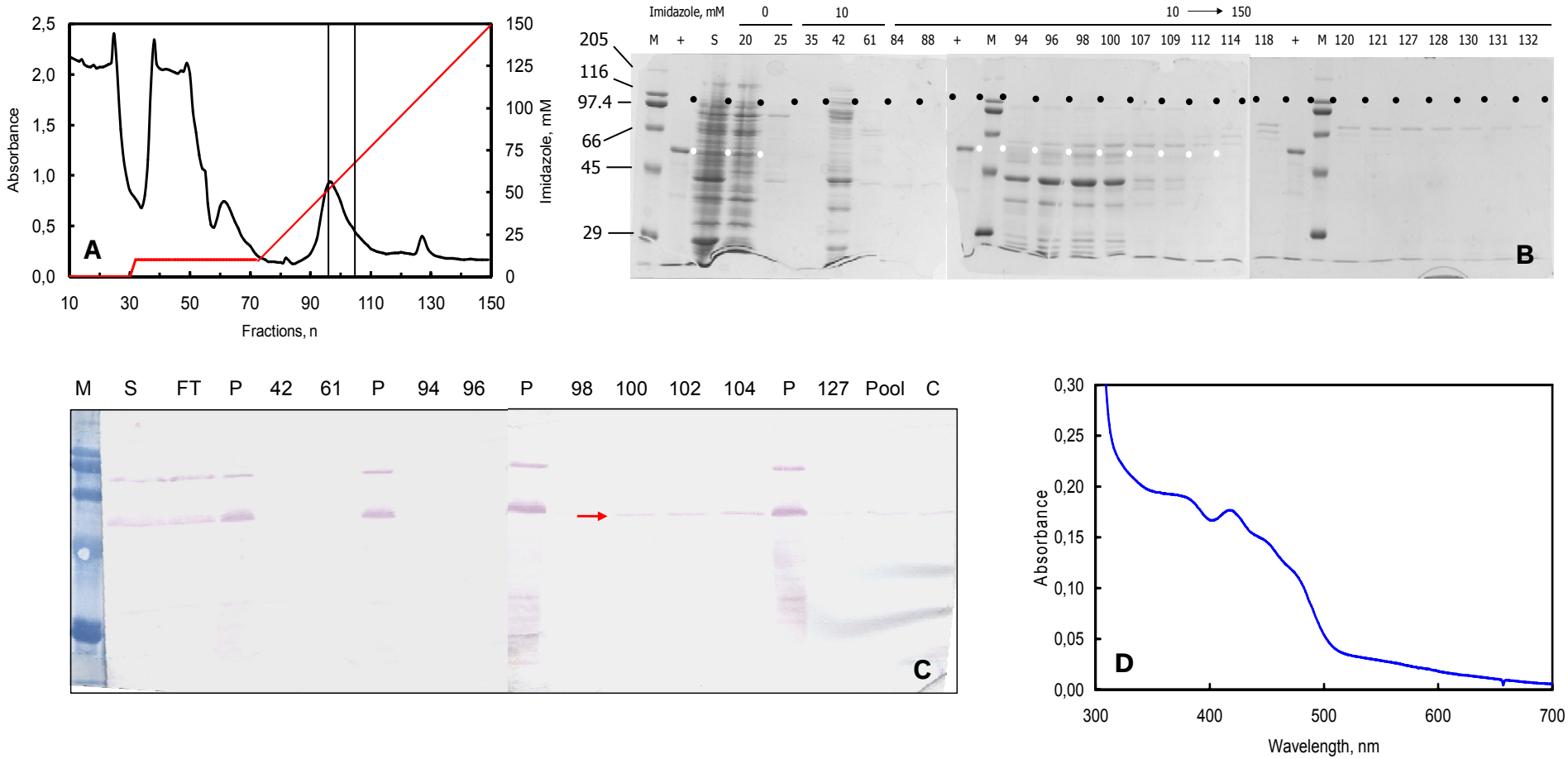

Figure 2.3.8: Purification of the flavoprotein responsible of the flavin signal associated to DHCR24Δ50-His. Affinity chromatography on Ni-NTA Sepharose. Crude extract from *E. coli* Rosetta (DE3) cells expressing the Δ50-His variant was loaded on a 20 ml Ni-NTA Sepharose column in buffer A. The column was developed with a 10-500 mM imidazole gradient (in 10 column volumes) (panel A). Vertical bars indicate fractions 96-104 which are associated to a flavin signal. Panel B: SDS-PAGE of fractions eluted from Ni-NTA Sepharose chromatography. M: markers; +: insoluble fraction of Δ50-His producing cells (positive control); S: crude extract. Black dots indicate the expected position of DHCR24Δ50. Panel C: Western-blot of fractions with anti-Seladin C-terminal antibodies. FT: flow-through; pool: pooled fractions 96-104; C:fractions 96-104 after concentration. The red arrow indicates the band corresponding to Δ50-His. Panel D: Absorbance spectrum of fractions 96-104 eluted from the Ni-NTA Sepharose column, pooled and concentrated by ultrafiltration.

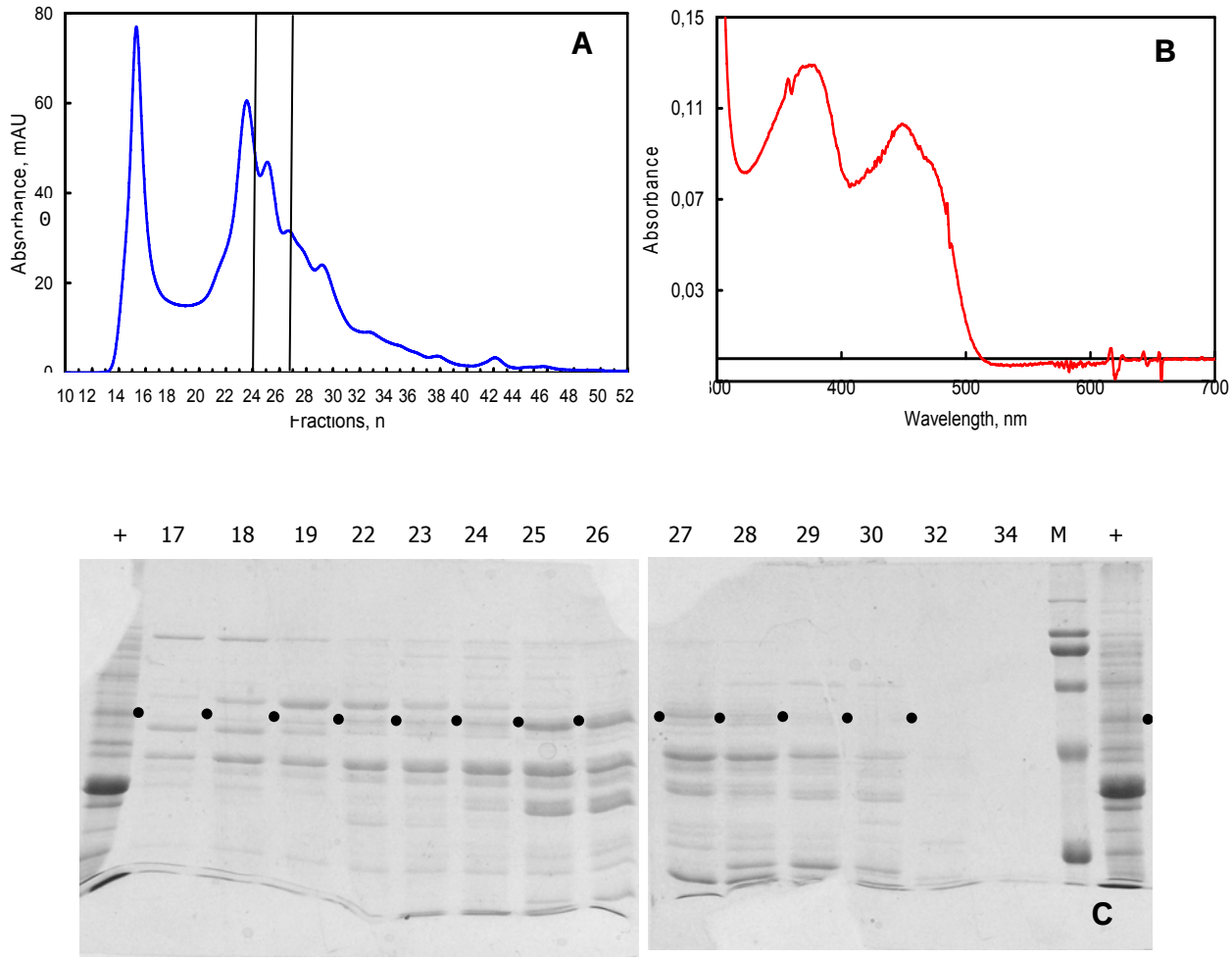

Figure 2.3.9: Purification of the flavoprotein responsible of the flavin signal associated to DHCR24Δ50-His. Gel filtration on Superose-12. Fractions 96-104 eluted from the Ni-NTA Sepharose column in figure 2.3.8 were concentrated and chromatographed on a Superose-12 column, equilibrated end eluted with buffer A (panel A). Vertical bars indicate fractions 25-27 that show a flavin signal. These fractions were pooled and concentrated. Panel B: Absorbance spectrum of fractions 25-27 after concentration. Panel C: SDS-PAGE of fractions collected during chromatography on Superose-12. M: markers; +: insoluble fraction of cells producing Δ50-His (positive control). Black dots indicate the expected position for DHCR24Δ50.

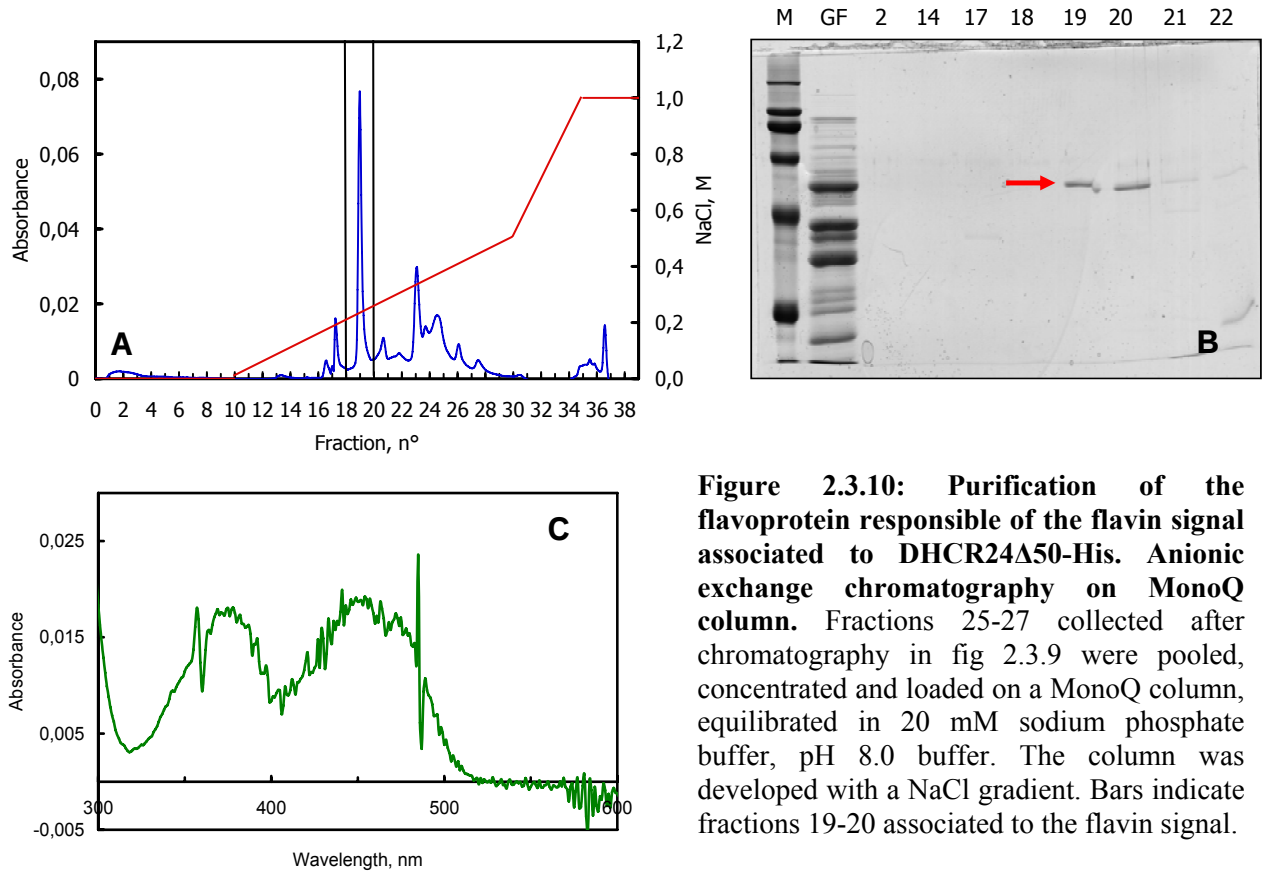

Figure 2.3.10: Purification of the flavoprotein responsible of the flavin signal associated to DHCR24Δ50-His. Anionic exchange chromatography on MonoQ column. Fractions 25-27 collected after chromatography in fig 2.3.9 were pooled, concentrated and loaded on a MonoQ column, equilibrated in 20 mM sodium phosphate buffer, pH 8.0 buffer. The column was developed with a NaCl gradient. Bars indicate fractions 19-20 associated to the flavin signal.

Panel B: SDS-PAGE of some fractions eluted from MonoQ chromatography. M: markers; GF: fraction 26 eluted from Superose-12 (positive control). Panel C: Absorbance spectrum of fractions 19-20 pooled and concentrated.

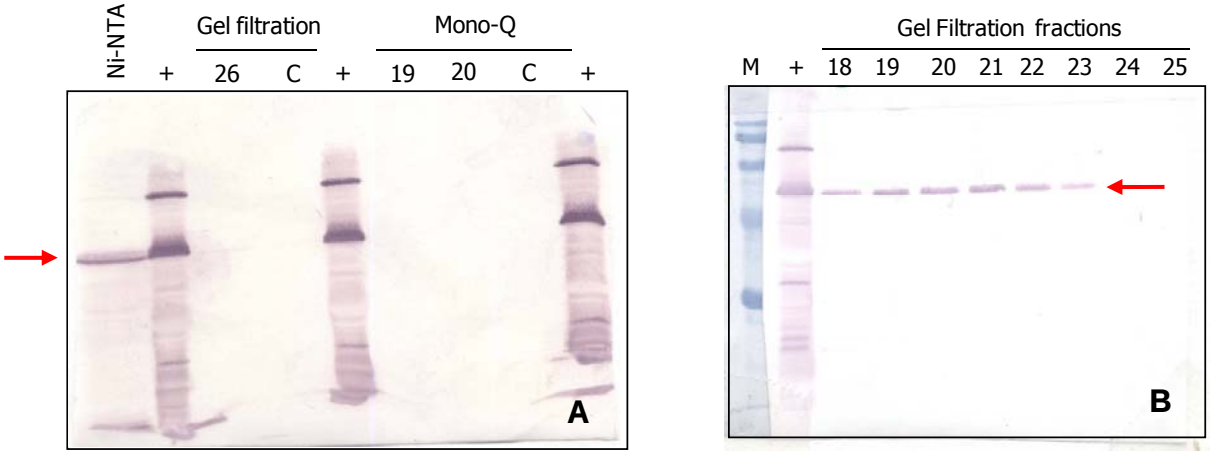

Figure 2.3.11: Western-blot of samples obtained during chromatographies shown in figures 2.3.8, 2.3.9, 2.3.10. Panel A: Ni-NTA: fractions 46-104 eluted from Ni-NTA Sepharose column, pooled and concentrated.. 26: fraction 26 eluted from Superose-12 column; C: samples of fractions associated to the flavin signal pooled and concentrated after the indicated chromatography step; 19, 20: fractions 19 and 20 eluted from MonoQ column. Panel B: Western-blot of fractions obtained during gel filtration on Superose-12. M: markers; +: insoluble fraction of cells producing Δ50-His (positive control). Red arrows indicate DHCR24Δ50-His.

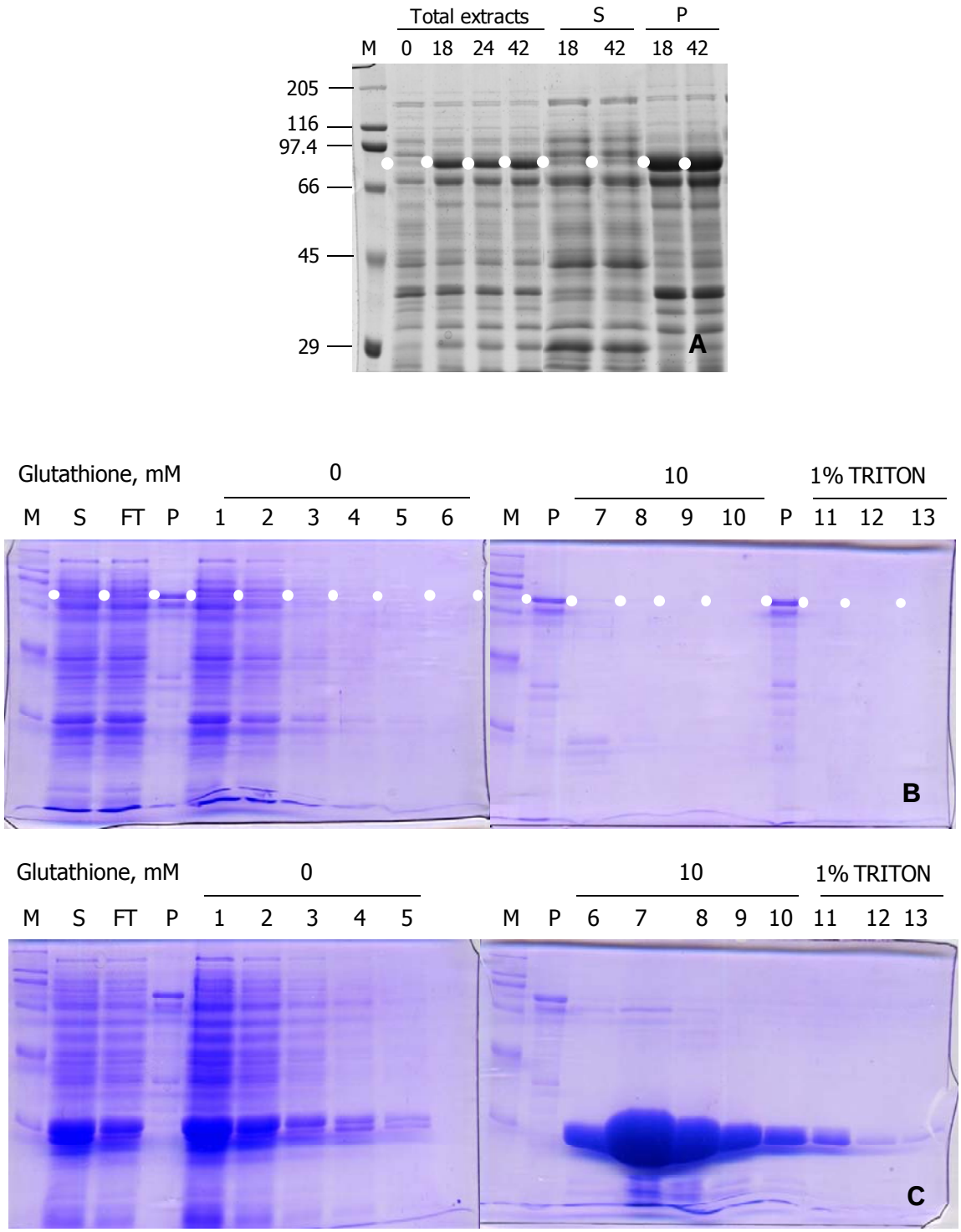

Figure 2.3.12: Expression of GST-DHCR24 variants and analytical purification attempts on a GSH-Sepharose column. Panel A: total extracts, soluble (S) and insoluble fractions (P) of *E. coli* cells transformed with pGEXDHCR24Δ26. Cells were grown at 15°C after induction with 0.1 mM IPTG (0) and aliquots were harvested after 18, 24 and 42 hours. Panel B: The crude extract of cells expressing GSTΔ33 was loaded on a 1 ml of GSH-Sepharose column equilibrated in PBS buffer (see text). Elution was carried out with PBS buffer containing 10 mM glutathione, with an additional wash with 1% Triton. Panel C: Purification of GST expressed in *E. coli* Rosetta cells (positive control). M: markers; FT: flow through, P: insoluble fraction (positive control). White dots indicate the expected position for the GSTΔ26 (84.6 kDa, panel A) and Δ33 (83.8 kDa, panel B) forms.

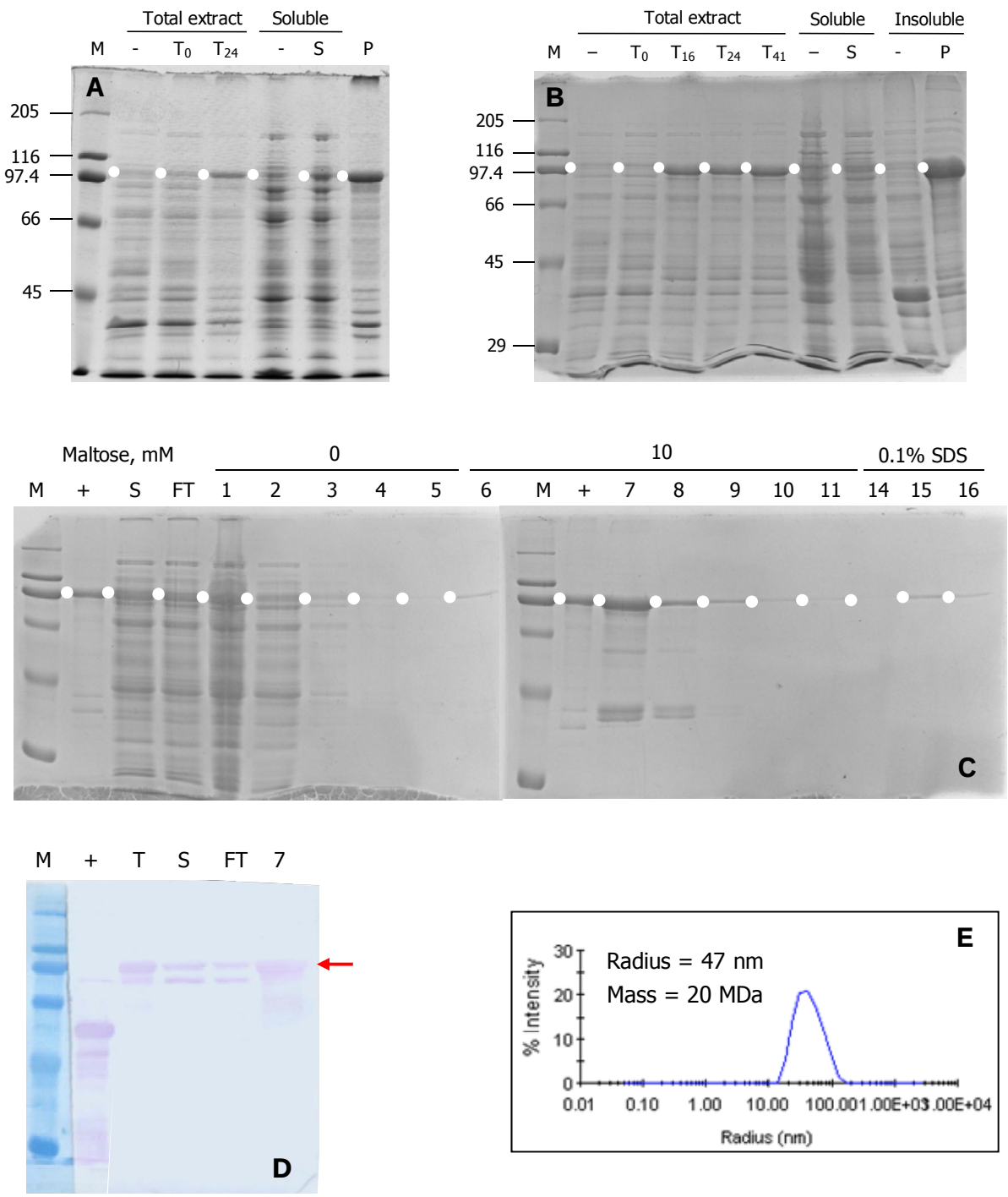

Figure 2.3.13: Expression and purification of MBP-DHCR24Δn. SDS-PAGE of total (T_0, T_{16}, T_{24}, T_{41}), soluble (S) and insoluble (P) extracts of *E. coli* Rosetta (DE3) cells transformed with pMAL-DHCR24Δ26 (panel A) and pMAL-DHCR24Δ41 (panel B). Cells were grown at 15°C after induction with 0.1 mM. Panel C: Purification of MBPΔ41 variant on a 1 ml amylose column equilibrated in CB buffer (see text). Proteins were eluted with 10 mM maltose. An additional wash with 0.2% SDS was carried out to elute the denatured proteins bound to the resin. Panel D: Western-blot with anti-Seladin C terminal antibodies of total extract, soluble extract, flow through (FT) and fraction 7 eluted with 10 mM maltose. Panel E: DLS signal of fraction 7 containing the MBPΔ41variant. M: markers; -: negative control; +: insoluble fraction of cells producing MBPΔ41 (positive control). White dots and red arrow indicate the expected position for the MBPΔ26 (99.4 kDa, panel A) and MBPΔ41 (97.8 kDa, panel B and C).

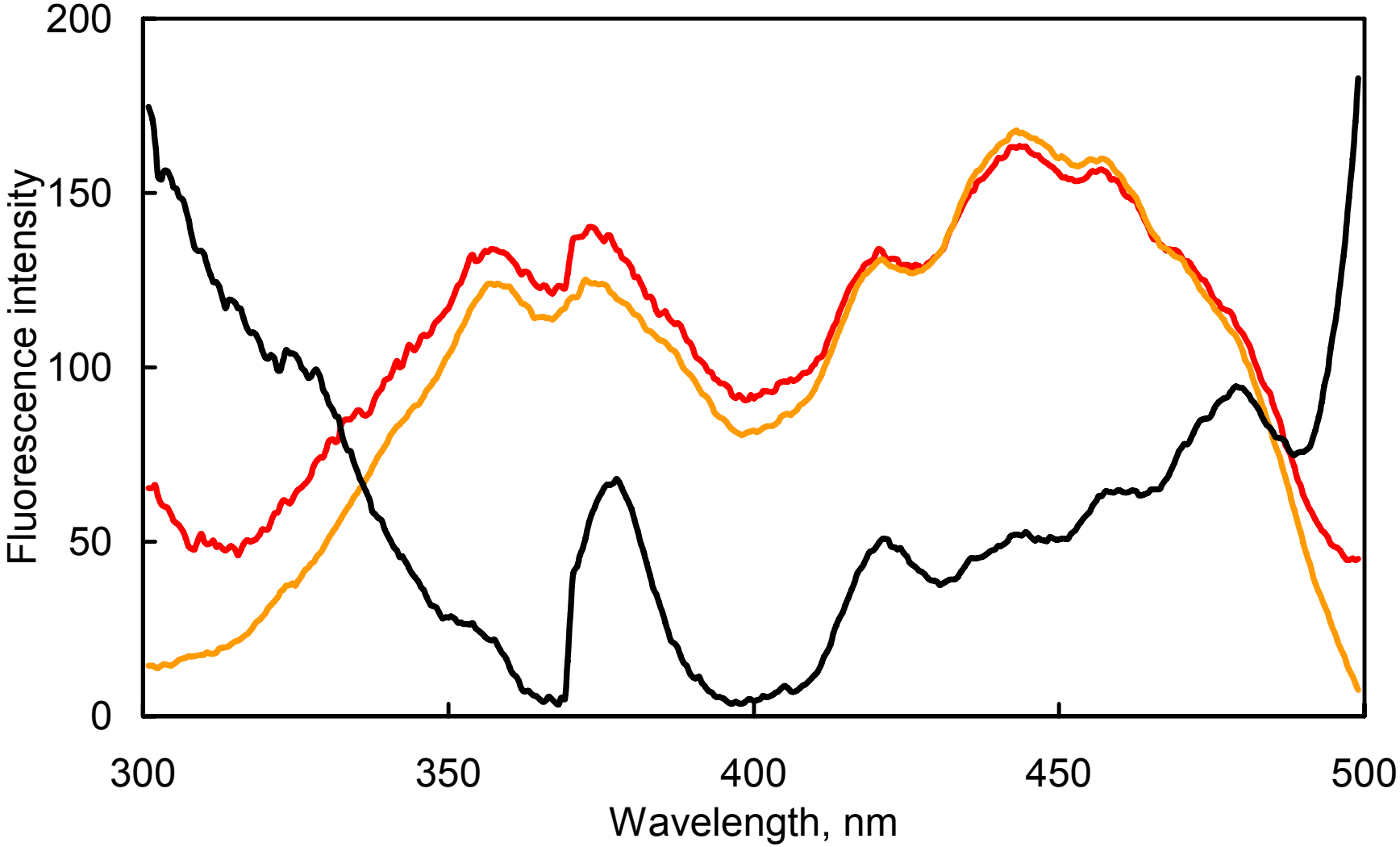

Figure 2.3.14: Purification of MBP-DHCR24Δn. Excitation spectra of fraction containing MBPDHCR24Δ33 (black), of the same fraction after denaturation at 100°C for 15 min (red) and of 1 μM FAD (orange). The comparison is only qualitative. λ_{em} = 520 nm.

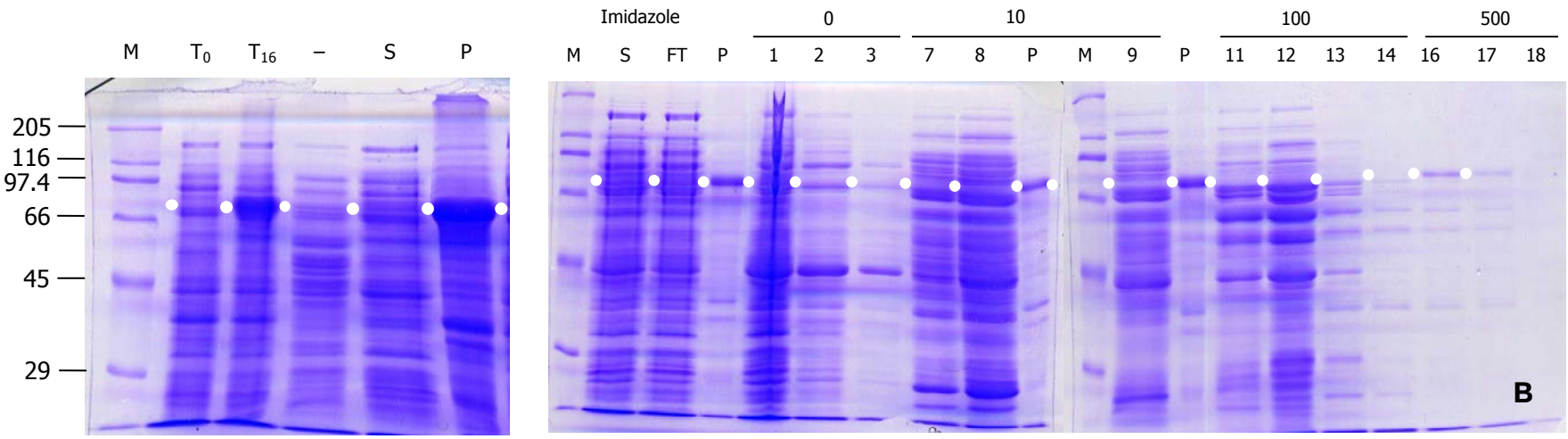

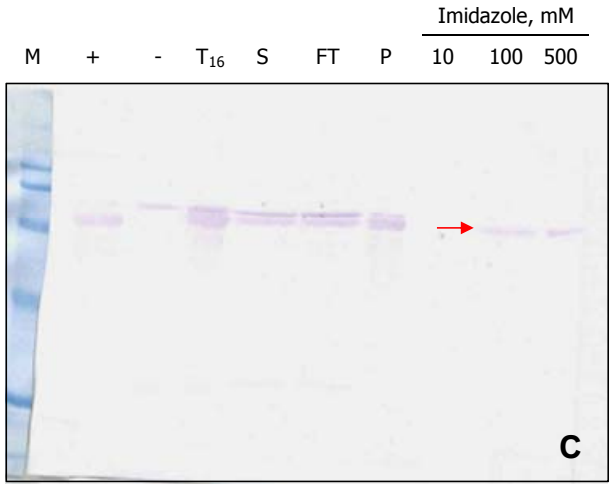

Figure 2.3.15: Expression and purification of His-SUMODHCR24Δ26 on Ni-NTA Sepharose. Panel A: Total (T_0 and T_{16}), soluble (S) and insoluble (P) extracts of *E. coli* Rosetta (DE3) cells containing pETSUMODHCR24Δ26 plasmid. After inductions with 0.1 mM IPTG (T_0), cells were grown at 15°C for 16 hours (T_{16}). -: crude extract of cells transformed with pETSUMO vector (negative control). Panel B: SDS-PAGE of fractions collected during the purification of His-SUMOΔ26 on Ni-NTA Sepharose. The resin was equilibred with buffer A and developed with a discontinuous gradient of imidazole (0, 10, 100, 500 mM). White dots indicate the expected position for His-SUMOΔ26. FT: flow-through. Panel C: Western-blot with anti-Seladin C-terminal antibodies. +: Insoluble fraction of cells producing His-SUMOΔ26 (positive control). The red arrow indicates the recognized His-SUMOΔ26 in fractions eluted with 100 and 500 mM.

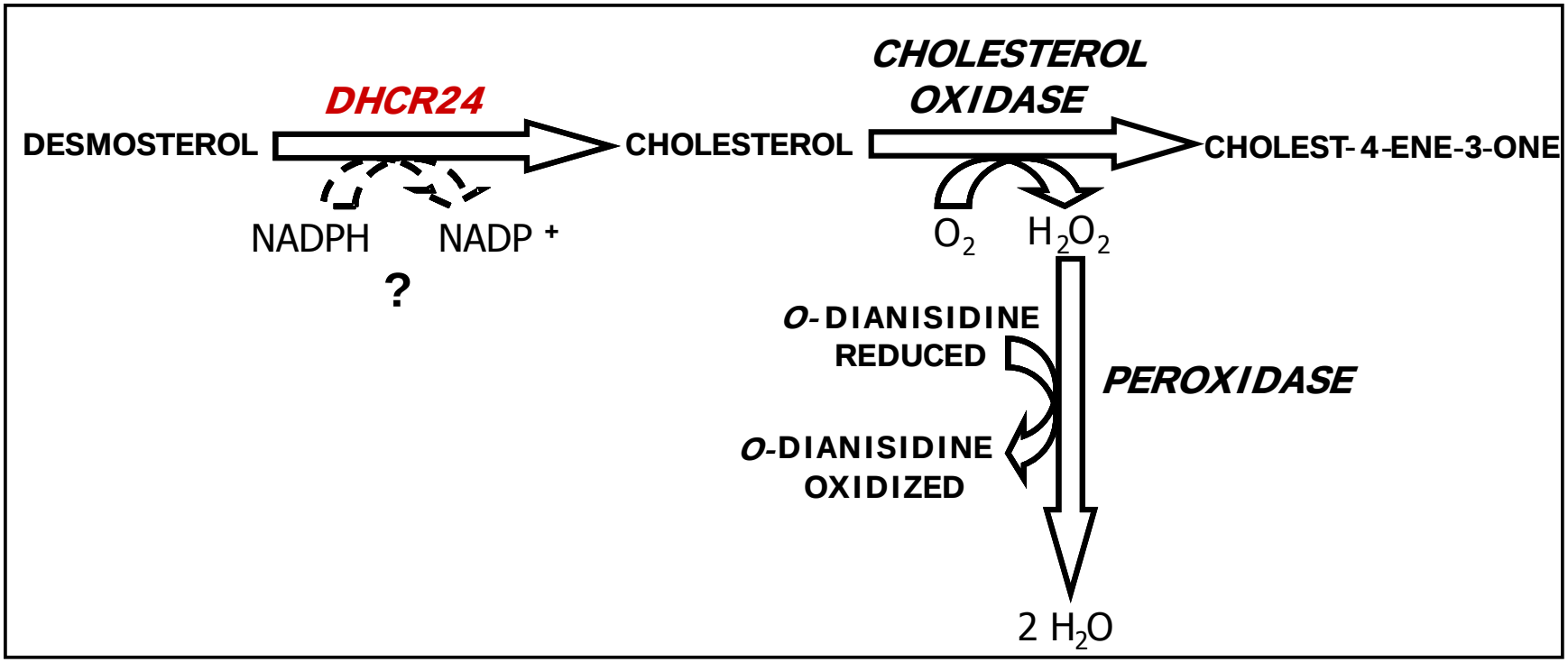

Figure 2.3.16: Set up of a coupled activity assay to monitor the DHCR24 catalyzed conversion of desmosterol into cholesterol. DHCR24 catalyzes the conversion of desmosterol in cholesterol. The latter is the substrate of cholesterol oxidase that converts the substrate in cholest-4-ene-3-one with the production of H_2O_2. The reaction of horse radish peroxidase allows to monitor the H_2O_2 production by measuring the oxidation of the chromogen o-dianisidine at 436 nm.

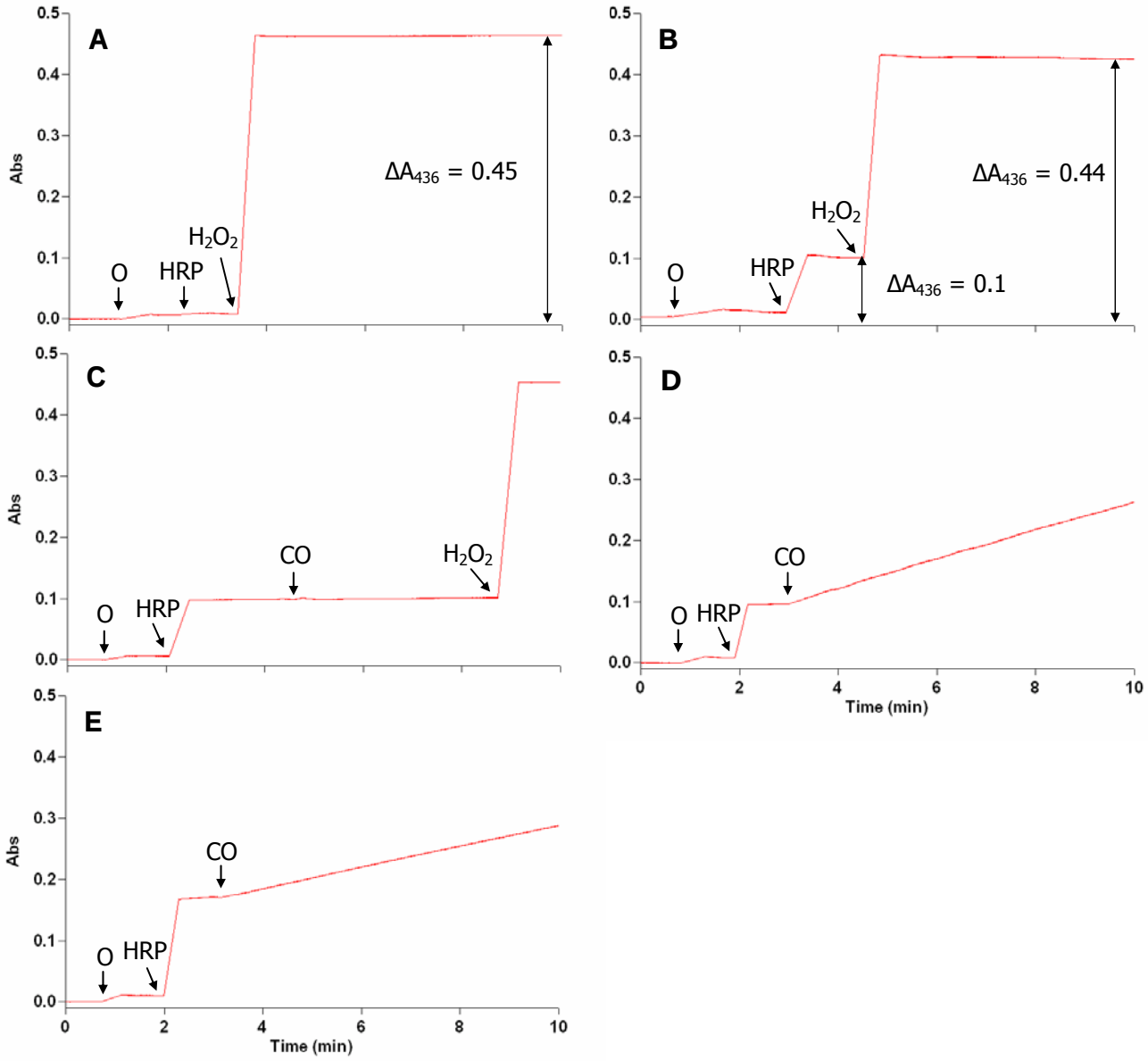

Figure 2.3.17: Set up of a coupled activity assay to monitor the DHCR24 catalyzed conversion of desmosterol into cholesterol. Assays were carried out in 100 mM Tris/HCl buffer, pH 7.5 at 25°C and the o-dianisidine (O) oxidation was monitored at 436 nm (ε = 11.6 $mM^{-1}cm^{-1}$). The o-dianisidine (O; 0.4 mM) oxidation catalyzed by horse radish peroxidase (1 mg/ml, 5 µl; HRP) was monitored in the presence of H_2O_2 (44 µM; Panel A). In these conditions o-dianisidine is rapidly and quantitatively oxidized, with a ΔA_{436} = 0.45 (40 µM). The addition of cholesterol (105 µM in 1.25% β-cyclodextrin) led to an initial variation of A_{436} of a value of 0.1 (Panel B) that was observed also after the addition of 1.25% β-cyclodextrin (not shown). The cholesterol oxidase (1 mg/ml, 5 µl ; CO) activity was monitored in the absence (Panel C) and presence (Panel D) of cholesterol (105 µM in 1.25% β-cyclodextrin) or desmosterol (105 µM in 1.25% β-cyclodextrin, Panel E).

3. HUMAN MICAL MONOOXYGENASE, A MULTIDOMAIN AXON GUIDANCE FLAVOPROTEIN

3.1 INTRODUCTION

MICAL (from the Macromolecule interacting with CasL) indicates a family of multidomain proteins conserved from insects to mammals, which plays an essential role in the control of cytoskeletal rearrangements that are at the basis of fundamental phenomena such as T cell maturation, axon growth, cell migration, cell-to-cell contacts, intracellular vesicle transport.

MICAL was initially identified in T cells as one of the interactors of CasL from which it derives its name. It was shown to be expressed in various other tissues, including thymus, lung, spleen and testis (Suzuki et al., 2002). At the same time, MICAL was also found in neuronal cells where it was shown to participate at the mechanisms that control axonal growth (Figure 3.1.1 panel A; Terman et al., 2002). During development of the nervous system, axonal growth cones are instructed to follow predetermined trajectories by heterogeneously distributed guidance molecules in their extracellular environment. Binding of axon guidance molecules to receptor complexes on the growth cone surface initiates intracellular signaling events, which in turn modulate growth cone morphology and directional mobility through local modifications of the neuronal cytoskeleton. Axon guidance molecules can act as attractants or repellents (Figure 3.1.1 panel B, Pasterkamp and Giger, 2009). In this process, semaphorines, a family of secreted or membrane-bound proteins, act as chemoattractive or chemorepulsive cues by binding to their receptors on the target cell. Semaphorin signaling during axon guidance is dependent on multimeric receptor complexes on the growth cone cell surface that contain plexin proteins as signal-transducing subunits. Upon semaphorin/plexin interaction, the cytosolic portion of plexin transduces the repulsive signal leading to inhibition of axon growth through local disassembly of the cytoskeleton structure. The details of the intracellular events that follow semaphorin/plexin interaction are not fully understood, but several participating proteins have been already identified, including members of the Rho family of small GTPases, collapsing response mediator proteins (CRMPs) and intracellular protein kinases (Figure 3.1.1 panel C).

Genetic and cell biology studies in Drosophila and various mammalian cell lines demonstrated that MICAL is an essential component of the intracellular response to the plexin-mediated semaphorin signaling (Terman et al., 2002). One MICAL form is found in Drosophila (D-MICAL) and three distinct MICAL genes are found in mammals (MICAL-1, MICAL-2 and MICAL-3), each with several isoforms that differ for the length of poorly conserved interdomain regions (Figure 3.1.2).

MICAL is formed by several conserved domains known to mediate protein-protein interaction: a calponin homology (CH) domain, a LIM domain, a prolin-rich region for Src homology 3 (SH3) domain recognition and a C-terminal region containing coiled-coiled motifs. The proline-rich region has been shown to mediate the interaction with the small GTPase Rab1 and with vimentin (Fischer et al., 2005; Suzuki et al., 2002). The C-terminal domain interacts with the cytosolic portion of PlexA (Terman et al., 2002). On the basis of sequence analyses, the N-terminal part of the protein (~ 500 residues) was proposed to be a flavoprotein of the monooxygenase or oxidase class, which was found to be essential for MICAL function in the cells (Figure 3.1.2 panel C; Terman et al., 2002). Therefore, it was proposed that MICAL functions in the semaphorin/plexin pathway through its flavoprotein domain by (i) producing reactive oxygen species in a NAD(P)H oxidase reaction or during oxidation of an unknown compound, or (ii) oxidizing or hydroxylating a small molecule that would act in the downstream signaling pathway, or (iii) oxidizing, hydroxylating or otherwise modifying a protein side chain resulting in the observed downstream effects (Figure 3.1.3).

The proposal that the MICAL N-terminal domain is related to monooxygenases was confirmed by structure determination of the mouse MICAL N-terminal region by two groups (Nadella et al., 2005; Siebold et al., 2005). The purified protein contained FAD, and it was demonstrated that this domain is structurally related to the class of FAD-dependent monooxygenases represented by p-hydroxybenzoate hydroxylase (PHBH) (Figure 3.1.5). The latter is the prototype of bacterial monooxygenases that act on aromatic compounds, which have been characterized in detail (see (Ballou et al., 2005; Entsch et al., 2005; Palfey and McDonald, 2010; van Berkel et al., 2006) for recent reviews and references therein). It was also shown that the mouse MICAL monooxygenase domain can oxidize NADPH with reduction of molecular oxygen to hydrogen peroxide (Nadella et al., 2005) with a high K_m for NADPH (222 μM) and a strikingly high turnover number (77 s^{-1}). The latter feature is at variance with monooxygenases of the PHBH class that exhibit a very low or even negligible NADPH oxidase activity in the absence of the substrate to be hydroxylated. In the presence of the substrate the rate of NADPH oxidation is enhanced up to 10^5 fold (as in PHBH) and the reactivity of the flavin-oxygen intermediate (initially, a 4a-hydroperoxy-FAD, Figure 3.1.4) is carefully controlled so that little or no hydrogen peroxide is released while one oxygen is transferred to the substrate undergoing hydroxylation and the other is released as part of a water molecule (Figure 3.1.4). This strict control of the reaction is achieved through conformational changes. Three stable conformations have been detected by combining site-directed mutagenesis, mechanistic and structural studies of PHBH and related enzymes. The striking difference among these conformations is the position of the FAD isoalloxazine ring that swings “in” and “out” of the active site during the catalytic cycle (Figure 3.1.5 panel D). Briefly, the “open” conformation allows

binding of the substrate to be hydroxylated; next the “flavin out” conformation allows FAD reduction by hydride transfer from NAD(P)H; the “flavin in” conformation brings the reduced flavin in a protected environment where formation of the 4a-(hydro)peroxy-FAD intermediate is favored at a position that promotes transfer of one oxygen atom to the substrate that becomes hydroxylated leaving a 4a-hydroxy-FAD intermediate (Figure 3.1.4). Release of one water molecule and regeneration of the oxidized flavin completes the catalytic cycle. “Flavin in” and “flavin out” conformations have been observed for mouse MICAL monooxygenase domain (MICAL-MO) (Siebold et al., 2005). At variance with PHBH, the “flavin out” conformation is the stable state of the protein in the “as isolated” (oxidized) form. The “flavin out” position is stabilized by several electrostatic interactions and by the formation of a charge-transfer interaction between the flavin isoalloxazine ring and the aromatic side chain of the conserved Trp 400 (Figure 3.1.5 panel C). In this conformation the FAD isoalloxazine ring is at the protein surface in proximity of residues that in PHBH have been shown to be implicated in the binding of the adenylate/pyrophosphate moieties of NADPH. Thus, for flavin reduction, Trp400 should move away to allow the nicotinamide ring of NADPH to form a productive complex with the flavin in order to reduce it by hydride transfer. Incubation of the crystals with NADPH caused flavin reduction and switch to a “flavin in” conformation. At variance with PHBH the conformational switch from the “out” to the “in” conformation involves significant relative repositioning of the monooxygenase and the FAD binding domains with formation of a channel that leads from the protein surface to the flavin isoalloxazine ring. The channel opening is on the same side of the protein as a patch of conserved positively charged residues in the N-terminal subdomain of MICAL-MO. These observations support the proposal that the MICAL-MO substrate may be the side chain of a protein residue that can access the reduced flavin through the channel. The patch of positive potential may favor docking of the protein substrate. According to this hypothesis, possible candidates as MICAL-MO substrates could be acidic cytoskeletal proteins. Among them actin is a strong candidate because covalent modification of actin is known to cause cytoskeletal rearrangements (Nadella et al., 2005; Siebold et al., 2005). In support of this hypothesis it has been recently shown that catalytic amounts of MICAL-MO in the presence of NADPH inhibit actin polymerization and accelerate its depolymerization (Hung et al, 2010). It has also been proposed that the collapsing response mediator protein (CRMP) may be the MICAL-MO substrate undergoing hydroxylation: addition of CRMP-1 to MICAL-MO quenches the NADPH-dependent hydrogen peroxide consumption measured in cell extracts (Schmidt et al., 2008). Alternatively, CRMP or other proteins (as well as the MICAL protein-interaction domains missing from MICAL-MO) may modulate the activity of the MICAL-MO domain by activating/quenching its NADPH oxidase activity or by presenting the

substrate undergoing hydroxylation (or oxidation) depending on the status of the cell (Nadella et al., 2005; Schmidt et al., 2008; Siebold et al., 2005).

Understanding the catalytic activity of the N-terminal monooxygenase-like domain of MICAL would significantly contribute to the understanding of the signaling pathways that lead to cytoskeletal rearrangements that are at the basis of fundamental processes, which underlie neuronal development, cell differentiation, communication and migration in health and disease (Pasterkamp and Giger, 2009; Zhou et al., 2008). Controlling axon growth through modulation of MICAL activity may be of therapeutic importance in the case of spinal chord injury (Beuchle et al., 2007; Pasterkamp et al., 1998; Pasterkamp et al., 1999; Pasterkamp and Kolodkin, 2003; Pasterkamp and Verhaagen, 2001, 2006), some forms of amyotrophic lateral sclerosis (Schmidt et al., 2009) and, perhaps, other neurodegenerative diseases. Modulation of MICAL activity may also be of relevance in some cancer forms. For example, it has been recently shown that some MICAL variants are associated with severe forms of prostate cancer, in particular with the tendency to metastatization (Ashida et al., 2006).

Surprisingly, the publication of mouse MICAL-MO structure in 2005 (Nadella et al., 2005; Siebold et al., 2005) was not followed up by *in vitro* studies of the mechanism of action of the isolated MICAL-MO domain and of protein forms including the other protein domains. To contribute to fill this void, the monooxygenase domain of human MICAL-1 has been produced in *E. coli* cells in our laboratory in three forms (untagged and with a N-terminal or C-terminal His-tag) and the kinetic and spectroscopic characterization of this novel flavoenzyme was carried out, to set the basis for further mechanistic studies and to help the design and interpretation of studies of MICAL in the cells.

3.2 METHODS

Construction of plasmids for the production of MICAL-MO

The region encoding residues 1-490 of human MICAL was amplified using Oligo-1 and Oligo 2.

Oligo 1 5'- CC*GAATTCC*AT**ATG**GCTTCACCTCCACCAACCCAGCGCATGCCC -3'

Oligo 2 5'- GT*GGATCC*TCTG**CTA**CTCGAGCTTGGCTAGCACATCATACAGGTCTCG-3'

Oligo-1 introduces a *EcoRI* site (*italic*) upstream of the translation start codon (bold) and a *NdeI* site (underlined). Oligo-2 introduces a *XhoI* restriction site (*italic*), a stop codon (bold) and a *Bam*HI restriction site (underlined). The amplified fragment was inserted in the pCRII-TOPO vector, and the obtained plasmid was used to transform *E. coli* Mach T1. Transformants were selected on LB plates supplemented with 50 μg/ml kanamicin (Kan). The resulting plasmid pTOPO-MICAL was sequenced and used for the subcloning of the region encoding MICAL monooxygenase domain (MICAL-MO) into pET23b vector. The *Nde-XhoI* fragment was cloned into pET23b digested with the same restriction enzymes and purified by agarose gel electrophoresis, to produce pETMICALHis encoding a C-terminally His-tagged version of MICAL-MO (MICAL-His; 496 residues; theoretical mass including the N-terminal Met residue: 55136; theoretical pI 9.05). The ligation products were transformed in *E. coli* DH5α cells and transformants were selected on LB plates containing ampicillin (Amp, 100 μg/ml).

Production of human MICAL monoxygenase domain in *E. coli* Rosetta (DE3) cells.

For the production of MICAL-His, pETMICALHis plasmid was transformed into *E. coli* Rosetta (DE3) cells. 10-20 colonies were used to inoculate 400 ml of LB medium supplemented with 25 μg/ml Clm and 100 μg/ml Amp. This preculture was grown to an optical density at 600 nm of approximately 1. Cells were harvested under sterile conditions, resuspended in fresh medium and used to inoculate 12-lt fermentor, to give an initial OD_{600} of 0.05. The culture was incubated at 25°C at 200 rpm until OD_{600} reached a value of approximately 1. The temperature was lowered to 15°C and 0.1 mM IPTG was added. Cell were harvested after 45 h.

Purification of MICAL-His.

E. coli cells (40 g) that had produced the MICAL-His form were resuspended in 50 mM sodium phosphate buffer, pH 7.5 100 mM NaCl, 1 mM EDTA, 5 mM β-mercaptoethanol (β-Me), 10% glycerol (Buffer F) and 1 mM PMSF (2 ml buffer/g cells). Homogenization was obtained by sonication (ten 30 s cycles with a Branson Sonifier with temperature controlled by immersion in a ice-salt bath) and homogenate is diluted to 5 ml buffer/g cells. The crude extract obtained after centrifugation of the homogenate at 18000 rpm (39086 g) for 1 h was directly loaded on a Ni-NTA Sepharose column (1 ml/g cells) equilibrated in buffer F. Unbound and weakly bound proteins were removed by flowing buffer F (1 column volume), buffer F containing 10 mM imidazole (5 column volumes) and buffer F containing 50 mM imidazole (5 column volumes). The column was developed by applying a 50-300 mM gradient of imidazole in buffer F (10 volumes). Fractions containing pure MICAL-His were pooled and concentrated by ultrafiltration in a Amicon concentrator equipped with a YM10 membrane. The sample was dialyzed overnight against buffer F, pH 7.2 or 20 mM Hepes/NaOH buffer, pH 7.0, 1 mM EDTA, 1 mM DTT, 10% glycerol (buffer G) or buffer G, 0.1 M NaCl. The protein solution was flesh frozen in liquid nitrogen and stored at -80°C.

NADPH oxidase activity assays

Standard NADPH oxidase activity: The initial velocity of NADPH oxidation (v) was monitored at 340 nm (ε_{340} = 6.23 mM^{-1} cm^{-1}) in 1 ml assays containing 100 μM NADPH in 20 mM Hepes/KOH, pH 7.0, at 25°C in Cary 100 (Varian) or Cary 219 (Varian) spectrophotometers. NADPH concentrations were varied between 10 and 300 μM to determine the steady-state kinetic parameters maximum velocity (V) and K_m for NADPH (K_{NADPH}) for the NADPH oxidase reaction, that was monitored at 340 nm for NADPH concentration up to 150 μM; for higher NADPH concentrations the reaction was monitored at 360 nm (ε_{360} = 4.32 mM^{-1} cm^{-1}).

Initial velocity data were expressed as apparent turnover numbers v/E, where v is the initial velocity of the reaction and E is the total enzyme concentration (s^{-1}) and turnover number (k_{cat}) have been calculated. The v/E values were fitted to the Michaelis-Menten equation (Eq 1) and double reciprocal plots (eq 2), or to the equation describing competitive (Eq. 3), non-competitive (Eq. 4) and uncompetitive inhibition (Eq. 5) using Grafit 4.0 software (Erythacus Software Ltd, UK).

Eq 1 $v/E = k_{cat}*S/(K_m + S)$

Eq 2 $E/v = (K_m/k_{cat})*1/S + 1/k_{cat}$

Eq 3 $v/E = k_{cat}*S/[K_m*(1+I/K_{is}) + S]$

Eq 4 $v/E = k_{cat}*S/[K_m*(1+I/K_{is}) + S*(1+I/K_{ii})]$

Eq 5 $v/E = k_{cat}*S/[K_m + S*(1+I/K_{ii})]$

In Eq 1-5, S is the varying substrate concentration and K_{is} and K_{ii} are the inhibition constants calculated from the effect of the inhibitor (I) on the slopes and intercepts of double reciprocal plots, respectively.

In some cases activities were measured in a HP8473 diode array (Agilent), recording spectra every 10 s for the first 2 min. Later the interval between subsequent spectra was increased by 20%.

Effect of viscosity on the NADPH oxidase reaction of MICAL-MO: The v/E values obtained by varying NADPH concentration in the presence of viscogens such as glycerol and sucrose were fitted to Eq. 6 (Eser and Fitzpatrick, 2010). The relative viscosity (η_{rel}) values for these two microviscogens have been obtained from the literature (Sheely, 1932; Caldwell, 1991).

Eq. 6 $v/E = k_{cat}*S/[K_m*(1+m*\mu) + S*(1+ n* \mu)]$

where $\mu = (\eta_{rel}^2-1)$; m and n are the effects of viscosity on k_{cat}/K_m and k_{cat}, respectively. The $m*\mu$ and $n*\mu$ values calculated at the different relative viscosity values correspond to $(k_{cat}/K_m)_0/(k_{cat}/K_m)_\eta$ and $(k_{cat})_0/(k_{cat})_\eta$ respectively, which indicate the ratio of the value of the parameter in the absence of viscogens and in its presence at a given concentration. The effect of PEG8000, a macroviscogen, was also studied (Caldwell, 1991).

Effect of ionic strength and of the type of ions on the NADPH oxidase reaction of MICAL-MO: The effect of ionic strength and type of ions on the enzyme activity was studied by measuring the initial velocity of assays done in the presence of varying concentrations of NADPH in the presence of different buffers (as indicated in the corresponding figures and tables). The effect of imidazole and bis-tris buffers on the slope of double reciprocal plots (K_{NADPH}/k_{cat}) as a function of the ionic strength was well fitted to the limiting case of the Debye-Hückel equation (discussed in Nørby et al., 1997; Eq. 7), which we modified for graphical purposes into Eq. 8.

Eq. 7 $\mathrm{Log}[(k_{cat}/K_{NADPH})/ (k_{cat}/K_{NADPH})_o] = z_e*z_{NADPH}*\sqrt{I}$

Eq. 8 $- \mathrm{Log}(k_{cat}/K_{NADPH}) = z_e*z_{NADPH}*\sqrt{I} - \mathrm{Log}(k_{cat}/K_{NADPH})_o$

Equilibrium titrations and anaerobic techniques

Prior to each experiment, aliquots of the enzyme (0.5 ml) were gel filtered through a Sephadex G25 prepacked column (PD-10, GE Healthcare) equilibrated in 20 mM Hepes/NaOH buffer, pH 7.0, 10% glycerol, 1 mM EDTA, 1 mM DTT. The enzyme (approximately 10 μM) was transferred to 1 ml quartz cuvette or to the cuvette of the vessel used for anaerobiosis (Williams, 1979). If needed, anaerobiosis was performed by applying several cycles of evacuation and equilibration with oxygen-free nitrogen (Williams, 1979).

Photoreduction of MICAL was done by adding 5 mM EDTA and 2 μM 5-deaza-5-carba riboflavin to the enzyme solution prior the anaerobiosis in the absence or presence of 30 μM $NADP^+$. The solution was then irradiated for different times with a standard slide projector lamp. After each irradiation period, spectra were recorded, until no further changes were observed.

A first pilot experiment of anaerobic reduction of MICAL-His with NADPH was done in the presence of $NADP^+$ (15 μM, equimolar to the enzyme) and 1 mM glucose 6-phosphate to the enzyme solution. Leuconostoc mesenteroides glucose 6-phospahte dehydrogenase (1 U, 10 μl) was then added to start the generation of NADPH. Titration with NADPH was carried out by adding up to 100 μl of 0.51 mM NADPH stock solution. After mixing, spectra were recorded at 17°C with the HP8473 diode array spectrophotometer. Spectra were corrected for dilution. For the analysis of the NADPH titration data, Eq. 9 was used. This equation takes into account that in the reaction the oxidized enzyme reacts with NADPH yielding reduced enzyme and $NADP^+$ with a 1:1 stoichiometry, so that the calculated equilibrium constant of the reaction (K_{eq}) allows the calculation of the standard free energy of the reaction ($\Delta G^{0'}$, Eq. 10) and of the mid-point potential of the bound FAD_{ox}/FAD_{red} couple (Eq. 11). A value of -0.32 V was used for the midpoint potential of the $NADP^+$/NADPH couple.

Eq 9 $$Y = [-K_{eq}*(E+S) \pm \sqrt{K_{eq}^2*(E+S)^2+4*(1-K_{eq})*(K_{eq}*E*S)}]/2*(1-K_{eq})$$

Eq 10 $$\Delta G^{0'} = .RT\ln K_{eq}$$

Eq 11 $$\Delta E^{0'} = -(\Delta G^{0'}/nF)$$

In Eq. 9 Y is the concentration of reduced enzyme, K_{eq} is the equilibrium constant of the enzyme reductive half reaction, S is the total NADPH concentration and E is the total enzyme concentration. In Eq. 10 R is the gas constant, T is the temperature. In Eq. 11 $\Delta E^{0'}$ is the difference between the

midpoint potential of the acceptor and that of the donor, n is the number of transferred electrons and F is the Faraday constant.

Stopped-flow studies of the reaction of MICAL-MO with NADPH

A Hi-Tech SF1 DX2 stopped-flow spectrophotometer was used to rapidly mix equal amounts (75 µl each) of the enzyme solution (approximately 10 µM in 20 mM Hepes/NaOH buffer, pH 7.0, 10 % glycerol, 1 mM DTT and 1 mM EDTA) and of the NADPH solution (0.1-0.88 mM) in the same buffer under anaerobiosis. Standard procedures for anaerobiosis, data collection and analysis were followed (Pennati et al, 2006).

Actin polymerization assays and NADPH oxidase reaction in the presence of G- and F-actin

Muscle actin and pyrene-modified muscle actin (Cytoskeleton, # cat AKL99 and AP05-A) were resuspended in cold distilled water to obtain a 10 mg/ml and 20 mg/ml solutions, respectively, in 5 mM Tris/HCl pH 8.0, 0.2 mM $CaCl_2$, 0.2 mM ATP, 5% (w/v) sucrose, 1% dextran. Aliquots of the solution were flash frozen in liquid nitrogen and stored at -80°C. Before each experiment, actin and pyren-actin were diluted with 5 mM Tris/HCl buffer, pH 8.0, 0.2 mM $CaCl_2$, 0.2 mM ATP, 1 mM DTT (dilution buffer) to a final concentration of 0.4 mg/ml (9.2 µM) and incubated on ice for 1 h to depolymerize actin oligomers. Actin was then centrifuged at 55000 rpm (100000 x g) for 1 h in a TL 100 ultracentrifuge, using a TLA 100.3 rotor. Polymerization of actin and pyren-actin was achieved by adding 1/10 volume of 50 mM Tris/HCl buffer, pH 7.5, 500 mM KCl, 20 mM $MgCl_2$, 5 mM DTT, 10 mM ATP (Polymerization buffer 10x) at 25°C.

Polymerization of pyrene muscle actin was monitored in a Cary Eclipse fluorescence spectrophotometer (Varian) (λ_{ex} = 365 nm, λ_{em} = 407 nm) in 120 µl assays, in the presence of 100 µM NADPH and 700 nM MICAL-His. Polymerization of muscle actin was monitored at the dynamic light scattering (DLS) apparatus (25°C, 2 acquisitions/min, 30-40 acquisitions).

The effect of G-actin and F-actin on the NADPH oxidase reaction of MICAL-MO was studied by measuring the initial velocity of 120 µl assays containing G-actin (0.83, 1.65 and 3.3 µM) or F-actin (0.6, 1.2 and 2.4 µM) at different NADPH concentrations (43, 100 and 210 µM). The effect of the dilution and polymerization buffers on the enzyme activity was also studied by measuring the initial velocity in 1 ml assays containing the dilution and polymerization buffers and varying NADPH concentration as reported for the standard NADPH oxidase activity.

3.3 RESULTS

MICAL-MO production and purification

E. coli Rosetta (DE3) cells transformed with pET23MICALHis plasmid were grown in LB supplemented with Clm and Amp to an OD_{600} of approximately 1 in a 12 l fermentor. The temperature was lowered to 15°C and 0.1 mM IPTG was added. An aliquot of cells was harvested after 15 h. The remaining culture was harvested after 45 h. As shown in figure 3.3.1 panel A, MICAL-His was produced in *E. coli* Rosetta strain cells; the level of soluble protein was low, but sufficient for its further purification. 30 g of cells that had produced MICAL-His were homogenized by sonication. The crude extract was directly loaded on a Ni-NTA Sepharose column (1 ml/g of cells) equilibrated in buffer F. Weakly bound proteins were removed flowing buffer F, buffer F containing 10 mM imidazole and buffer F containing 50 mM imidazole (as described in Methods). Bound proteins were eluted by applying a linear gradient of imidazole (Figure 3.3.1 panel B and C). MICALHis was purified to homogeneity (Figure 3.3.2), obtaining approximately 0.5 mg protein/g starting cell paste. Interestingly, the NADPH oxidase activity yield appeared to increase during the purification, a fact that could be ascribed to the sensitivity of the enzyme to the ionic strength and the composition of the medium (see below) (Table 3.3.1). The N-terminal sequencing of the purified protein revealed that the N-terminal Met had been posttranslationally removed and that the N-terminus was otherwise intact (498 residues; theoretical mass without the N-terminal Met residue: 55005; theoretical pI 9.05). The enzyme was stable for months in buffer F or G (regardless of the presence of NaCl) when flash frozen in liquid nitrogen and transferred to -80°C.

Determination of the stoichiometry and of the extinction coefficient of the bound FAD cofactor

The electronic absorbance spectrum of MICAL-His is indistinguishable from that of the untagged or N-terminally His-tagged forms. It is characterized by absorption maxima at 457 nm, 376 nm and 278 nm with a A_{457}/A_{278} ratio of 13 (Figure 3.3.3). A broad band of absorbance extending to 700 nm was observed in the spectrum, as reported also for the Drosophila protein (Terman et al, 2002). This broad absorbance band is most likely due to a charge-transfer interaction between the oxidized flavin and Trp400 observed in the crystal structure of the oxidized mouse MICAL-MO (Nadella et al., 2005; Siebold et al., 2005) where the flavin is in the “out” conformation and is coplanar with Trp400. Protein denaturation by addition of 0.2% SDS (Aliverti et al., 1999) converted the spectrum to that of free FAD (Figure 3.3.3). The flavin released from MICAL-His was confirmed to be FAD by fluorescence spectroscopy with the protein denatured by SDS or heat treatment. Denaturation

was found to bring along a 25 fold increase of fluorescence, which indicates that, as in the case of several other flavoenzymes, the flavin fluorescence is quenched by the protein environment (Table 3.3.3). Addition of phosphodiesterase (PDE) brought about a 10-fold increase in flavin fluorescence confirming the presence of bound FAD. By using the extinction coefficient of free FAD (ε_{452} 11.3 mM^{-1} cm^{-1}), the values of absorbance at 452 nm of the cofactor released by denaturation and the protein concentration, we calculated the MICAL-His contains 0.95 ± 0.12 mol FAD/mol protein (average of 7 determinations), indicating that 1 molecule of FAD is bound per molecule of enzyme. The extinction coefficient at 457 nm, which was calculated using the A_{452} of released FAD, is 8.1 ±0.2 mM^{-1} cm^{-1} (average of 7 determinations, Table 3.3.2)

The NADPH oxidase activity of MICAL-MO

The initial velocity of oxidation of NADPH was measured at 25°C in 20 mM Hepes/KOH buffer, pH 7.0, by monitoring the decrease of absorbance at 340 nm. The calculated kinetic parameters K_{NADPH} and k_{cat} were approximately 30 μM and 4 s^{-1} (Table 3.3.4). As found for the mouse enzyme (Nadella et al, 2005) NADPH is by far the best substrate of MICAL with a K_m value that is almost 20-fold lower than that measured for NADH and a 10-fold higher k_{cat} (Table 3.3.4). However, our results differ significantly from those reported by (Nadella et al., 2005) in that our K_m value for NADPH and k_{cat} are both approximately one order of magnitude lower than the corresponding values published for the mouse enzyme (K_m 222 μM; k_{cat} 77s^{-1}). The differences in the K_m value for NADPH could be reconciled by taking into account the fact that the (Nadella et al., 2005) assays were carried out in buffer containing 0.1 M NaCl. Indeed, inclusion of 0.1 M NaCl in our assays with the human protein led to a dramatic increase of the K_m value (500 μM) and a less marked decrease of k_{cat} (2.6 s^{-1}, Table 3.3.4). This observation led to a more thorough study of the dependence of MICAL-MO activity from the ionic strength and the type of ions.

Effect of ionic strength and anions on human MICAL-MO activity

Inclusion of NaCl (0.1 M) in the assays led to a 10-fold increase of the K_m value for NADPH with limited effect on k_{cat} (Table 3.3.4). In order to set the basis for further experiments on MICAL-MO, the effect of ionic strength and specific ions on its NADPH oxidase activity were studied. In all cases plots of reciprocal initial velocities as a function of the reciprocal NADPH concentrations at different fixed levels of salts added to the standard assay buffer (20 mM Hepes/KOH), pH 7.0) were linear. For each salt they yielded a set of lines converging on the Y-axis. The slopes of these plots exhibited a linear dependence on the ionic strength. The chloride salts yielded similar effects when the ionic strength was taken into account (Figure 3.3.4, panel A) indicating a specific effect of the

ion. No effects of calcium or magnesium ions were observed, indicating that a regulatory role of these ions is unlikely. Acetate salts had a milder effect than chloride salts, while MICAL was found to be very sensitive to phosphate. That chloride anions have a specific effect on MICAL-MO was confirmed by studying the activity of MICAL in the presence of different concentration of Tris and imidazole buffers that had been titrated to pH 7.0 with either acetic acid and HCl (Figure 3.3.4 panel B). The effect of ionic strength on the slope of double reciprocal plots obtained by varying chloride or acetate salts, Hepes, Tris, and phosphate were linear with respect to the ionic strength value (Figure 3.3.4 panel A and B). On the contrary, the effect of ionic strength on the slopes of the plots obtained with imidazolo/chloride, imidazolo/acetate and Bis-Tris/acetate could be fitted to Eq. 8, which derives from the original Debye-Hückel equation. The $-\mathrm{Log}(V/K_{NADPH})$ versus the square root of the ionic strength value ($\sqrt{I}$) was linear (Figure 3.3.4 panel C, Table 3.3.5). The intercept allows to calculate the ionic strength independent value of the parameter and the slope the product of the charges of the enzyme active site (z_e) and of the ligand (NADPH). Since NADPH, at pH 7.0, should carry 3-4 negative charges (Wijnands et al., 1984; Dawson et al, 1969), the enzyme active site should carry a charge of 0.1-0.13.

Reactivity of the FAD cofactor bound to MICAL-MO

Anaerobic photoreduction of the enzyme was carried out in the absence or presence of $NADP^+$. During the first part of the experiments, the conversion of the bound oxidized FAD to the 2-electron reduced FAD hydroquinone was observed (Figure 3.3.5 panel A and C). A very small increase of absorbance between 550 and 700 nm was observed during the early phases of the reduction, indicating the possible presence of some neutral flavin semiquinone. In the presence of $NADP^+$, further irradiation of the reduced enzyme led to the appearance of reduced NADPH (Figure 3.3.5 panel D), indicating that the reaction between MICAL and NADPH is largely favoured in the direction leading to the $E_{red}/NADP^+$ couple, but is not fully irreversible. Anaerobic reduction of MICAL-His with NADPH was done into two ways. In a pilot experiment, $NADP^+$ (15 μM) and 1 mM glucose-6-phosphate were added to the anaerobic solution of MICAL-His. Glucose-6-phosphate dehydrogenase (1 U, 10 μl) was added to start the generation of NADPH. The enzyme was rapidly converted to the reduced form with an isosbestic point at 348 nm. Later the isosbestic point was lost and NADPH accumulated (Figure 3.3.6). Anaerobic titration with NADPH (0.51 mM) led to the formation of the FAD hydroquinone without formation of intermediates (Figure 3.3.7). In this experiment the first 0.5 equivalents of NADPH failed to cause any absorbance changes. This observation can be attributed to a small amount of residual oxygen in the solution. Fitting the fractional absorbance changes during the titration after the first additions to Eq. 9 led to

calculating that 1 mol of NADPH is sufficient to reduce 1 mol of enzyme-bound FAD with a dissociation constant of 1.69 ± 0.3 μM. Since this value refers to the overall reaction leading from (NADPH + $MICAl_{ox}$) to ($NADP^+$ + $MICAL_{red}$), its reciprocal ($0.591*10^6$) corresponds to the equilibrium constant. From the E_m value of the NADP/NADPH couple of -0.32 V at pH 7.0, the E_m value of the bound FAD/FAD_{hq} couple could be calculated to be -0.150 V using Eq. 10 and 11.

Opening the anaerobic cuvettes to air at the end of each reductive titration led to different results. After photoreduction in the absence of $NADP^+$, the spectrum of the oxidized enzyme was recovered without detection on intermediate species (Figure 3.3.5 panel B). When the enzyme that had been photoreduced in the presence of $NADP^+$ was exposed to air, the oxidation of the NADPH still present was firstly observed (Figure 3.3.5). Later a species with a peak at 358 nm appeared (Figure 3.3.5 panel E). Further mixing with oxygen led to loss of this species and recovery of the spectrumof the oxidized enzyme (Figure 3.3.5 panel F). Exposure to air of the enzyme after NADPH titration led to direct oxidation of the enzyme without detection of intermediates.
The species responsible of the 358 nm peak may be an adduct between the bound FAD and molecular oxygen (Ghisla et al, 1977), which would be consistent with MICAL N-terminal flavoprotein domain being a monoxygenase rather than an oxidase. However, in monooxygenases the 4a-(hydro)peroxy-flavin intermediate is characterized by an absorbance maximum in the 370-380 range. Therefore the precise nature of this putative flavin-oxygen adduct, which is very sensitive to the properties of its environment (Ghisla et al, 1977), still needs to be determined.

Rapid reaction studies of the reaction between MICAL-MO and NADPH

MICAL-His (15 μM) was mixed anaerobically with 100-880 μM NADPH at 25°C in a stopped-flow spectrophotometer equipped with a diode-array detector. Absorbance changes were consistent with conversion of the oxidized enzyme to the 2-electron fully reduced species with no detectable intermediates (Figure 3.3.8 panel B). This observation was confirmed by the analyses of the kinetics of decrease of absorbance at several wavelengths that indicated that the reaction could be described by a simple monoexponential process at all wavelengths (Figure 3.3.8 panel A). Under the experimental conditions, by making the approach to equilibrium assumption, the K_d value for the enzyme-NADPH complex can be calculated from the dependence of the observed reduction rate from NADPH concentration. The calculated $K_M(K_d)$ for NADPH was 56 ± 7.3 μM and the k_{red} was 3 ± 0.1 s^{-1} (Figure 3.3.8 panel A inset). The $K_M(K_d)$ was higher and the k_{red} lower than the K_{NADPH} and k_{cat} measured under steady-state conditions (Table 3.3.4). Since a requirement for catalytic competence of any reaction intermediate is that its rates of formation or decay must be both equal or greater than turnover, the observation of a k_{red} smaller than k_{cat} was puzzling. This discrepancy was

easily solved by measuring the steady-state K_{NADPH} and k_{cat} in the same buffer as that used for the stopped-flow experiments. In these experiments the buffer contained 10% glycerol to stabilize the enzyme. The K_{NADPH} and k_{cat} values measured in the presence of 10% glycerol matched well the $K_m(K_d)$ and k_{red} values obtained in the stopped-flow experiment (Table 3.3.4) indicating that enzyme reduction by NADPH is determining the rate of enzyme turnover under our experimental conditions. This conclusion was supported by a preliminary experiment in which we reacted MICAL with NADPH (20 μM) in the presence of atmospheric oxygen and varying concentrations of $NADP^+$ (0, 20 μM and 200 μM). In this experiment NADPH oxidation was observed, but the enzyme-bound flavin remained in the oxidized state. Interestingly, in the study of MICAL reaction with NADPH we identified no intermediates regardless of the presence of oxygen or $NADP^+$. The similar values of the steady-state K_m for NADPH and the K_d for the enzyme-NADPH complex determined from the stopped-flow experiment further supported the validity of the approach to equilibrium assumption, i.e.: that the chemical step (hydride transfer from NADPH to the enzyme bound flavin) is much slower than both the rate of formation of the Michaelis complex and of that of its dissociation.

The observation of an effect of glycerol on MICAL reaction led to the study of the viscosity effects on the reaction.

Effect of viscosity on the reaction of MICAL-MO

The effect of glycerol and sucrose (microviscogens) and of PEG8000 (a macroviscogen) on the K_{NADPH} and k_{cat} of the NADPH oxidase reaction of MICALHis was studied in 20 mM Hepes/NaOH, pH 7.0 (Figure 3.3.9 panel C and Table 3.3.6) under steady-state conditions. The k_{cat} and k_{cat}/K_{NADPH} values were little sensitive to PEG8000 so that the study of the effect of this macroviscogen was abandoned. On the contrary, both k_{cat} and k_{cat}/K_{NADPH} were lowered by glycerol (Figure 3.3.9 panel A) and sucrose (Figure 3.3.9 panel B). Interestingly, the data could not be fitted to the equation describing a noncompetitive inhibition pattern (Eq. 4). Rather, they were well fitted with Eq 6, which relates the effect of viscosity on k_{cat} and k_{cat}/K_{NADPH} as a function of the relative viscosity of the solvent (Table 3.3.7, (Eser and Fitzpatrick, 2010)). Therefore, it appears that glycerol and sucrose act by increasing the solvent viscosity rather than by mimicking MICAL substrates or products. In the absence of an effect of a macroviscogen such as PEG8000, the effects of increasing solvent viscosity with microviscogens can provide information on diffusion limited steps and even enzyme conformational changes during the catalytic cycle. The observed effects of glycerol and sucrose on k_{cat} and k_{cat}/K_{NADPH} were very similar to each other so that the data could be even fitted to the same line (Figure 3.3.9 panel D). Plots of the relative k_{cat} (i.e.: k_{cat} measured in the

absence of glycerol over the k_{cat} measured in the presence of a given relative viscosity value) as a function of the relative viscosity brought about by increasing glycerol or sucrose were linear and with a slope close to 1 (Figure 3.3.9 panel D). Plots of the relative k_{cat}/K_{NADPH} as a function of the relative viscosity brought about by glycerol or sucrose were also linear but the slope was 3.0 ± 0.1 (for glycerol) and 4.2 ± 0.3 (for sucrose) (Figure 3.3.9 panel D, Table 3.3.8). A slope of 1 is expected when k_{cat} is limited by diffusion of one of the enzyme substrates or products to/from the enzyme active site (Blacklow et al., 1988; Brouwer and Kirsch, 1982; Caldwell et al., 1991; Eser and Fitzpatrick, 2010). This result is in contrast with the observation that the hydride transfer step is fully determining k_{cat}. In such a case a solvent viscosity effect would be expected. However, the observed effect may be interpreted as due to the presence of a conformational change that takes place during the catalytic cycle (Blacklow et al., 1988; Brouwer and Kirsch, 1982; Caldwell et al., 1991). An absolute value of the viscosity effect greater than unity on V/K has been interpreted as due to a viscosity effect on a protein conformational change that takes place on binding of the varied substrate to the enzyme (Blacklow et al., 1988; Brouwer and Kirsch, 1982; Caldwell et al., 1991; Eser and Fitzpatrick, 2010). Effects on k_{cat} and k_{cat}/K_{NADPH} would monitor steps contributing to the overall turnover rate and those taking place from NADPH binding up to (and including) the first irreversible step. In MICAL, the effects of viscosity may be monitoring the conformational changes that have already been proposed to take place in MICAL on the basis of its structure (Nadella et al., 2005; Siebold et al., 2005), namely the movement of Trp400 to allow hydride transfer form the NADPH nicotinamide ring to the flavin or the subsequent flavin out/flavin in transition. A third conformational change may be proposed to take place on the basis of the known properties of PHBH. In this enzyme NADPH may bind to the enzyme regardless of its conformation or oxidation state. However, initial NADPH binding has been proposed to occur in a non productive mode. Prior to hydride transfer two events must take place: i) the flavin should move to the "out" conformation and (ii) the NADPH nicotinamide ring should reposition to obtain the correct geometry for direct hydride transfer from its C(4) position to the flavin N(5) atom. The latter event must be accompanied by a local conformational change a of loop (Cole et al, 2005). As a working hypothesis, it is attractive to propose that the viscosity effect on k_{cat}/K_{NADPH} may mainly monitor the conformational changes that bring NADPH in a position suitable for hydride transfer (that postulated to accompany repositioning of the nicotinamide ring and the observed movement of Trp400), while the effect on k_{cat} may be monitoring the "flavin out"/"flavin in" transition after hydride transfer.

Actin as substrate of MICAL-MO

The MICAL-MO effect on actin polymerization was studied *in vitro*. G-pyrene actin was prepared as described in Methods. After addition of the polymerization buffer, the fluorescence intensity increased 20-fold and the polymerization was complete after 15 min (Figure 3.3.10 panel A). Interestingly, the addition of MICAL-His (45 μM, 2 μl) and of NADPH (100 μM final concentration) before polymerization led to different results depending on the sequence of addition. When MICAL-His was added first, the fluorescence signal increased of ~ 5-fold, but decreased to the initial level when NADPH was added. At this point, polymerization was started with an initial velocity similar to that of the control sample (Figure 3.3.10 panel A). However, the final intensity increase was only 15-fold. When NADPH was added before MICAL-His, no increase in the signal was observed. In this case the polymerization started more slowly and the signal increase was only 10-fold (Figure 3.3.10 panel A). NADPH oxidase activity assays were carried out in the dilution and polymerization buffers in the presence of 100 μM NADPH and MICAL (45 μM, 2 μl) in order to measure the time-course of the NADPH oxidation reaction under the conditions used for fluorescence experiments. As shown in Figure 3.3.10 panel D, NADPH is completely oxidized by MICAL within 5 min in the presence of dilution buffer, whereas it took ~15 min to observe complete oxidation of NADPH in the presence of the polymerization buffer. Thus, this result suggest that the differences observed in the polymerization of actin in the presence of MICAL depending on the order of enzyme and NADPH additions (Figure 3.3.10 panel A) may be related to the actual presence of NADPH during the polymerization reaction. In fact, when MICAL was added before NADPH (Figure 3.3.10 trace (b)), NADPH was completely consumed before the polymerization started and no effects on the velocity of polymerization was observed. On the contrary, when MICAL was added after NADPH (Figure 3.3.10 trace (c)), NADPH was still present when the polymerization started (after ~ 2 min), suggesting that the NADPH oxidation activity of MICAL actually affects the polymerization rate. This results confirms the hypothesis that MICAL-MO inhibits polymerization through its NADPH oxidase activity(Hung et al, 2010).

The effect of MICAL-MO on the depolymerization of actin was also examined. When MICAL and NADPH were added to F actin (produced from pyrene-labelled G-actin), a very fast decrease in the fluorescence signal was observed (Figure 3.3.10 panel B). The same results were obtained in assays where NADPH or MICAL was added before polymerization and the second component was added after F actin was formed (Figure 3.3.10 panel B). In order to verify the possible effects of NADPH and MICAL on the fluorescence signal, polymerization assays in the absence of actin were done. When NADPH was added to the dilution buffer, the fluorescence intensity increased to a value of 6, as expected by taking into account the emission spectrum of NADPH (λ_{ex} 340 nm, figure 3.3.12),

and it decreased in the presence of MICAL. The calculated rate of NADPH consumption in the actin buffer (1.1 s^{-1}) and in actin polymerization buffer (0.33 s^{-1}, Figure 3.3.10) were both significantly lower than that observed for the depolymerization of actin (Figure 3.3.10), These observations confirm that MICAL stimulated actin depolymerisation (Hung et al, 2010) in the presence of NADPH and suggest that F actin stimulates NADPH oxidation by MICAL. Polymerization of muscle actin was also monitored by dynamic light scattering at 25°C. The signal obtained from a G-actin solution (5.7 μM) revealed the presence of a species with a calculated mass of 44 kDa (i.e.: the expected mass for the monomeric actin) (Figure 3.3.11 panel B). The addition of polymerization buffer led to a time-dependent increase of the average particle radius that was completed in 15 min, a time interval similar to that required to fully convert G actin into F actin as monitored fluorimetrically At the end of the reaction the mean radius reached a value of 130 nm (Figure 3.3.11 panel A). As expected from the previous fluorimentric assays, the radius did not vary when NADPH was added, but, surprisingly, it further increased after addition of MICALHis (Figure 3.3.11). This result indicates that the fluorescence decrease with previously observed is not due to actin depolymerization as initially proposed (Hung et al, 2010). Rather, it seems to suggest that MICAL modifies actin causing formation of aggregates. When pyrene-acin is used , the formation of these aggregates may lead to the observed fluorescence quenching In order to confirm and extend the hypothesis that actin may actually be a substrate of MICAL, the initial velocity of oxidation of NADPH was measured at 25°C in the presence of G-actin (0.83, 1.65 and 3.3 μM) and F-actin (0.6, 1.2 and 2.4 μM), or in the presence of the corresponding buffer. The rate of NADPH oxidation in the presence of the dilution buffer is similar to that observed in the 20 mM Hepes/KOH buffer, pH 7.0 (k_{cat} 3.4 s^{-1}), but K_{NADPH} is significantly higher (~100 μM, Table 3.3.9). The effect is more drastic with polymerization buffer, as expected for the higher ionic strength. When G-actin is present in the assay, the rate of NADPH oxidation is only a 30 % higher than the rate measured in the corresponding buffer (k_{cat} 4.5 s^{-1}). On the contrary, the presence of F-actin increased the rate of NADPH oxidation (k_{cat} 12.3 s^{-1}) with respect to the corresponding buffer (Figure 3.3.13; Table 3.3.9). This preliminary, but highly reproducible result suggests that actin is a MICAL-MO substrate. At the time of writing, the identification of actin side chain that may be modified by MICAL-MO and the nature of such covalent modification is in progress.

3.4 CONCLUSIONS

Homogeneous forms of the flavoprotein domain of the human MICAL have been produced in *E. coli* with most of the experiments carried out with the most abundant form, which carries a C-terminal His-tag. This form was indistinguishable from the untagged and the N-terminal His-tagged forms for the flavin content, the absorbance properties and the steady-state kinetic parameters k_{cat} and K_m for NADPH. NADPH oxidation catalyzed by MICAL-MO leads to stoichiometric production of H_2O_2, defining the NADPH oxidase reaction of MICAL-MO. Steady-state parameters k_{cat} and K_m for this reaction were approximately 4 s^{-1} and 30 μM in 20 mM Hepes/KOH buffer, pH 7.0. This activity is one order of magnitude lower than that reported for the mouse protein form (Nadella et al, 2005), but still significantly higher than that observed with several monooxygenases of the PHBH class in the absence of the substrate to be hydroxylated. In previous experiments we attributed the high rate of the NADPH oxidase activity of the mouse MICAL-MO to artifacts due to the assay method. The NADPH oxidase reaction of MICAL-MO is limited by the rate of enzyme reduction by NADPH at atmospheric oxygen concentrations as shown by rapid reaction experiments of the isolated reductive half reaction. The similarity of the K_m for NADPH measured under steady-state conditions and the corresponding value measured in the stopped-flow during the study of the reductive half reaction, suggest that for MICAL-MO the K_m for NADPH actually corresponds to the dissociation constant of the enzyme-NADPH complex.

MICAL-MO showed functional similarities with the class of monooxygenases represented by PHBH. It was found to be very sensitive to the ionic strength of the medium and to the nature of the anions present in solution. As reported for PHBH, (Entsch et al, 2005; Palfey and McDonald, 2010; Wijnands et al, 1984) the ionic strength effect on MICAL-MO activity is related to the strong sensitivity to electrostatics. The NADPH oxidase activity of MICAL-MO is also sensitive to the viscosity of the medium. Glycerol and sucrose (microviscogens), but not PEG8000 (a macroviscogen) have an effect on both k_{cat} and k_{cat}/K_{NADPH} values. The dependence of k_{cat} on the relative viscosity brought about by glycerol and sucrose are linear and with slopes close to unity. Since kred is fully limiting turnover, the viscosity effecton k_{cat} may be monitoring one or more of the conformational changes that take place during the NADPH oxidase reaction of MICAL-MO.. The viscosity dependence of k_{cat}/K_{NADPH} is much greater than unity indicating that a conformational change may take place following binding of NADPH to the enzyme (Blacklow et al., 1988; Brouwer and Kirsch, 1982; Caldwell et al., 1991; Eser and Fitzpatrick, 2010). The viscosity effects maybe monitoring one or more of the proposed conformational changes that accompany the enzyme reaction as discussed in the “results” paragraph..

In spite of the effect of glycerol on the enzyme kinetic properties, glycerol (10%) had to be included in the titration and rapid reaction kinetics experiments to ensure enzyme stability over several hours. Under our experimental conditions, no charge-transfer complexes were observed during photoreduction in the absence/presence of $NADP^+$ or during the titration with NADPH. Furthermore, no intermediates were detected for the reaction between MICAL-MO and NADPH monitored at the stopped-flow. In MICAL-MO it has been proposed (Siebold et al., 2005) that Trp400, which stabilizes the flavin out conformation forming a charge transfer interaction with the FAD isoalloxazine ring in the crystal structure of mouse MICAL-MO and in solution, must move away to allow for the correct positioning of the NADPH nicotinamide ring prior to hydride transfer. Failure to observe charge-transfer complexes with pyridine nucleotides during the reductive titrations and the rapid reaction study would indicate that movement of Trp400 may be slow relative to productive positioning of the NADPH nicotinamide ring and hydride transfer, at least under the present experimental conditions. On the other hand, failure to observe charge-transfer complexes between reduced MICAL-MO and $NADP^+$, either during titrations or rapid reaction studies, may simply reflect a weak binding of $NADP^+$ to the reduced enzyme.

Exposure to air of the enzyme that had been photoreduced in the presence of $NADP^+$ led to the transient observation of a complex spectrum with a novel feature at 358 nm. The spectrum may indicate the presence of a covalent intermediate between the flavin and molecular oxygen during turnover with oxygen. With FAD-dependent monooxygenases, 4a(hydro)peroxyFAD and 4a-hydroxyFAD have been sometimes detected during the catalytic cycle. Their stability and the details of their absorbance properties depend to a large extent upon the enzyme identity and the experimental conditions, as discussed in (Ghisla et al., 1977). Conditions to stabilize the intermediate(s) of MICAL-MO still need to be found. In this process the sensitivity of the enzyme to ionic strength, the type of salts and the viscosity of the medium will have to be taken into account.

One of the key issue of MICAL is the actual catalytic activity. It has been proposed that MICAL flavoprotein domain acts as a NADPH oxidase producing reactive oxygen species (H_2O_2) and that its activity may be modulated by the downstream domains and by their interaction with other proteins (Kolk and Pasterkamp, 2007; Schmidt et al., 2008; Terman et al., 2002; Ventura and Pelicci, 2002; Zhou et al., 2008). high NADPH oxidase activity of the MICAL monoxygenase domain reported for the mouse enzyme (77 s^{-1}) may have been overestimated (Nadella et al., 2005), but the 20-fold lower values we measured with the human protein still makes MICAL flavoprotein domain a relatively good oxidase. However, the catalytic efficiency is dramatically lowered by increasing ionic strength and anions so that *in vivo*, and in the absence of the protein additional

domains, interacting proteins or the physiological substrate, the basal oxidase activity may be very low due to a high K_m for NADPH. In this respect the sensitivity of MICAL NADPH oxidase activity to electrostatics may indeed provide a means to finely tune its oxidase activity in the absence of the physiological substrate undergoing hydroxylation (or otherwise covalent modification). Alternatively, it has been proposed that MICAL-MO oxidizes or hydroxylates a small molecule or the side chain of an interacting protein. Among the candidate protein substrates of MICAL are CRMP-1 (Schmidt et al., 2008) and actin (Kolk and Pasterkamp, 2007; Nadella et al., 2005; Siebold et al., 2005). In the latter case MICAL-MO has been recently shown to be sufficient to inhibit actin polymerization and to promote actin depolymerization (Hung et al, 2010). Here, we confirmed and extended this hypothesis, demonstrating that MICAL-MO affects actin polymerization through its NADPH oxidase activity. Furthermore, k_{cat} for the NADPH oxidation in the presence of F-actin was 4-fold higher (12.3 $s^{-}1$) than that measured under standard conditions and 10-fold higher than that observed in the corresponding polymerization buffer, indicating that actin may be a substrate of MICAL-MO.

All these experiments set a solid basis for the further characterization of MICAL properties in relation to its biological activity and for the interpretation of results obtained through cell biology and genetic approaches.

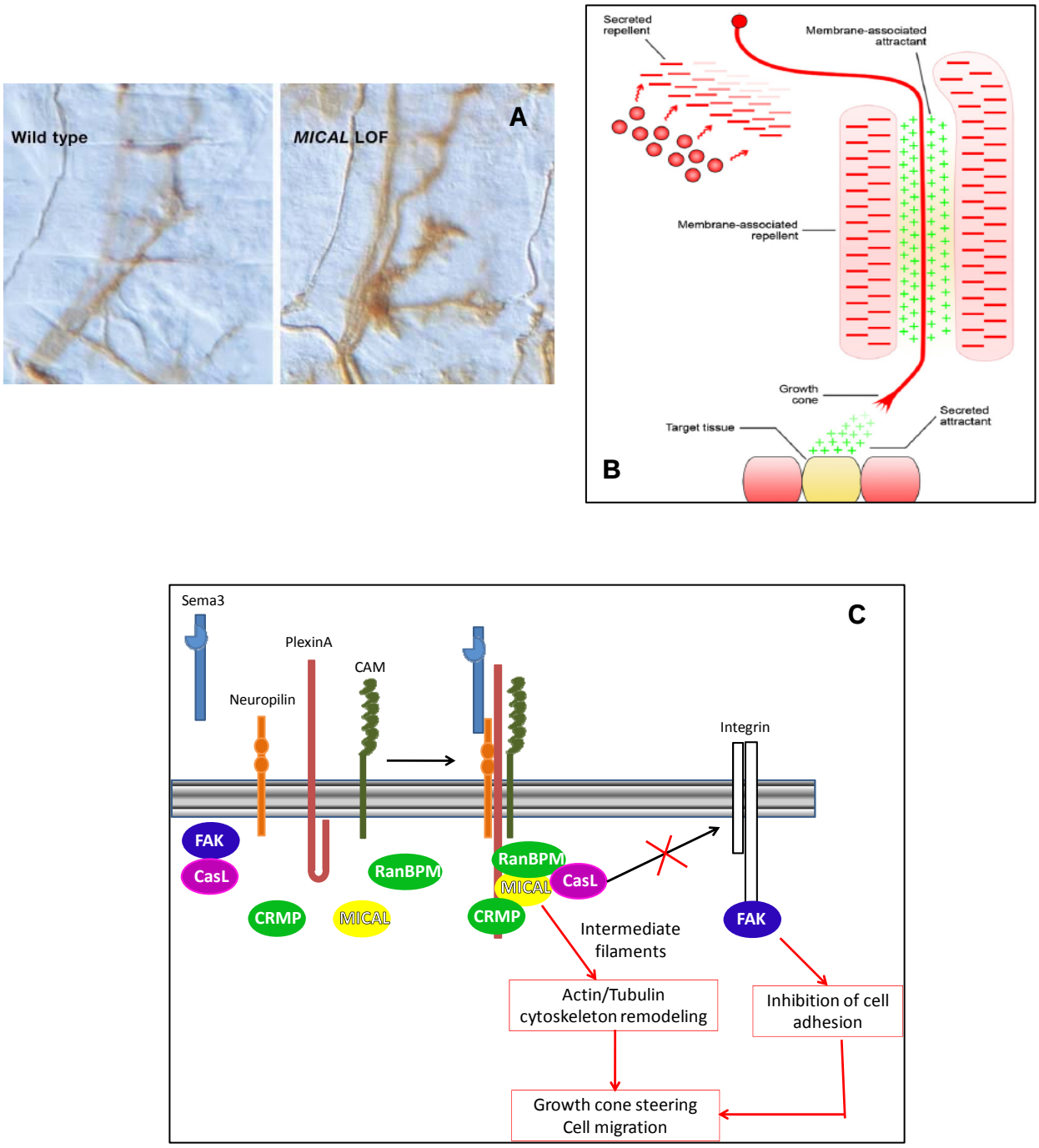

Figure 3.1.1 MICAL participates at the mechanisms that control axon growth. Panel A: Effect of MICAL deletion on Drosophila axon growth (Terman et al, 2002). LOF: loss of function. Panel B: Axon growth is guided by molecules that act as attractants or repellents. Panel C: Potential role of MICAL in Sema3/PlexA signalling. CRMP, collapsin response mediator protein ; RanBMP, Ran-small GTPase binding protein (RanBPM);FAK, focal adhesion kinase. CasL may be sequestered by MICAL preventing the formation of the integrin signaling complexes, thus inhibiting cell adhesion. MICAL is also known to bind vimentin (the main component of intermediate filaments) and their expression patterns are similar in nonneuronal cells. MICAL also binds rab1, a small GTPase involved in the secretory pathway and targeting vesicles to their target destination through interaction with the microtubule and/or actin cytoskeleton.

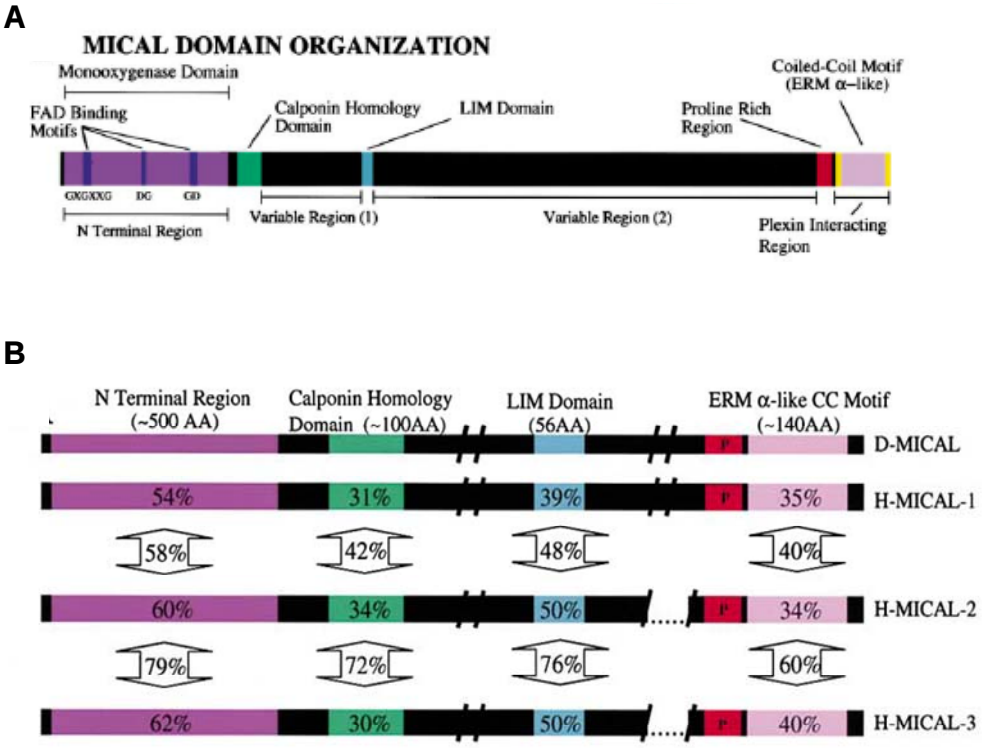

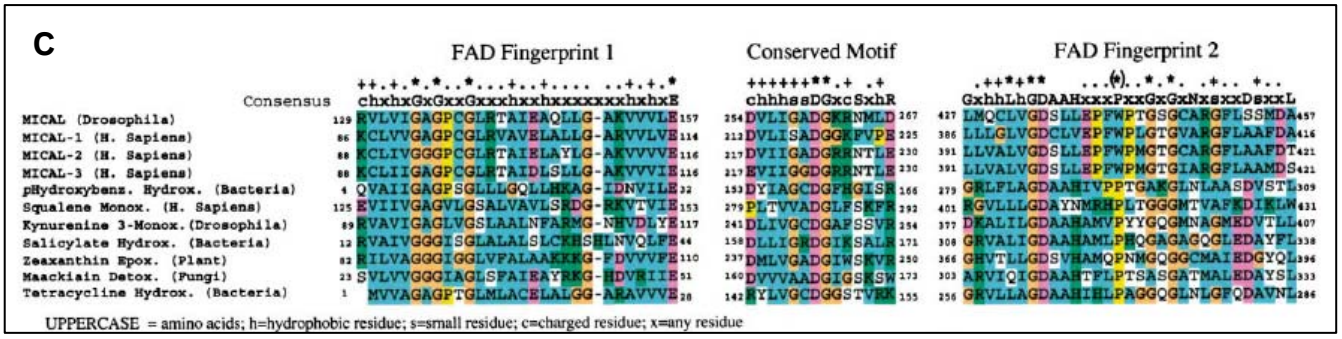

Figure 3.1.2: Molecular characterization of MICAL. Panel A: MICAL domain organization. Panel B: Conserved regions of MICAL in Drosophila (D-MICAL) and in vertebrates (H-MICAL). Black regions indicate sequences that are not well conserved among family members. Percents within domains indicate the homology identities in the corresponding regions. Panel C: Alignment of conserved sequences of the MICAL monooxygenase domain with members of the flavoproteine monooxygenase family (Terman et al, 2002).

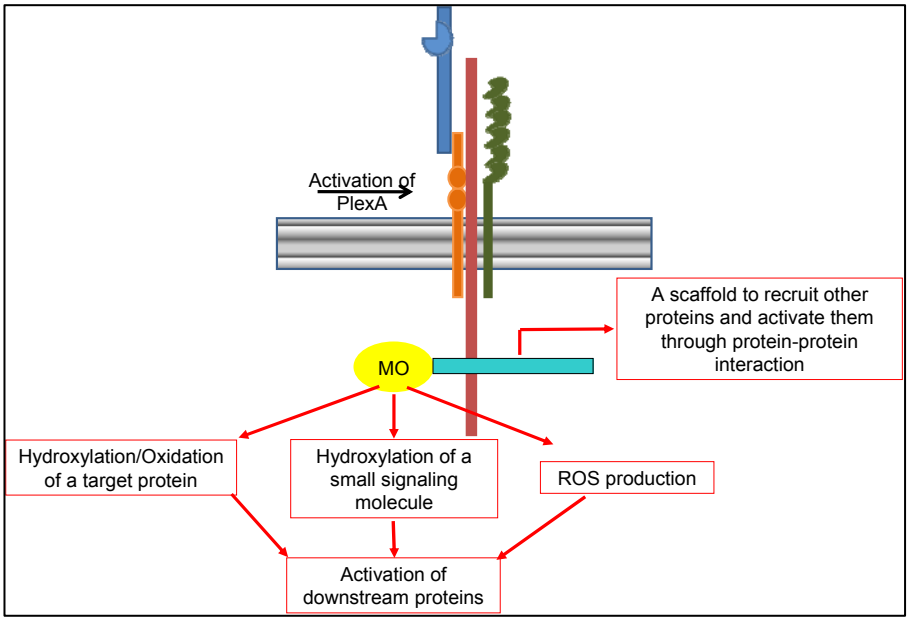

Figure 3.1.3: Proposed role for MICAL. Modified from (Kolk and Pasterkamp, 2007)

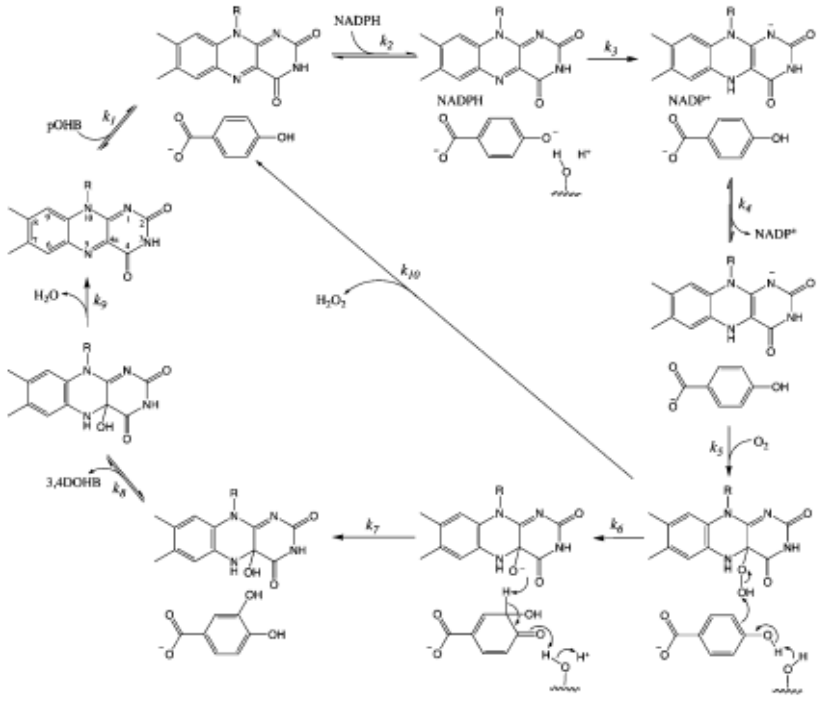

Figure 3.1.4: Catalytic cycle of p-hydroxybenzoate hydroxylase (Entsch et al, 2005).

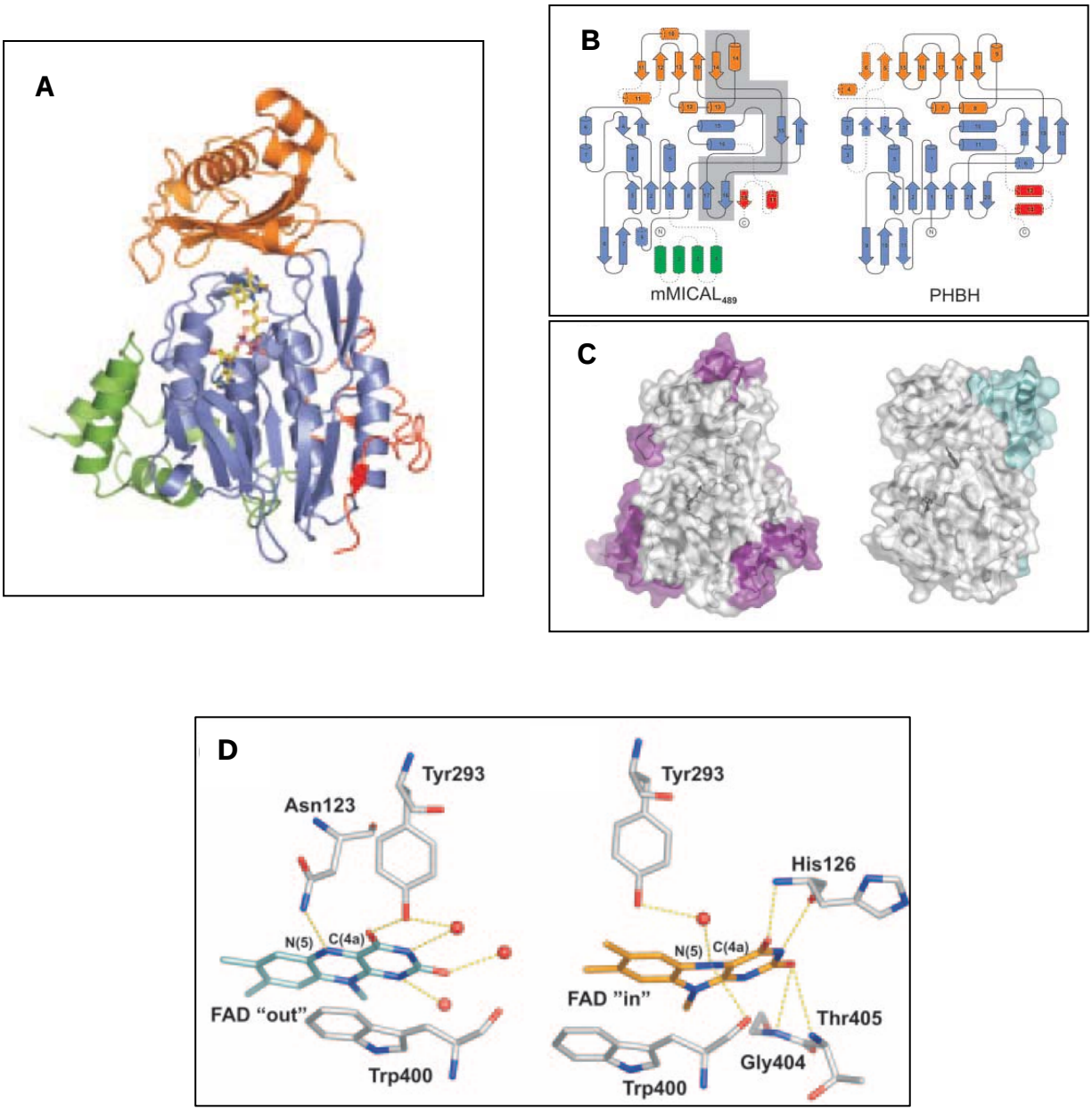

Figure 3.1.5: Panel A: Structure of mouse MICAL monooxygenase (MO) domain in the oxidized form. Green: four-helix bundle domain; cyan: the FAD-binding domain; orange: MO domain; red: linker region. The FAD molecule is depicted as sticks. Panel B: Structural comparison MICAL-MO (left) and PHBH (right). Domains are colored as in panel A. The grey-shaded area is deleted in the human splice isoform MICAL-1B. Panel C: Solvent accessible surface of MICAL-MO (left) and PHBH (right). Panel D: coordination of the isoalloxazine ring in the oxidized (left) and reduced (right) forms (Siebold et al, 2005).

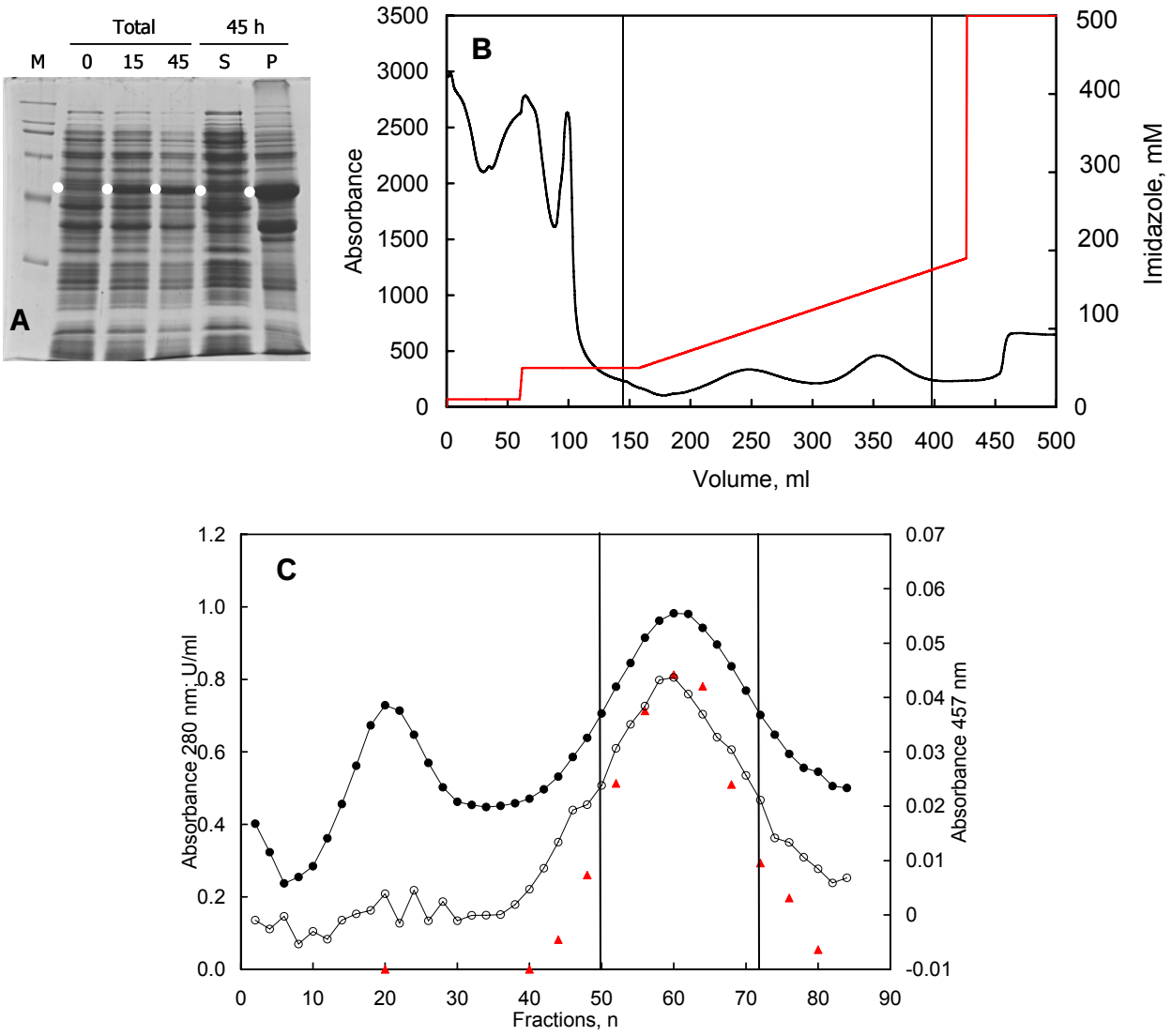

Figure 3.3.1. Expression levels of MICALHis and purification on Ni-NTA Sepharose. Panel A) *E. coli* Rosetta (DE3) cells transformed with pET23MICAL were grown to an OD_{600} of approximately 1 in a 12 l fermentor. One aliquot was withdrawn to prepare a whole cell extract for SDS-PAGE (Total, 0). The temperature was lowered to 15°C. IPTG (0.1 mM) was added. An aliquot of cells (0.5 lt culture) was harvested after 15 h and the rest after 45 h. These cells were used to prepare total cell extracts (Total, 15 and 45). The cells harvested at 45 h were homogenized and centrifuged to obtain the crude extract containing soluble proteins (S) and the pellet (P). The white dots mark the position of MICAL proteins. Panel B) Elution profile of the Ni-NTA Sepharose chromatography. Crude extract of cells containing MICALHis was loaded on Ni-NTA Sepharose. Weakly bound proteins were eluted with 50 mM imidazole. Elution of bound proteins was done applying a 50 to 300 mM gradient of imidazole in 50 mM sodium phosphate buffer, pH 7.5, 100 mM NaCl, 10% glycerol. Black: A_{280} measured in continuum; Red: concentration of imidazole. Vertical bars indicate fractions analyzed in details in panel C. Panel C: Detail of the profile of absorbance at 280 nm (●), 457 nm (o) and NADPH oxidase activity (▲) of fractions obtained after chromatography on Ni-NTA Sepharose. Vertical bars indicate fractions containing MICALHis that were pooled and concentrated.

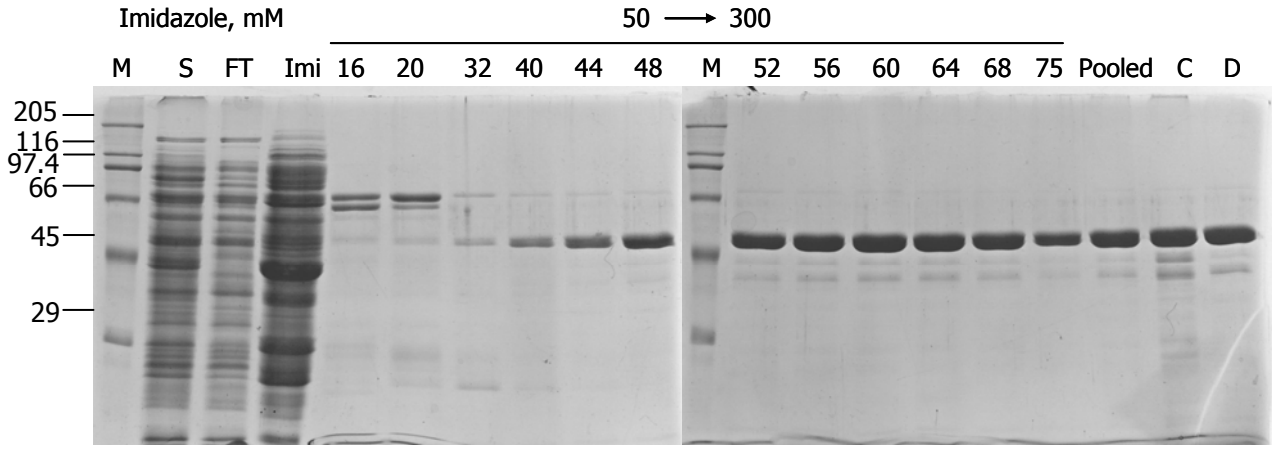

Figure 3.3.2: Purification of MICALHis on Ni-NTA Sepharose. SDS-PAGE of fractions eluted from Ni-NTA Sepharose column. S: crude extract (40 µg); FT: flow-through; Imi: weakly bound proteins eluted with 50 mM imidazole. Pooled: fractions pooled after Ni-NTA chromatography (5 µg); C: fractions pooled and concentrated (5 µg); D: MICAL-His after dialysis (5 µg).

Table 3.3.1: Purification of MICALHis on Ni-NTA Sepharose (from 43 g cells)

	Volume (ml)	Protein (mg)	Activity (U)	Specific Activity (U/mg)
Crude Extract	210	2940	6.8	0.0021
Ni-NTA Sepharose	32	18.7	32.6	1.7
Concentration & Dialysis	4.2	11.8	37.4	3.2

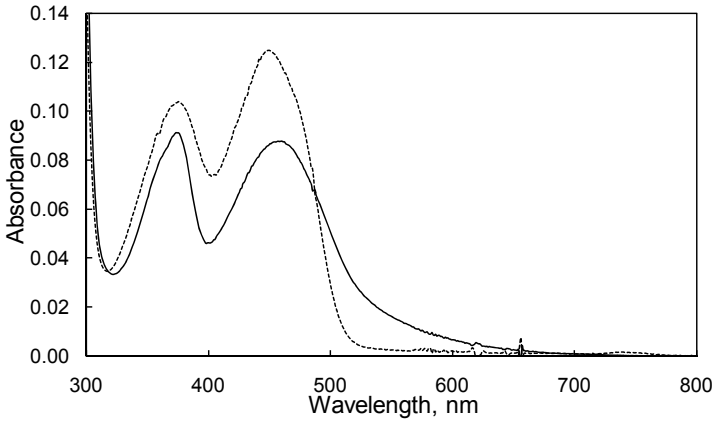

Figure 3.3.3. Absorption spectrum of human MICAL monooxygenase domain. The spectra of native MICALHis (12 µM based on the Bradford protein assay,) in 20 mM Hepes/NaOH buffer, pH 7.0, 10% glycerol, 1 mM EDTA, 1 mM DTT before (continuous line) and after denaturation by addition of SDS (0.2 %, dashed line) are shown.

Table 3.3.2: Determination of the stoichiometry and of the extinction coefficient of the bound FAD cofactor of MICALHis. Protein concentration was determined by the Bradford method. For calculation of flavin concentration the extinction coefficient of FAD at 450 nm (11.3 mM^{-1} cm^{-1}) was used. MICALHis was denatured in: [a] 50 mM sodium phosphate buffer, pH 7.2, 10% glycerol, 0.1 M NaCl, 1 mM DTT, 0.2% SDS; [b] Hepes/NaOH pH 7.0, 10% glycerol, 0.1 M NaCl, 1 mM EDTA, 1 mM DTT; [c] 10 mM Tris/HCl pH 7.5 buffer

Native			Denaturation	Denatured			Stoichiometry	ε
µM	λ max	Abs		λ max	Abs	µM		mM^{-1} cm^{-1}
8.7[a]	457	0.081	SDS	450	0.107	9.5	1.1	8.5
12.1[a]	457	0.088	SDS	450	0.122	10.8	0.9	8.0
13[b]	457	0.0829	SDS	450	0.114	10	0.8	8.2
14.3[b]	457	0.1	SDS	450	0.144	12.7	0.87	7.8
6.7[c]	457	0.0467	SDS	450	0.0645	5.7	0.85	8.1

Table 3.3.3: Determination of the FAD content in MICALHis preparations

Native protein		Denaturation	Denatured protein		Fluorescence Increment	[FAD] %
µM	Fluorescence Emission 530 nm		Fluorescence Emission 530 nm	Fluorescence Emission 530 nm +PDE		
0.44	0.2	SDS	2.9	23.0	7.9	97
0.51	0.06	SDS	3.8	30.1	7.9	97
0.61		SDS	4.6	32.31	6.6	94
0.28	0.09	100°C	2.1	20.8	9.9	100
0.53	0.12	100°C	3.95	40.2	10.1	100

Table 3.3.4. Steady-state kinetic parameters of the NAD(P)H oxidase activity of MICALHis. Assays were carried out at 25°C in 20 mM Hepes/KOH buffer, pH 7.0, in the presence of the indicated NAD(P)H concentration ranges and additions. k_{cat} and $K_{NAD(P)H}$ values, and their associated errors, were determined by fitting the data to the Michaelis-Menten equation (Eq. 2). The error was propagated according to Bevington (Bevington, 1969).

NADPH, µM	NADH, µM	NaCl, M	Glycerol, %	$K_{NAD(P)H}$, µM	k_{cat}, s^{-1}	$k_{cat}/K_{NAD(P)H}$, $s^{-1}mM^{-1}$
10-300				26±4	3.9±0.1	150 ± 23
	80-670			580±24	0.28±0.01	0.48 ± 0.03
40-650		0.1		499±28	2.6 ±0.1	5.2 ± 0.4
10-300			10	93±11	2.9±0.1	31.2 ± 4

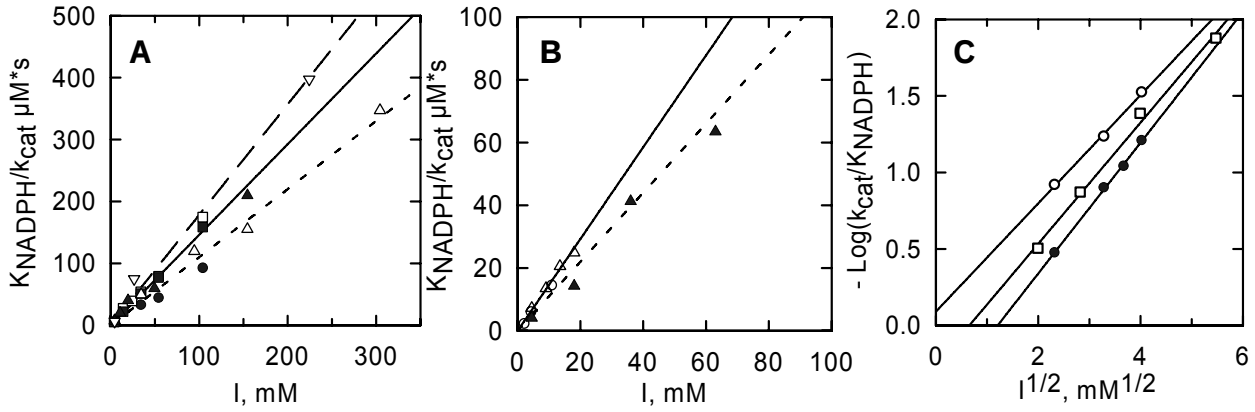

Figure 3.3.4. Effect of ionic strength and type of anions on MICAL-MO NADPH oxidase reaction. The slopes of double reciprocal plots obtained by measuring initial velocities in the presence of varying NADPH and different concentrations of salts or buffers are plotted as a function of the ionic strength of the assay mixture. Panel A: the following salts were added to the standard assay buffer (20 mM Hepes/KOH, pH 7.0): ●, sodium acetate; △, magnesium acetate; □, NaCl; ■, KCl; ▲, calcium chloride; ▽, sodium phosphate. Panel B: assays were carried out with different concentrations of Hepes/KOH buffer (○), Tris-chloride (△) or Tris-acetate (▲). Panel C: assays were carried out with different concentrations of imidazol-chloride (○), imidazol-acetate (□) or Bis-Tris-acetate (●). In panels A and B the continuous line is the common fit of the data obtained with the chloride salts; the dotted line is the common fit obtained with the acetate salts; the dashed line is the fit to the data obtained with sodium phosphate. In the C panel the lines are the fit of the data to Eq.8, derived from the limiting case of the Debye-Hückel equation (Eq. 7) described in (Nørby and Esmann, 1997)

Table 3.3.5: Effect of the ionic strength brought about by imidazole and Bis-Tris buffers on the k_{cat}/K_{NADPH} values of the NADPH oxidase reaction of MICAL. The values of the slopes of double reciprocal plots obtained from initial velocity measurements of reactions carried out in the presence of different concentrations of imidazole and Bis-Tris buffers were analyzed using Eq 8, derived from the limiting case of the Debye-Hückel equation (Eq.7, (Nørby and Esmann, 1997), Figure 3.3.4). The slope of the lines equals $-(z_e * z_{NADPH})$ and the intercept equals $\text{Log}(k_{cat}/K_{NADPH})$ at zero ionic strength $[(k_{cat}/K_{NADPH})_o]$. The charge of NADPH (z_{NADPH}) at pH 7.0 is between -3 and -4 taking into account the pK_a value of the 2'-phosphate group of 6.1. Therefore, the charge of the enzyme active site (z_e) can be calculated.

Buffer	slope	intercept	$z_e * z_s$	z_{NADPH}= -3	z_{NADPH}= -4	(k_{cat}/K_{NADPH}
Imidazole/chlori	0.35±0.02	0.09±0.06	-0.35±0.02	0.12	0.09	1.23
Imidazole/acetat	0.43±0.01	-0.52±0.04	-0.43±0.01	0.14	0.11	0.31
Bis-Tris/acetate	0.40±0.02	-0.26±0.08	-0.34±0.02	0.13	0.10	0.55
			Average	0.13	0.10	

Table 3.3.6. Effect of PEG 8000 on the kinetic parameters of the NADPH oxidase reaction of MICAL. Initial velocity data obtained at 25°C in 20 mM Hepes/NaOH buffer, pH 7.0, in the presence of varying concentrations of NADPH and different levels of PEG8000 (see Figure 3.3.9 panel C) were fitted independently with the Michaelis-Menten equation (Eq. 2). The effects of increasing solvent viscosity with PEG8000 on k_{cat} and k_{cat}/K_{NADPH} were calculated and fitted to a straight line as a function of relative viscosity. The values of the slopes and intercepts of these lines are in Table 3.3.8.

PEG8000 (%, w/v)	η_{rel}	k_{cat}, s^{-1}	K_{NADPH}, μM	k_{cat} / K_{NADPH}, $s^{-1}mM^{-1}$
0	1.0	2.9 ± 0.05	36.3 ± 2.5	80 ± 6
1.7	1.6	3.0 ± 0.08	43.9 ± 4.3	68 ± 7
3.3	2.0	2.9 ± 0.13	57.7 ± 7.3	51 ± 7
6.7	3.6	2.7 ± 0.07	44.2 ± 3.9	61 ± 6

Table 3.3.7. Effect of glycerol and sucrose on the kinetic parameters of the NADPH oxidase reaction of MICAL. Initial velocity data obtained at 25°C in 20 mM Hepes/NaOH buffer, pH 7.0, in the presence of varying concentrations of NADPH and different levels of glycerol or sucrose (see Figure 3.3.9 panel A and B) were fitted with Eq. 6. The parameters m and n allow to calculate the effect of viscosity on k_{cat} and k_{cat}/K_{NADPH}, respectively (Figure 3.3.9 panel D). The calculated values as a function of the relative viscosity of the solvent were fitted to a straight line. The values of the slopes and intercepts (when present) are in Table 3.3.8.

Viscogen	k_{cat}, s^{-1}	K_{NADPH}, μM	m	n
Glycerol	2.8 ± 0.04	47.2 ± 2.5	1.09 ± 0.16	0.34 ± 0.05
Sucrose	3.0 ± 0.07	35.6 ± 3.1	1.47 ± 0.25	0.44 ± 0.05

Table 3.3.8. Effect of solvent viscosity on k_{cat} and k_{cat}/K_{NADPH}. The data shown in Figure 3.3.9 A-C were fitted as described in the legends of Tables 3.3.6 and 3.3.7. The effects of viscosity on k_{cat} and k_{cat}/K_{NADPH} (expressed as the ratio of the parameter calculated in the absence of the viscogen over the value calculated in the presence of a given viscogen concentration) exhibited a linear dependence on the relative viscosity brought about by the corresponding viscogen concentration. For the effect of glycerol and sucrose on k_{cat}, the best line has an intercept equal to zero.

	Effect of viscosity on			
	k_{cat}		k_{cat}/K_{NADPH}	
Viscogen	slope	intercept	slope	intercept
Glycerol	0.97 ± 0.01	-	3.0 ± 0.1	– (2.1 ± 0.2)
Sucrose	1.04 ± 0.03	-	4.2 ± 0.3	– (3.3 ± 0.3)
PEG8000	0.04 ± 0.01	0.94 ± 0.03	0.1 ± 0.14	– (1.1 ± 0.3)

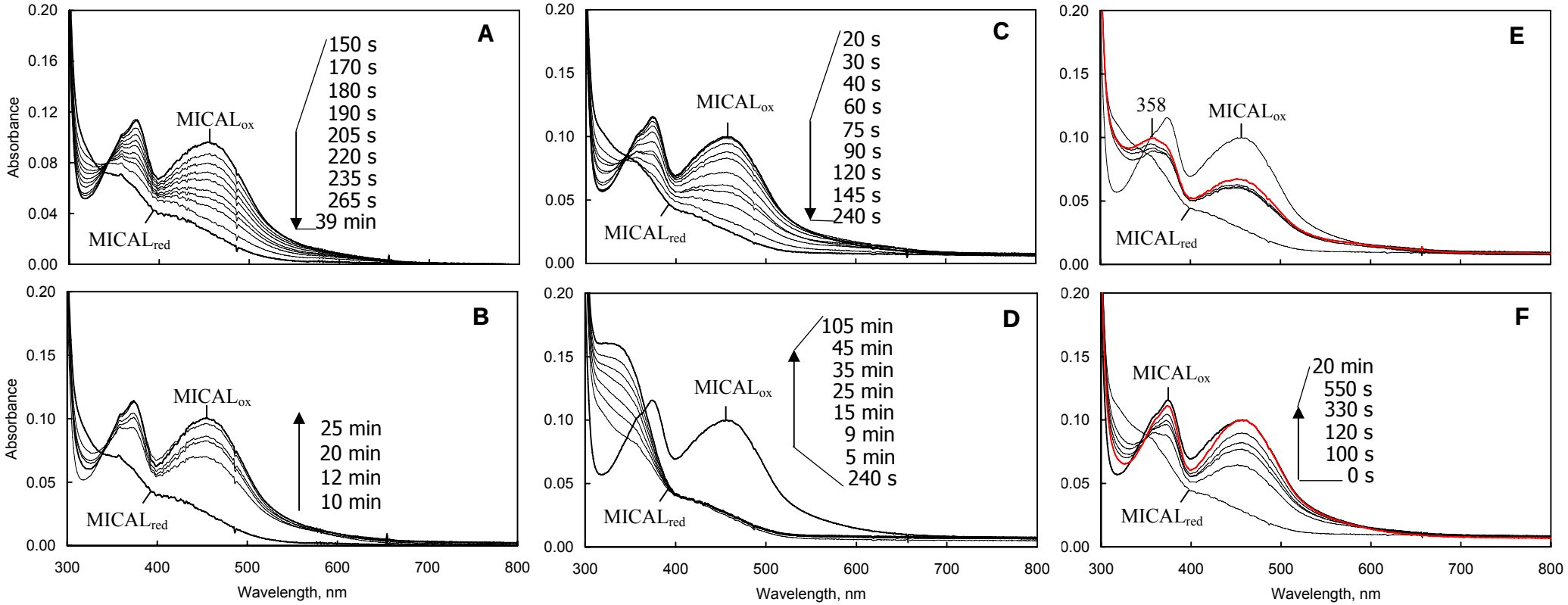

Figure 3.3.5. Photoreduction of MICAL-MO. A solution containing MICAL-His (10 µM), EDTA (10 mM), 5-deaza, 5-carba riboflavin (1 µM) in 20 mM Hepes/NaOH buffer, pH 7.0, 1 mM DTT and 10% glycerol was made anaerobic in the absence (Panel A-B) and presence (Panel C-F) of $NADP^+$ (30 µM). The solution was irradiated with a standard projector lamp for different times. In the first part of the experiment (Panel A and C), complete reduction of MICAL flavin cofactor was observed (spectrum marked as $MICAl_{red}$). With further irradiation formation of NADPH was observed in the presence of $NADP^+$ (Panel D). The solution was then exposed to air by opening the cuvette and gentle mixing (Panel B and E). in the absence of $NADP^+$, the spectrum of the oxidized enzyme was recovered without detection on intermediate species (Panel B). In the presence of $NADP^+$, a first, partial oxidation of the flavin was observed with oxidation of NADPH and appearance of an absorption peak centered at 358 nm (panel E, red line), which partially decayed. A second mixing of the solution with air (Panel F) led to loss of this peak of abosorbance and full oxidation of the flavin (red line). The spectrum of the $MICAl_{ox}$ and of $MICAl_{red}$ (prior to accumulation of NADPH) is shown for reference in panels E and F. In Panel A, C and D the total irradiation times are shown; in B and F, the times after the mixing with air are shown. “0 s” indicates the spectrum before mixing with air the second time.

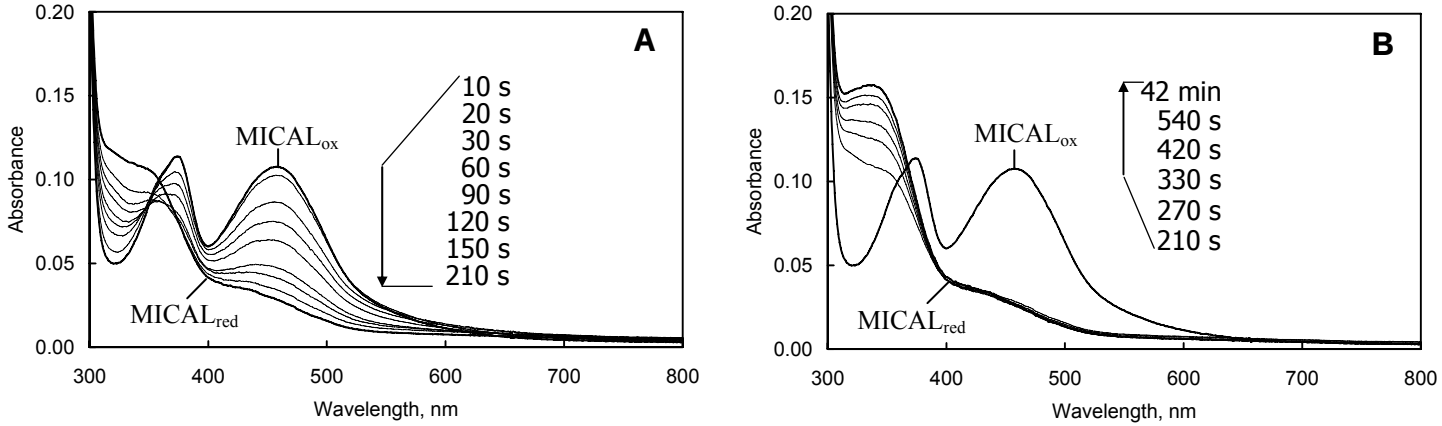

Figure 3.3.6: Anaerobic reduction of MICALHis in the presence of $NADP^+$, glucose-6-phosphate and glucose-6-phosphate dehydrogenase. A solution containing MICALHis (10 µM), $NADP^+$ (15 µM) and glucose-6-phosphate (1 mM) in 20 mM Hepes/NaOH buffer, pH 7.0, 1 mM DTT and 10% glycerol was made anaerobic (Panel A, spectrum marked as $MICAL_{ox}$). Glucose-6-phosphate dehydrogenase (1 U) was added to start the generation of NADPH and spectra were collected at the indicate time. Panel A: first part of the reduction ,with the formation of the completely reduced flavin ($MICAL_{red}$). An isosbestic point at 348 nm was observed. Panel B: accumulation of NADPH during the second part of the reduction.

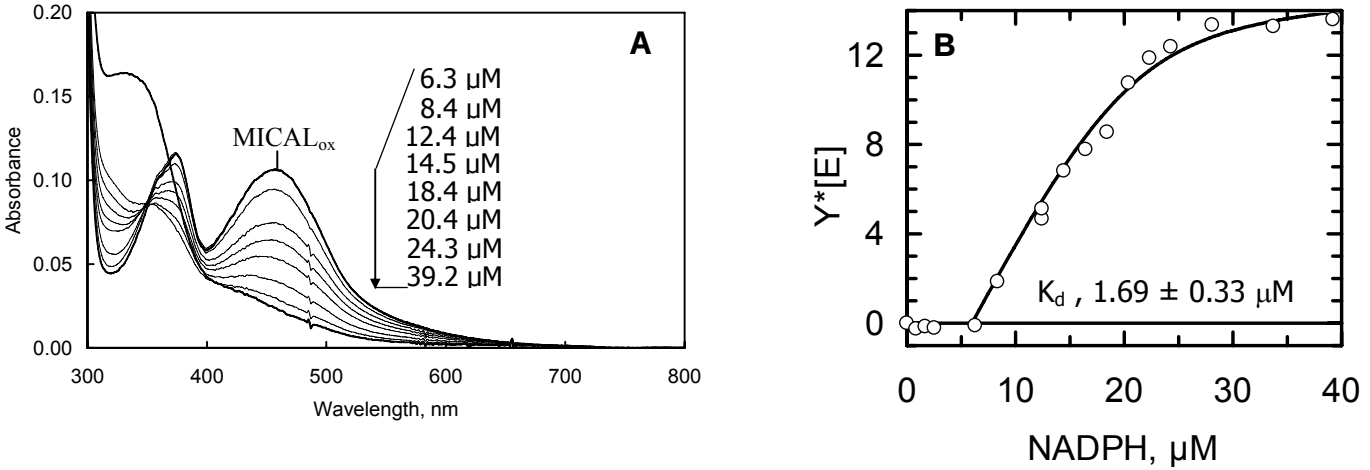

Figure 3.3.7: Anaerobic titration of MICALHis with NADPH. A solution containing MICALHis (13 µM) in 20 mM Hepes/NaOH buffer, pH 7.0, 1 mM DTT and 10% glycerol was made anaerobic (Panel A, spectrum marked as $MICAL_{ox}$). A NADPH solution (0.51 mM) was added at the final concentration indicated (Panel A) and spectra collected after each addition. Panel B) Fitting of the fractional absorbance changes at 457 nm ($Y = ((A_x-A_o)/(A_f-A_o))$ corrected for the enzyme concentration to Eq 9.

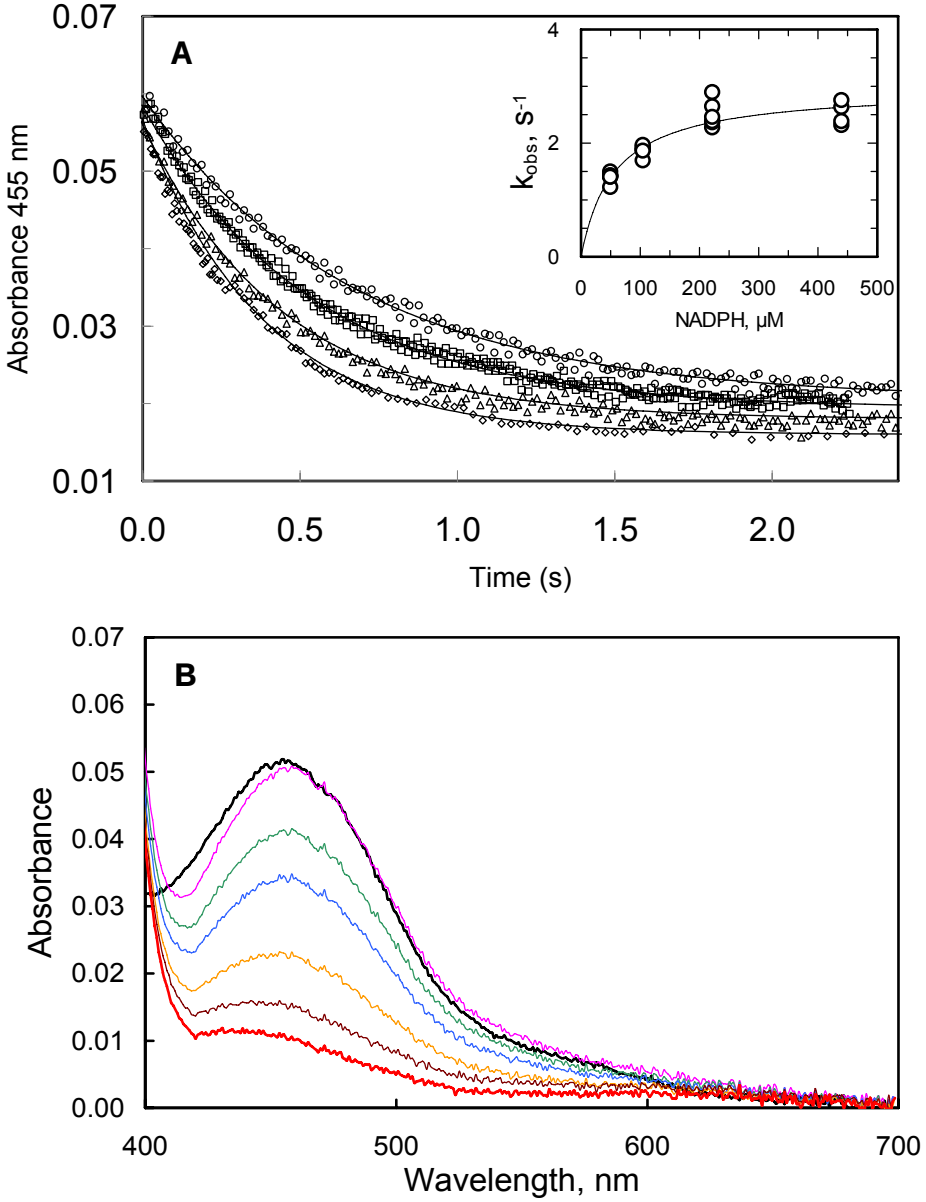

Figure 3.3.8. Reaction of MICAL-MO with NADPH. Panel A) MICAL-MO (7.5 μM) was reacted anaerobically with NADPH (circles, 50 μM; squares, 105 μM; triangles, 222 μM; diamonds, 440 μM after mixing) in 20 mM Hepes/NaOH, pH 7.0, 10% glycerol, 1 mM DTT, 1 mM EDTA at 25°C in the stopped-flow spectrophotometer. The observed absorbance changes at 455 nm were fitted to a single exponential equation (lines). The data were not corrected for baseline drifts (determined by acquiring the spectra of the NADPH solutions before each series of shots) to avoid overlapping of the traces. The inset shows the plot of the measured rate constants as a function of NADPH and their fit to a hyperbole yielding k_{red}, 3 ± 0.1 s-1 and $K_M(K_d)$, 56 ± 7.3 μM. Panel B) Selected spectra observed during the reaction of MICAL (7.5 μM) with NADPH (222 μM) in 20 mM Hepes/NaOH buffer, pH 7.0, 10% glycerol, 1 mM DTT, 1 mM EDTA.

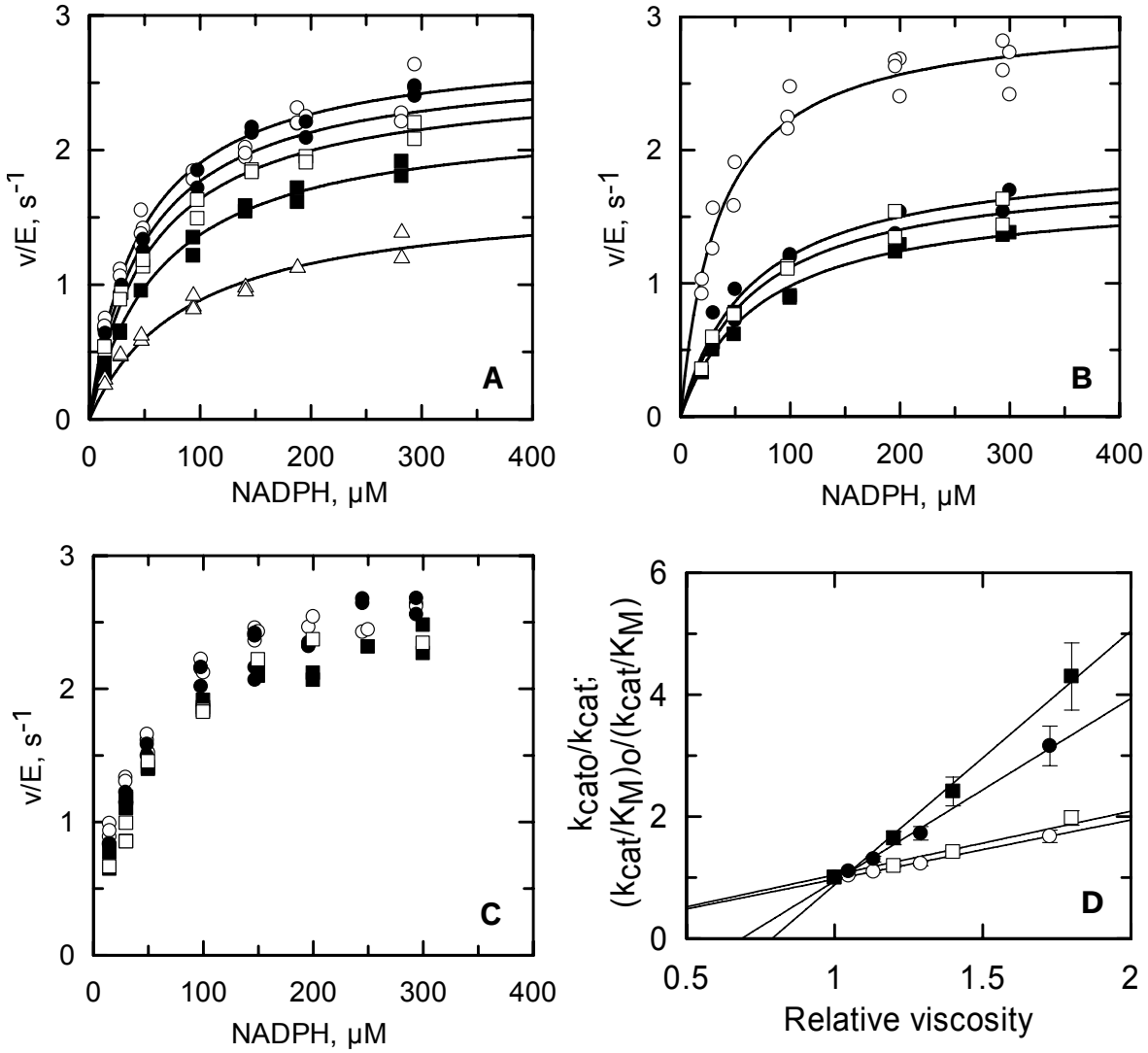

Figure 3.3.9: Effect of glycerol, sucrose and PEG8000 on the MICAL NADPH oxidase reaction. Initial velocity measurements were carried out at 25°C in the presence of varying NADPH concentrations and fixed levels of glycerol (A), sucrose (B) and PEG8000 (C). Viscogen concentrations and relative viscosity were as follows: Panel A, glycerol (%, η_{rel}) 0,1 (o); 2.5, 1.04 (●); 5, 1.13 (□); 10, 1.29 (■) and 20, 1.72 (Δ). Panel B: sucrose (%, η_{rel}) 0,1; 13.3, 1.2; 15.6, 1.4; 21.3, 1.8; Panel C: PEG 8000 (%,η_{rel}) 0,0 (o); 1.7, 1,6 (●); 3.3, 2 (□) and 6.7, 3.6 (■). In panel A and B the curves are the best fit of the data to Eq 6. The calculated parameters are in Table 3.3.7 and they were used to calculate the effect of viscosity on k_{cat} and k_{cat}/K_{NADPH} (see Table 3.3.8 and panel D). In Panel C only a scatter graph is presented for clarity. The kinetic parameters calculated by fitting independently the curves obtained at the different PEG8000 concentrations are summarized in Table 3.3.6. The negligible dependence of the MICAL reaction on PEG8000 was confirmed by the analysis of the dependence of the effects on k_{cat} and k_{cat}/K_{NADPH} on the relative viscosity of the medium (Table 3.3.8). Panel D) Effect of viscosity brought about by glycerol (circles) and sucrose (squares) on k_{cat} (open symbols) and k_{cat}/K_M for NADPH (closed circles). The initial velocity data shown in panel A and B were fitted as described in Table 3.3.7. The effects of viscosity on k_{cat} and k_{cat}/K_{NADPH} were fitted to the straight lines shown here. The parameters are in Table 3.3.8.

Figure 3.3.10: Pyrene actin polymerization assays in the presence of MICAL-MO. G-Pyrene actin (5.7 μM, in 5 mM Tris/HCl buffer, pH 8.0, 0.2 mM $CaCl_2$, 0.2 mM ATP, 1 mM DTT) was polymerized by addition of the polymerization buffer (P) and the fluorescence signal was measured (λ_{ex} 365 nm, λ_{em} 407 nm; Panel A and B, trace (a)). The effect of MICAL-MO (M; 0.7 μM) and NADPH (100 μM) on the polymerization rate was studied, by adding the enzyme before the reductant (Panel A, trace (b)) or vice versa (Panel A, trace (c)). Panel B: MICAL-MO (0.7 μM) enhances the depolymerization of actin in the presence of NADPH (100 μM; trace (d)). The same effect was observed when MICAL (trace (e)) or NADPH (trace (f)) were added before the polymerization buffer. Panel C: assays carried out in the dilution buffer in the absence of actin. Variation of the fluorescence intensity were monitored after addition of the polymerization buffer (P, trace (g)), MICALHis and NADPH (traces (h) and (i)). NADPH emission signal reached a value of 6, as confirmed by the emission spectrum in figure 3.3.12. This value decreased linearly after MICAL addition (trace (i)) as a consequence of the NADPH consumption by MICALHis. Numbers indicate the variation of fluorescence/min. Panel D: NADPH oxidase activity of MICAL (0.7 μM) in the presence of NADPH (100 μM). Assays were carried out at 25°C in the dilution buffer (trace (m)) and in the polymerization buffer (trace (l)). The NADPH is completely oxidized within 5 min in the dilution buffer (trace (m)) and within 15 min in the polymerization buffer (trace (l)). Numbers indicate the Δ/min. Traces were shifted along y axis for clarity (trace (a), panel A: 220 units; trace (a) panel B: 500 units; trace (b): 110 units; trace (d): 350 units; trace (e): 150 units; trace (g): 20 units; trace (h): 10 units; trace (l): 0.2 units).

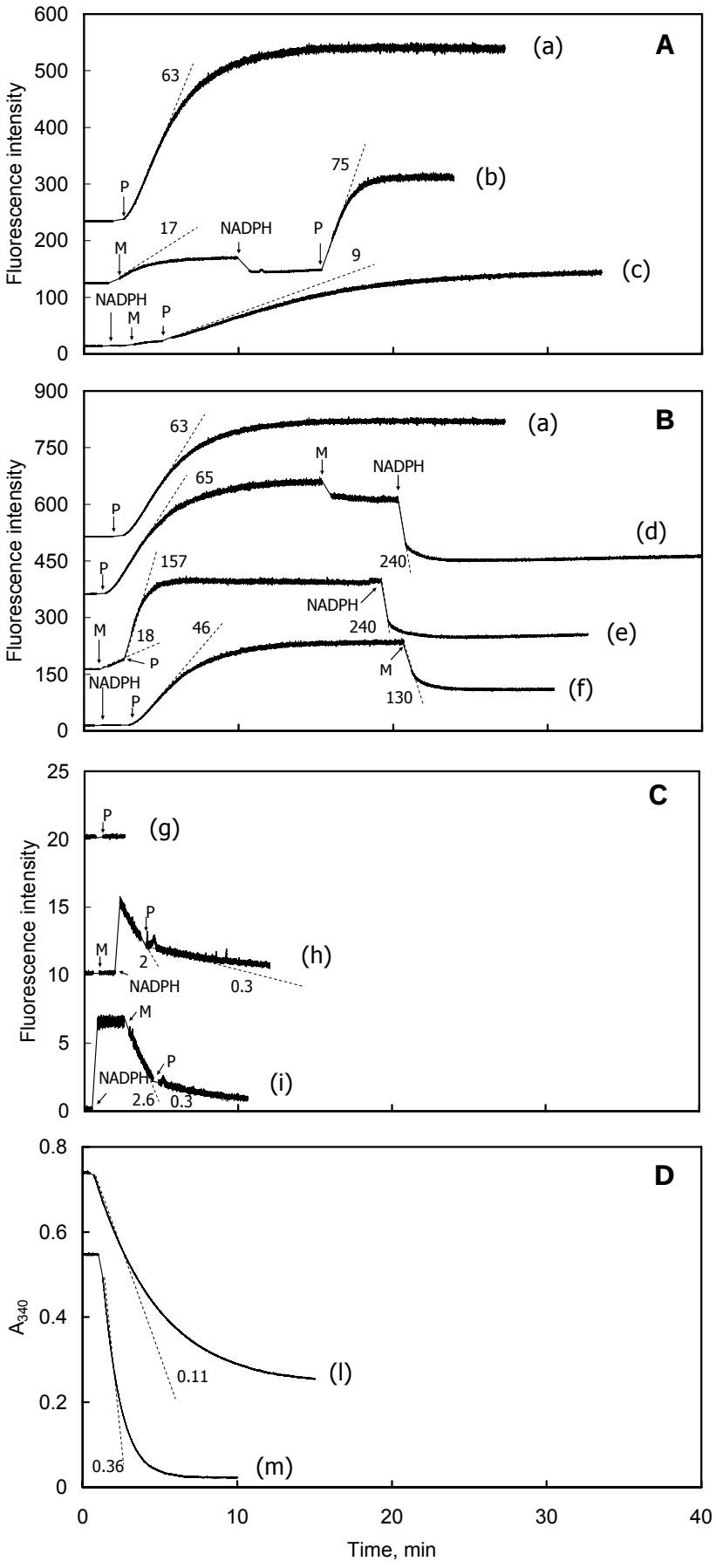
A
B
C
D
(a)
(b)
(c)
(d)
(e)
(f)
(g)
(h)
(i)
(l)
(m)
63
75
17
9
65
157
240
46
18
2
0.3
2.6
0.11
0.36
130
NADPH
P
M
Fluorescence intensity
A_{340}
Time, min

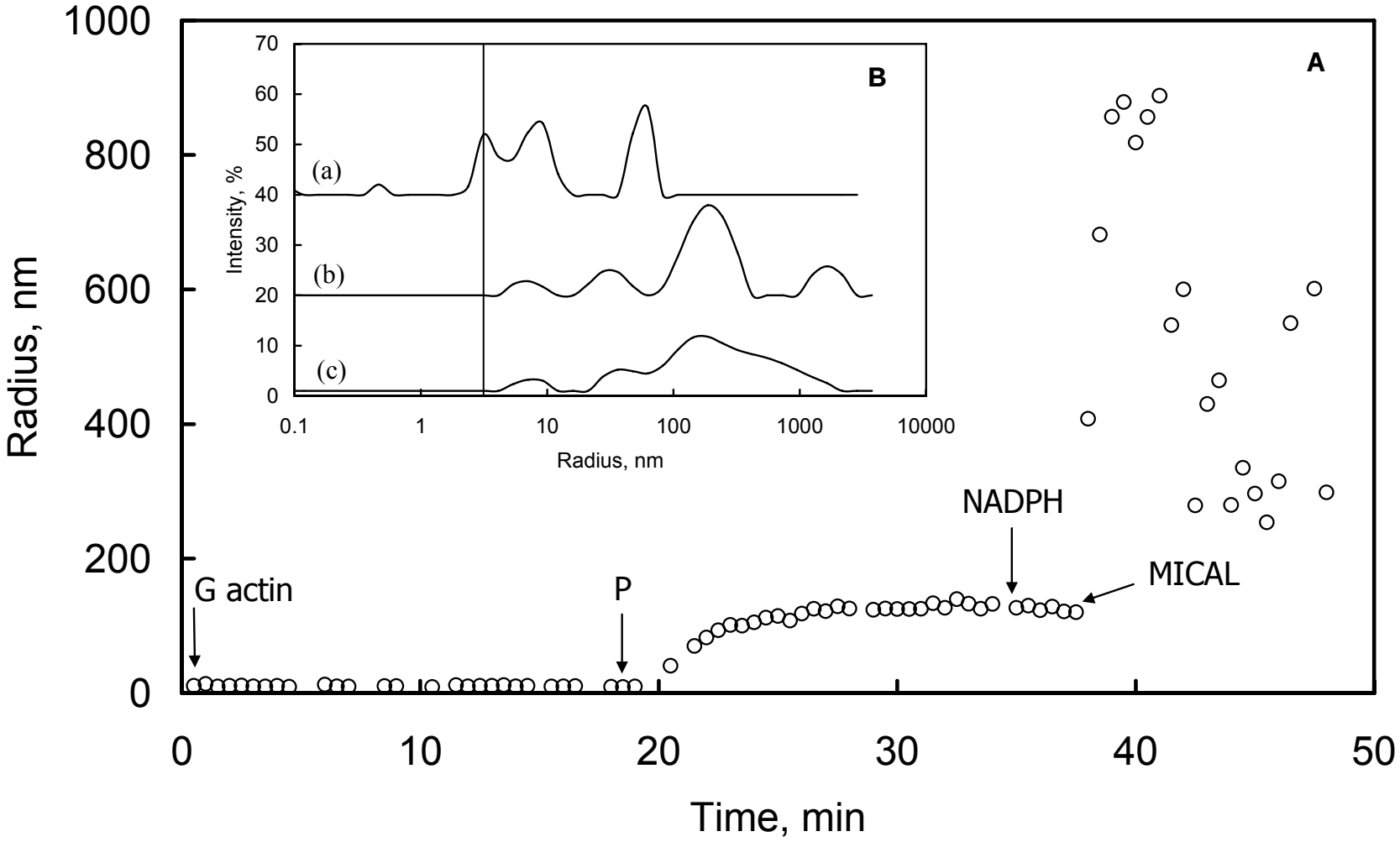

Figure 3.3.11: Actin polymerization assays at the dinamic light scattering (DLS). Panel A: Mean radius values of the ultracentrifuged G actin solution (G actin, 5.4 μM). Polymerization buffer (P) was added to the solution in DLS cuvette. At the end of the polymerization, NADPH (100 μM) and MICALHis (0.7 μM) were added. Panel B: Species of different radius were detected in the G actin solution (a), during polymerization (b) and after NADPH addition (c). The expected radius for G actin is indicated (3.2 nm, 44 kDa).

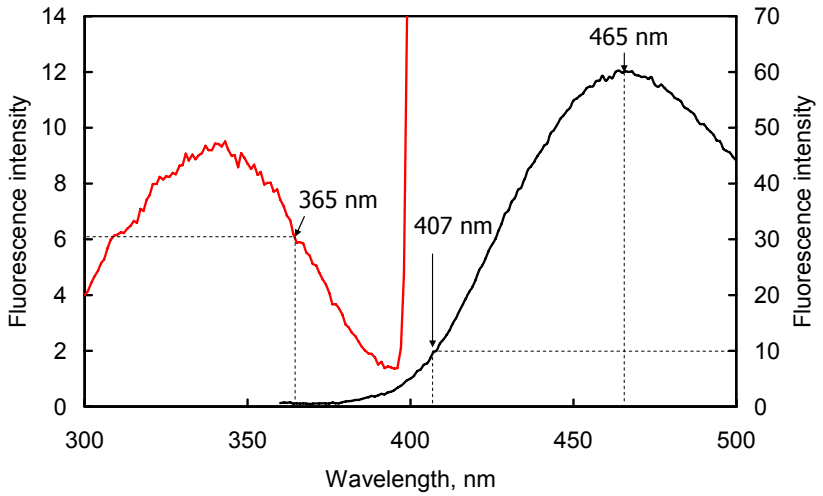

Figure 3.3.12: Excitation and emission and spectra of NADPH. Excitation (red; λ_{em} 407 nm) and emission (black; λ_{ex} 340 nm) spectra of 100 µM NADPH in dilution buffer (5 mM Tris/HCl buffer, pH 8.0, 0.2 mM $CaCl_2$, 0.2 mM ATP, 1 mM DTT).

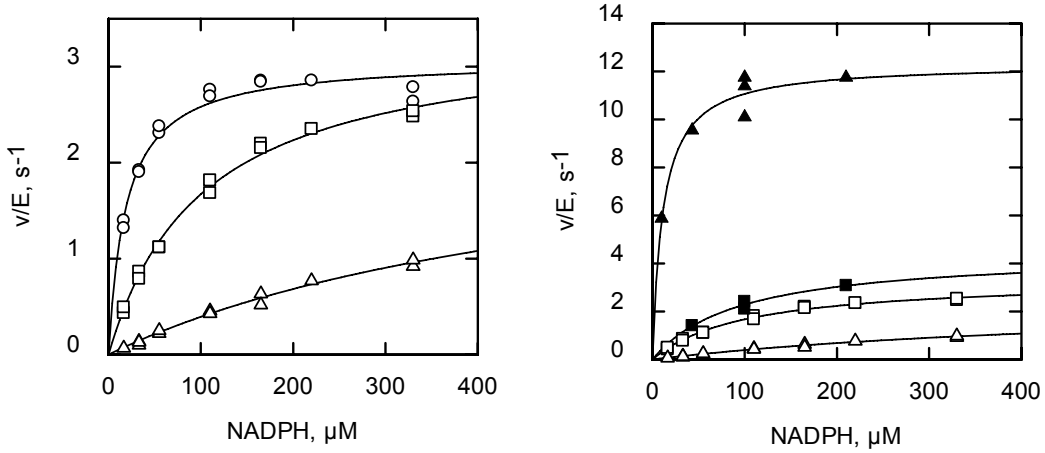

Figure 3.3.13: NADPH oxidase activity of MICALHis in the presence of Hepes/KOH buffer pH 7.0 (o), dilution buffer (□), polymerization buffer (Δ), G actin (■) and F actin (▲). Assays were carried out at 25°C in the presence of different concentration of NADPH (15-300 µM).

Table 3.3.9: Kinetic parameters for the NADPH oxidase activity of MICALHis in the presence of of Hepes/KOH buffer pH 7.0, dilution buffer, polymerization buffer, G actin and F actin.

Buffer	**Actin**	**k_{cat} s^{-1}**	**K_{NADPH} µM**	**V/K s^{-1} μM^{-1}**
Hepes/KOH pH 7.0	-	3.1 ± 0.1	19 ± 2	0.163 ± 0.018
Dilution buffer	-	3.4 ± 0.1	101 ± 8	0.034 ± 0.003
Dilution buffer	G actin	4.5 ± 0.6	96 ± 28	0.047 ± 0.015
Polymerization buffer	-	2.6 ± 0.4	554 ± 118	0.005 ± 0.001
Polymerization buffer	F actin	12.3 ± 0.5	11 ± 3	1.12 ± 0.31

4. ON THE ROLE OF S371 OF FLAVOCYTOCHROME b2

4.1 INTRODUCTION

Flavocytochrome b_2 (L-lactate cytochrome *c* oxidoreductase, EC 1.1.2.3, Fcb2) is a homotetrameric yeast enzyme, which catalyzes the oxidation of L-lactate (Lac) to pyruvate (Pyr) with concomitant reduction of cytochrome *c* (Cyt *c*). During the catalytic cycle Lac binds to the flavodehydrogenase (FDH) domain and is oxidized to Pyr with transfer of the reducing equivalents to the bound flavin mononucleotide (FMN), yielding its hydroquinone form:

$$\text{L-lactate} + \text{E-FMN}_{ox} \rightarrow \text{Pyruvate} + \text{E-FMN}_{red}$$

The reduced flavin then transfers electrons one at a time to heme b_2 in the N-terminal protein domain with the intermediacy of the flavin semiquinone species. Cyt *c* is the physiological acceptor for heme b_2 (Lederer, 1991). The crystal structure of Fcb2 was solved for the wild-type enzyme and for several mutants. The tetramer is composed of four identical subunits (57000 Da), each formed of two structural domains, the hemoprotein (residues 1-100) and the flavodehydrogenase domain (FDH, residues 101-487). The C-terminal end of the subunit (residues 488-511) makes contacts in the center of the tetramer with each of the three other flavin domains (Figure 4.1.1; Xia et al, 1987). The L-lactate oxidation reaction occurs in the FDH domain. The hemoprotein, whose structure is highly reminiscent of the cytocrome b5 fold, contains a eme b_2 prosthetic group located in a crevice (Xia et al, 1990). Contacts between the cytochrome domain and the FDH domain are favoured by the partial mobility of the heme-containing portion, as demonstrated by the tetramer crystal structure, where two hemoprotein domains were disordered (Xia et al, 1990). The flavodehydrogenase domain is composed of a $\alpha_8\beta_8$ barrel and contains a FMN cofactor bound at the end of the β-barrel, corresponding to the C-terminus of the β-strands. The resolution of the structure in the presence of pyruvate led to the identification of residues important for the substrate binding and for the catalysis (see below).

Several studies on Fcb2 have focused on the mechanism of Lac dehydrogenation catalyzed by its FDH domain. The latter is the structural and mechanistic prototype of a family of α-hydroxyacid dehydrogenases (as reviewed in, e.g., (Lederer, 1991; Fitzpatrick, 2001; Fitzpatrick, 2004; Lederer et al, 1996 and Lederer et al, 2005)) which includes, as well characterized members, glycolate oxidase (GOX) (Lindqvist, 1991), L-lactate monoxygenase (LMO) (Maeda-Yorita et al, 1995), L-lactate oxidase (LO) (Maeda-Yorita et al, 1995), mandelate dehydrogenase (MDH) (Lehoux et al, 1999) and long chain α-hydroxy acid oxidase (LCHAO) (Cunane et al, 2005). Components of this

extended family play important roles in the metabolisms of a wide number of organisms and some of them are also of significant interest for industrial and medical purposes. This is the case of GOX, that is associated to pathologies in the metabolism of oxalate in animals and more generally to enzymatic deficiencies of the perixosomes, where it is located.

These enzymes are believed to share a common mechanism for the oxidation of the α-hydroxy acid substrate in the enzyme reductive half reaction, which formally implies the loss of two electrons and two protons during the conversion to the corresponding α-keto acid. In all cases, the acceptor of the reducing equivalents is the bound FMN. The enzymes of the Fcb2 family differ with respect to the oxidative half reaction leading to dehydrogenases or oxidases. Two mechanistic hypotheses for the α-hydroxy acid dehydrogenation reaction have been formulated and tested over the past decades. The so-called "proton abstraction" (PA) or "carbanion" mechanism predicts that the bound α-hydroxy acid undergoes abstraction of the α-hydrogen (Hα) as a proton by an active site base with formation of an α-carbanion intermediate. The latter would evolve, probably by two single electron transfer steps to yield the flavin hydroquinone and the α-keto acid product (Scheme 1A). The alternative "hydride transfer" (HT) mechanism predicts that the substrate Hα is directly transferred to the flavin N5 position as a hydride anion with elimination of the α-hydroxyl proton (Scheme 1B). For none of the enzymes of the Fcb2 family, the mechanism of substrate dehydrogenation has been definitely established, as discussed in, e.g.(Fitzpatrick, 2001; Lederer, 1996; Lederer et al, 2005).

In support of the PA mechanism there are several observations made on Fcb2 as well as on other enzymes of its structural family. Among them is the reported pK_a of 9 in the reduced enzyme for the group which abstracts the substrate Hα, which has been considered too low for being that of the reduced FMN N5 atom (Balme et al, 1994; Rao et al, 1998), which has been estimated to be ~20 for the free flavin, and the decrease of one unit of the pK_a of this group induced by the D282N mutation (Gondry et al, 1996). Furthermore, studies of the transhydrogenation reactions between 2-^{2}H-lactate (or 2-^{3}H-lactate) and bromopyruvate led to isotope effects, which could be rationalized only in the frame of a PA mechanism (Gondry et al, 1996; Urban et al, 1985).

On the other hand, other results can be better interpreted as to indicate that the HT mechanism is operative. For example, Fcb2 can oxidize lactate when FMN is substituted by 5-deaza-5-carba-FMN (Pompon et al, 1979), which is known to be an obligatory acceptor of hydride anions. Furthermore, substrate and solvent kinetic isotope effects have now been interpreted within a HT mechanism with asynchronous αOH proton abstraction and hydride transfer to FMN-N5 (Fitzpatrick, 2004; Sobrado et al, 2003).

A number of other results on Fcb2 and related enzymes could be interpreted within the framework of both the proposed mechanisms (Schema 1). Site-directed mutagenesis of active site residues in

various family members yielded interesting information in terms of role of active site residues in substrate binding and/or transition state stabilization, but, unfortunately, did not provide decisive mechanistic evidences. H373 is the proposed active site base that abstracts Lac Hα or α-OH as a proton. This residue is hydrogen bonded with D282, that stabilizes the acid-base properties and the orientation of H373. Other conserved residues are Y143 and R376 that form interactions with the Pyr carboxylate group; Y254 that is hydrogen bonded with O(2) carbonyl and stabilizes the transition state; R289 that interacts with D292, modulating the properties of R376, proximal to the substrate. K349 stabilizes the negative charge of $FMNH^-$ after the reduction reaction (Gondry et al, 1996; Cunane et al, 2002; Gondry et al, 2001; Reid et al, 1988, Xia et al, 1990; Mowat et al, 2004) (Figure 4.1.2).

A key missing information is the structure of a complex between the enzyme and a true substrate analog defining the structure of the Michaelis complex of Fcb2. Indeed, the crystal structure of wild-type Fcb2 (Xia et al, 1990) had the reaction product Pyr bound to the active site, where FMN is believed to be in the semiquinone form. Furthermore, none of the crystal structures available to date for Fcb2 and the enzymes of the family provides a definitive mechanistic answer.

Recently, to gain insight into the mechanism of Fcb2-catalysed L-lactate oxidation, minimal models of the enzyme active site in complex with the L-lactate substrate have been built by a fully quantum-mechanical approach starting from the available crystal structures. Following structural optimization (at 0 K) and finite temperature (300 K) molecular dynamics simulations, a stable complex with L-lactate poised for hydride transfer was obtained (Figure 4.1.3; Tabacchi et al 2005). Simulation of the lactate dehydrogenation reaction according to such a mechanism led to the observation of a free energy profile characterized by a single transition state and a free energy of activation of 12.1 kcal/mol consistent with that determined experimentally (13.5 kcal/mol). During the simulated reaction, transfer of the lactate αH, as a hydride anion, to FMN N(5) position was preceded by transfer of the α-OH proton to H373 Nε yielding a short-lived lactate alkoxide species, which underwent oxidation, and the positively charged H373 forming an ion pair with D282 carboxylate (Figure 4.1.4 panel B and C).

During the model building process it was observed that a crystallographically-detected active site water molecule (Wat609 in the PDB file 1fcb, Figure 4.1.4 panel A-C and Figure 4.1.5) modulated the proton affinity of the active site base, H373 of Fcb2 (Tabacchi et al, 2005; Tabacchi et al, 2009). In particular, during molecular dynamics simulations at 300 K, in an active site model not including Wat609 proton transfer events from the fragment mimicking H373 Nδ to that mimicking D282 carboxylate O1 was observed, yielding a negatively charged histidinate and neutral D282 carboxylic acid (Figure 1D, E). However, inclusion of Wat609 in the active site model led to

preserving the neutral H373/negatively charged D282 carboxylate couple (Figure 4.1.4 panel A). Starting from the model lacking Wat609 a series of constrained molecular dynamics simulations were also performed to test the reactivity of the model. As expected from the molecular dynamics simulations at 300 K of the enzyme-lactate complex, at the very early stages of the simulated reaction (i.e.: as lactate αH was pulled away from lactate), a proton was transferred from lactate αOH group to H373 Nε, and the H373 Nδ hydrogen was transferred as a proton to D282 carboxylate. As depicted in Figure 4.1.4 panel E, these proton transfer events led to an active site model containing the lactate alkoxide, neutral H373 and neutral D282. The calculated free energy barrier for this step was very low (0.4 kcal/mol) and the energy level of the resulting enzyme-substrate complex was essentially unchanged with respect to the initial Michaelis complex. However, the simulation of the reaction beyond this initial phase failed. Increasing the value of the reaction coordinate led to a system that was unstable and no relative minima of the constraint force could be calculated. On the contrary, including Wat609 in the model led to the free energy profile described above in which H373 remains neutral and hydrogen bonds to D282 γ-carboxylate (with Nδ) and to the bound substrate (with Nε) until the lactate αOH proton is transferred to H373 Nε, just before the transition state (Tabacchi et al, 2005). At this stage H373 is positively charged and forms an ion pair with Asp282 (Figure 4.1.4 panel C). All these findings agree well with the fact that all evidence accumulated so far on Fcb2 supports that H373 is neutral in the oxidized active site (Lederer 1991; Lederer, 1992). During lactate oxidation, H373 would abstract one of the substrates protons (the αH or α-OH proton, depending on the postulated mechanism) undergoing a pK_a increase (up to ~15) in the reduced enzyme (Lederer, 1992). The pH increase would mainly result from the mutual stabilization of the positively charged imidazolium ring and of the negatively charged FMN hydroquinone formed upon lactate oxidation. The pK_a increase of H373 would in turn favor lactate oxidation by facilitating: (i) proton transfer from lactate to H373 and (ii) electron transfer from lactate to the oxidised flavin, yielding the negatively charged FMN hydroquinone form. The pK_a increase of H373 in the reduced enzyme leading to a positively charged H373 has also been proposed to stabilize the FMN-N5-sulfite adduct, thus causing the very low dissociation constant of the complex (in the low μM range, Lederer, 1978).

In the Fcb2 active site the crystallographic Wat609 belongs to a S371-Wat-D282-H373 hydrogen-bonded chain (Figure 4.1.5), which is conserved in all the Fcb2 structures and in the structures of other Fcb2 family members. Interestingly, S371, which holds Wat609 in place, belongs to the SNHGXRQ sequence that is strictly conserved in the Fcb2 family of enzymes (Lederer et al, 2005).

To test the prediction made by the computational work that the reactivity of the active site base H373 may be modulated by the water molecule held in place by S371, the latter residue has been

replaced with an alanine in Fcb2. The S371A substitution should prevent the positioning of Wat609 with important consequences on the acid-base properties of H373, and therefore, on the catalytic properties of the enzyme.

4.2 METHODS

Production of Fcb2 and Fcb2-S371A as pDS derivatives *E. coli*

For the production of Fcb2-S371A as pDsb2 derivative, the *Bam*HI-*Bgl*II 1178 bp fragment of pETFcb2-S371A (see paragraph 4.3) was substituted for the corresponding fragment of pDSb2 (Black et al, 1989), available in our laboratory, yielding pDSb2-S371A. After sequencing (by PRIMM s.r.l., Milano), the pDSb2 and pDSb2-S371A were transformed into *E. coli* HB101 cells and the transformants were grown at 37°C in LB broth containing 100 μg/ml Ampicillin (Amp). A preculture was set up using freshly transformed cells. When OD_{600} reached a value of approximately 1, 0.5 ml aliquots were used to inoculate 2 l flasks containing 0.5 l LB-Amp. Cells were harvested after 16 h growth and stored frozen.

Protein purification

The full-length wild-type and S371A-Fcb2 were purified by adopting a procedure designed to minimize flavin loss. Cells (13 g) were resuspended in 30 mM (Na, K) phosphate buffer, pH 7.0, containing 1 mM EDTA, 20 mM DL-lactate, 0.5 mM phenylmethylsulfonyl fluoride (PMSF), 0.1 mM FMN (5 ml/g cells). 0.2 mg of lysozyme per gram of cells was added. The suspension was incubated on ice for 60 min under stirring, and sonicated (two 30 s and two 1 min cycles). After centrifugation at 27000 x g for 15 min at 4°C, the pellet was resuspended in 50 ml homogenization buffer and the sonication and centrifugation steps were repeated. The combined crude extracts were directly loaded on a hydroxyapatite column (HTP, BioRad, 2.6 x 13 cm, 60 ml) equilibrated with 30 mM (Na, K) phosphate buffer, pH 7.0, containing 1 mM EDTA (Buffer H). Weakly absorbed proteins were washed with 2 column volumes of buffer H containing 20 mM DL-lactate, 0.5 mM PMSF. The protein was eluted by applying a 30 to 600 mM (Na, K) phosphate gradient in buffer containing 20 mM DL-lactate, 0.5 mM PMSF in 800 ml. Fractions showing lactate dehydrogenase activity and electrophoretically homogeneous protein were pooled, concentrated by ultrafiltration in an Amicon cell equipped with a YM30 membrane. Aliquots were dialyzed against 100 mM (Na, K) phosphate buffer, pH 7.0, 1 mM EDTA, 20 mM DL-lactate and 0.1 mM FMN (Buffer I). The dialyzed enzyme samples were flash frozen in liquid nitrogen and stored at -80°C. Prior to each experiment, DL-lactate and FMN were removed by gel filtration on a Sephadex G-25 column (PD-10, prepacked disposable columns, GE Healthcare) equilibrated with 100 mM (Na, K) phosphate buffer, pH 7.0, 1 mM EDTA.

Activity assays and determination of the steady-state kinetic parameters.

Activity assays were carried out by monitoring ferricyanide (FeCN) reduction at 420 nm (ε = 1.04 mM^{-1} cm^{-1}) in assays mixture containing 100 mM (K) phosphate/NaOH buffer, pH 7.5, 1 mM EDTA, 5 mM L-lactate and 1 mM FeCN at 25°C in Cary219 or Cary100 (Varian) spectrophotometers. Apparent steady-state kinetic parameters were determined by measuring initial velocities of reactions that contained 5 mM L-lactate in the presence of varying FeCN concentration (0.1-2 mM), or 1 mM FeCN in the presence of varying L-lactate concentration (0.1-15 mM). To measure the primary kinetic isotope effects, L-[2-^{2}H]-lactate (lithium salt, Sigma) was used. The initial velocity values (v/E, expressed as µmol FeCN reduced per second per µmol FMN-containing enzyme) as a function of the varied substrate concentration (S) were fitted to the Michaelis-Menten equation (Eq. 1, paragraph 3.2) using the Grafit 4.0 software. The error associated with the determination of the primary kinetic isotope effects on k_{cat} ($^{D}k_{cat}$) and on k_{cat}/K_{lac} ($^{D}k_{cat}/K_{lac}$) was calculated from the values of k_{cat} and K_{lac} determined with the protio- and deutero-substrate applying the error propagation method as described in (Bevington, 1969).

pH profiles

The dependence of v/E on pH was determined by carrying out reactions in the presence of 1 mM FeCN and 5 mM L-lactate in the buffer system described by (Sobrado et al, 2001), namely, 50 mM Bis-Tris/HCl (pH 4.0-7.0), 150 mM Hepes/KOH (pH 7.0-8.5), or 50 mM ethanolamine/HCl (pH 8.5-9.5). To determine the pH dependence of k_{cat} and k_{cat}/K_{lac} in the acidic range, initial velocities of reactions that contained 1 mM FeCN and varying L-lactate were measured between pH 4.0 and 7.0. Equations 12 and 13 were used:

Eq. 12: $Y = Limit * 10^{(pH-pKa1)}/(10^{(2*pKa1-pKa2)} + 10^{(pH-pKa1)} + 1)$

Eq.13: $Y = Limit * 10^{(pH-pKa)}/(10^{(pH-pKa)} - 1)$

In Eq. 12 and 13, Limit is the pH independent value of the parameter (Y) being analyzed. In Eq. 12, pK_{a1} and pK_{a2} are the pK_a values of the groups that need to be unprotonated and protonated, respectively, for maximal value of the parameter. In Eq. 13, pK_a is that of the single group, the dissociation of which leads to an increase of the value of the parameter Y.

Determination of the dissociation constant of the enzyme-sulfite complex

The dissociation constant of the enzyme-sulfite complex was determined by titrating the enzyme (6-15 μM in terms of bound FMN) with sulfite solutions in 100 mM (Na, K) phosphate buffer, pH 7.0, 1 mM EDTA. After correction for dilution and calculation of the different spectra, which were consistent with the formation of a FMN-N(5)-sulfite adduct (Lederer, 1978), the fractional absorbance changes at 454 nm as a function of sulfite concentration were fitted to Eq. 14.

Eq. 14: $[(A_o–A_x)/(A_o–A_f)]*E = [(K_d+L+n) - \sqrt{((K_d+L+n)^2 – 4*L*n)}]/2$

Where: A_o, A_x and A_f are the absorbance values at 454 nm of the free enzyme, after addition of a given concentration of sulfite (L) and at the end of the titration, respectively; E is the total enzyme concentration; K_d is the dissociation constant of the enzyme-sulfite complex and n is the number of binding sites, which was found to be equal to 1.

Protein and cofactors quantification

The Bradford assay (Bradford, 1976) and the Bradford Reagent (Amresco) were used for protein quantification. A mass of 57 kDa was used to calculate the concentration of the full-length Fcb2 from the protein assay. For the quantification of the heme content of Fcb2 preparations, the absorbance spectrum of lactate-reduced samples was measured and reduced heme was quantified by using the absorbance value at 423 nm and the published extinction coefficient at this wavelength (ε_{423}, 183 mM^{-1} cm^{-1}, Labeyrie et al, 1978). To quantify bound FMN, the absorbance spectrum of protein samples that had been gel-filtered or dialyzed to remove excess FMN and DL-lactate was measured. 1-3 mM sodium sulfite (final concentration) was added from a 1 M solution. The difference between the spectrum of the free enzyme and that of the enzyme after reaction with sulfite was calculated and concentration of FMN was determined by using the calculated $\Delta\varepsilon$ at 454 nm of 10.5 mM^{-1} cm^{-1} (Lederer, 1978). The heme content of the enzyme solution could also be measured with the oxidized protein by using the published extinction coefficient at 413 nm (ε_{413} = 129.5 mM^{-1} cm^{-1}, Labeyrie et al, 1978).

4.3 RESULTS

Production of the pDS derivatives of Fcb2 and Fcb2-S371A variant and steady-state kinetic characterization

Previous work, aimed to the characterization of wild-type and S371A variant of FDH domain of Fcb2 from pET23b derivatives, led to the production of homogeneous Fcb2-FDH, with the correct FMN content. On the contrary, the S371A variant of FDH was obtained as a non-reconstitutable apoenzyme. Thus we turned our attention to the full-length Fcb2, which were produced in the wild-type and S371A variant from pET23b derivatives. The Fcb2 purified protein contained 0.9 mol FMN, but only 0.2 mol heme per mol protein. The turnover number at saturating lactate and FeCN was 151.5 ± 6.9 s^{-1}, K^{Lac} was 0.1 ± 0.01 mM and K_{FeCN} was 0.32 ± 0.005 (Table 4.3.1). Thus, the turnover was approximately 2-fold lower than the reported for Fcb2, while the K_m values for lactate and, especially, FeCN are somewhat between those reported for the holoenzyme (Cénas et al, 2007). A similar low heme content was observed upon purification of the Fcb2-S371A variant, however the FMN content was only 0.25 mol/mol protein. The K_m value for L-lactate was increased approximately 6-fold with respect to the wild-type protein and that for FeCN was decreased approximately 4-fold. The k_{cat} value was 6-7-fold lower that that measured with the wild-type enzyme even after correction for the flavin content of the preparation (Table 4.3.1).

Thus, we turned our attention on the production of Fcb2 and Fcb2-S371A as pDSb2 derivatives. pDSb2 is the plasmid most commonly used for the production of full-length Fcb2 and its variants. $pDSb_2$ and $pDSb_2$-S371A were transformed into *E. coli* HB101. High levels of wild-type and S371A-Fcb_2 were obtained by growing cells at 37°C for 16 h (Figure 4.3.1 panel A). 13 g of *E. coli* HB101 cells were homogenized by sonication and the crude extract was loaded on a hydroxyapatite column, equilibrated in buffer H. Weakly absorbed proteins were washed with 2 column volumes of buffer H containing 20 mM DL-lactate, 0.5 mM PMSF. The protein was eluted by applying a 30 to 600 mM (Na, K) phosphate gradient in buffer containing 20 mM DL-lactate, 0.5 mM PMSF (see Methods). The pooled fractions were concentrated and dialyzed against buffer I. The wild-type Fcb2 could be purified near to homogeneity (Figure 4.3.1 panel B). It presented a full-complement of heme, essentially stoichiometric amounts of FMN and had a specific activity value similar to those reported in the literature (Table 4.3.1; (Gondry et al, 1996; Cénas et al, 2007; Sobrado et al, 2001; Gondry et al, 2001; Sobrado and Fitzpatrick, 2003)). The Fcb2-S371A variant produced from pDSb2-S371A could also be purified by the same procedure (not shown). The resulting protein was similar to the wild-type with respect to heme content, but the flavin content was only 0.4 mol/mol enzyme. The k_{cat} value was approximately 10-fold lower than that of the wild-type (Table 4.3.1).

The K_m for lactate was essentially unchanged, but that of FeCN was significantly decreased leading to a low value that could not be precisely measured (Table 4.3.1). Thus, it appears that the S371A substitution affects flavin incorporation as found for other Fcb2 mutant forms, namely the R298K- (Mowat et al, 2000), H373- (Gaume et al, 1995), Y254L- and D282N-Fcb2 variants (Gondry et al, 1996; Gondry et al, 1995). For all these mutants it has been concluded that the lack of flavin insertion is due to an altered folding pathway during protein production in *E. coli*, but that the fraction of flavinylated enzyme is properly folded and can be studied to obtain information on the role of the mutated residue in Fcb2. In support of the fact that this may also be applied to Fcb2-S371A are the fact that the position of the absorbance maxima of the oxidized and reduced enzyme forms are similar (Figure 4.3.2), as the absorbance changes observed during sulfite titration (see below). For the Fcb2-S371A form, the 10-fold decrease of k_{cat} in the absence of significant changes of the K_m for L-lactate suggests that the rate of the enzyme reductive half-reaction is specifically lowered by the amino acid substitution.

Sulfite reactivity of FMN bound to Fcb2-S371A

Sulfite forms a stable covalent adduct with the N(5) position of Fcb2 FMN coenzyme, the formation of which can be monitored spectrophotometrically being associated to characteristic spectral changes (Lederer, 1978; Massey et al, 1969; Müller et al, 1969). As expected, sulfite titration of the wild-type Fcb2 led to spectral changes, comparable to those observed for the pET derivative (Figure 4.3.2 inset) and a calculated K_d (2.8 ± 0.1 μM, Table 4.3.1) similar to those found in literature (Lederer, 1978; Gondry et al, 1995). For the Fcb2-S371A form, the shape of the difference spectra (Figure 4.3.2) were also similar to those obtained with the wild-type enzyme, but the calculated K_d was approximately 10-fold higher (Table 4.3.1). In all these spectra, the 400-430 nm region is poorly defined due to the presence of the strong heme signal. This is especially troublesome with the S371A mutant where the heme:flavin ratio is approximately 2, with a ratio of the extinction coefficients of heme and flavin of at least 10 in favor of heme.

The observed increase of the K_d value of the FMN-sulfite complex could be explained with an altered conformation of the active site or by making the hypothesis that S371A substitution lowers the proton affinity of H373 by preventing the correct positioning of Wat609. Indeed, the stability of the flavin-sulfite adduct in Fcb2 has been ascribed to the positively charged H373 in the reduced enzyme (or in the enzyme sulfite complex) due to the mutual stabilization of the negative charge of the flavin introduced by sulfite addition.

Effect of the S371A substitution on the pH dependence of the steady-state kinetic parameters k_{cat} and k_{cat}/K_{lac}

The pH profile of the initial reaction velocity was firstly determined between pH 4.0 and 10 in the presence of fixed concentrations of L-lactate (5 mM) and FeCN (1 mM) (Figure 4.3.3 panel A and B, Table 4.3.2) for the wild-type and mutant forms produced from the pET and pDS-based plasmids. The initial velocity of the reaction of the wild-type Fcb2 forms obtained with the two plasmids exhibited a pH dependence similar to each other (Figure 4.3.3 panel A) and to the k_{cat} and k_{cat}/K_{Lac} profiles reported for Fcb2 under similar buffer and temperature conditions (Sobrado et al, 2001; Sobrado and Fitzpatrick, 2003) with apparent pK_a values of 5.2 ± 0.1 and 9.5 ± 0.1 (Figure 4.3.3, Table 4.3.2). The pH dependence of the initial velocities of the reaction catalyzed by the two Fcb2-S371A forms were also similar to each other and to the corresponding curve obtained with the wild-type species (Figure 4.3.3 panel B, Table 4.3.2). The pH profiles of the apparent k_{cat} and k_{cat}/K_{Lac} values were also determined between pH 4.0 and 7.0, for the wild-type Fcb2 form obtained with pDSb2 and the two Fcb2-S371A enzymes (Figure 4.3.3 panel C and D, Table 4.3.2). The pK_a governing the ascending limb of the k_{cat} and k_{cat}/K_{Lac} profiles of Fcb2 has been tentatively assigned to that of H373 (Lederer, 1991). Thus, it was of interest to test an effect of the S371A substitution on this part of the pH profile. For Fcb2, the k_{cat} and k_{cat}/K_{Lac} values increased with the dissociation of a group with pK_a of 4.4 ± 0.1 and 4.8 ± 0.1, respectively (Figure 4.3.3 panel C). The pH profiles obtained with the two Fcb2-S371A variants were similar to each other and the calculated pK_a values and the calculated pK_a values from the k_{cat} and k_{cat}/K_{Lac} profiles were 4.7 ± 0.1 and 5.0 ± 0.2, respectively (Table 4.3.2). Thus, taking into account the error associated with these determinations, no evidence of the effect of the S371A substitution on the pK_a value governing the ascending limb of the k_{cat} and k_{cat}/K_{Lac} profiles could be obtained. This lack of effect does not contradict the prediction made on the basis of the simulations that the water molecule held in place by S371 modulates the proton affinity of H373. Rather, it may suggest that Wat609 may influence the protonation state of H373 in the reduced enzyme and/or that the pK_a governing the ascending limb of the V and V/K_{Lac} profiles of Fcb2 is not that of H373 in the oxidized enzyme. Both these cases are possible. The pK_a was assigned to that of H373 on the basis of the observation that H373 is the only ionizable group in the active site that must be dissociated for catalysis and which may have a pK_a in the observed range in the oxidized enzyme (Lederer, 1991). However, it was not ruled out that the observed value is not that of a microscopic pK_a (Lederer, 1991). Against the assignment of the observed pK_a to that of H373 in the oxidized enzyme (or at least its insensitivity to the charge on the neighbouring D282) is the fact that the pH profile of V exhibited by the D282N-Fcb2 variant was similar to that of the wild-type enzyme (Cénas et al, 2007). D282 is the negatively charged

residue adjacent to H373, which should stabilize the protonated, positively charged, H373 form. However, the D282N substitution lowered the pK_a of the active site base in the reduced enzyme by 1.5 units (Gondry et al, 1996).

Effect of the S371A substitution on the deuterium primary kinetic isotope effects

The primary kinetic isotope effects on k_{cat} and k_{cat}/K_{Lac} were also determined in the presence of 1 mM FeCN at pH 7.5 (Figure 4.3.4, Table 4.3.3) for both the wild-type and the Fcb2-S371A forms produced with the pDS derivatives. For Fcb2, the magnitude of the kinetic isotope effects provides valuable information on the changes of the rate of lactate oxidation during the enzyme reductive half reaction.

For Fcb2-S371A the calculated $^{D}k_{cat}$ and $^{D}k_{cat}/K_{Lac}$ were 6.1 ± 0.1 and 6.0 ± 0.4, respectively, thus greater than the corresponding values measured by us with the wild-type enzyme ($^{D}k_{cat}$, 4.8 ± 0.1 and $^{D}k_{cat}/K_{Lac}$, 4.1 ± 0.3; Table 4.3.3) and found in the literature. The similarity of $^{D}k_{cat}$ and $^{D}k_{cat}/K_{Lac}$ supports the concept that also with Fcb2-S371A the K_{Lac} value measured under steady-state conditions equals the dissociation constant of the enzyme-lactate complex (Gondry et al, 1996; Klinman and Matthews, 1985), and confirms that the mutation has no effect on lactate binding to the enzyme. The higher values of the primary kinetic isotope effects for the Fcb2-S371A variant as compared to those of the wild-type enzyme clearly indicate that the amino acid substitution has a specific effect on the flavin reduction rate, which becomes more limiting the overall turnover. This effect would be consistent with a lower stabilization of the transition state due to the destabilization of the positively charge on H373 in the absence of the water molecule.

4.4 CONCLUSIONS

Flavocytochrome b_2 (L-lactate:cytochrome c oxidoreductase, Fcb2) is the structural and mechanistic prototype of a family of α-hydroxyacid dehydrogenases that are believed to share a common mechanism for the oxidation of the α-hydroxy acid substrate in the enzyme reductive half reaction. Recent first principles molecular dynamics studies on active-site models of Fcb2, in complex with the substrate, were carried out to contribute towards establishing the mechanism of the enzyme-catalyzed L-lactate oxidation, a still debated issue (Tabacchi et al, 2009). These simulations highlighted the relevance of an active site water molecule and suggested a role of the conserved S371 side chain hydroxyl group in positioning this water molecule close to the catalytically relevant D282-H373 couple. This residue, which belongs to the SNHGXRQ sequence characteristic of the Fcb2 family of enzymes, in fact is connected to H373 through a S371-Wat609-D282-H373 hydrogen bonded chain.

The role of S371 of Fcb2 has been studied for the first time by generating the S371A enzyme variant. Attempts to produce the isolated FDH domain carrying the S371A substitution led to the obtainment of the apoprotein form suggesting that the mutation interferes with protein folding. Production of wild-type Fcb2 in *E. coli* from a pET23b derivative led to a protein with the full FMN complement but only 0.2 mol heme/mol enzyme. Its kinetic properties were in between those of the holoenzyme and the isolated FDH domain. The S371A variant of full length Fcb2 produced from pET23b had a heme content as low as that of the wild-type form, but also a low FMN content confirming the effect of the S371A substitution on the protein folding pathway.

The wild-type Fcb2 could also be produced in *E. coli* as pDS derivative. It presented a full-complement of heme and stechiometric amounts of FMN. The Fcb2-S371A variant was similar to the wild-type with respect to heme content, but the flavin content was only 0.4 mol/mol enzyme. Thus, several lines of evidence indicate that the invariant S371 residue plays a role during enzyme folding. This observation finds precedents in other site directed mutants of Fcb2 (Mowat et al, 2004; Gondry et al, 1995) where it was concluded that the flavinylated enzyme is properly folded and may be used to gain information on Fcb2 properties. That this is likely to be true also for the S371A-Fcb2 variant are: (i) the chromatographic behavior and protein stability, which are not significantly changed with respect to the wild-type enzyme; (ii) the similar difference absorbance spectra upon sulfite titration (Figure 4.3.2); (iii) the similar K_M value for L-lactate (Table 4.3.1), and (iv) the similar pH dependence of v/E, k_{cat} and k_{cat}/K_M (Figure 4.3.3). The S371A substitution appears to specifically affect: (i) k_{cat}, which decreases by one order of magnitude, due to a lower rate of the enzyme reductive half reaction, as shown by the increase of the magnitude of the observed primary kinetic isotope effects (Table 4.3.3), and (ii) the K_d of the enzyme-sulfite adduct,

which increases approximately 10-fold (Table 4.3.1). The observed changes in the properties of the S371A-Fcb2 may indicate an overall altered geometry of the active site that specifically affects the flavin reactivity by altering the tendency to form the flavin N(5)-sulfite adduct and the electron transfer from lactate. Among the factors that have been proposed to greatly stabilize the negatively charged reduced FMN and FMN-sulfite adduct is His373, which becomes readily protonated on flavin on flavin reduction or formation of the FMN-sulfite adduct. Therefore, these results are also fully consistent with the hypothesis formulated in the basis of simulations (Tabacchi et al, 2005, Tabacchi et al, 2007; Tabacchi et al, 2009), namely that S371 ensures the correct positioning of a water molecule (Wat 609 in 1fcb structure), which acts as a hydrogen bond donor to D282. This water molecule contributes to maintain H373 in the protonated state in the reduced enzyme by preventing proton transfer to D282 to yield neutral H373 and neutral D282. Therefore, the positively charged H373 can stabilize the transition state and the enzyme-sulfite adduct. The S371A substitution could prevent (or alter) lowering the proton affinity of H373. In such a case both FMN reduction would be lowered and the affinity of the FMN-sulfite adduct would be weakened without altering lactate binding as we observed. Overall, these results show the importance of S371 for the correct folding pathway of Fcb2 flavodehydrogenase domain, in agreement with previous studied that led to substitution of other active site residues. The observed effects on the reactivity of the flavin can be equally well explained by an overall altered geometry of the active site and by a specific effect of the S371A substitution as it emerged from the computational approach. In the latter case these results show how active site residues not in direct contact with the reaction center may be able to control and tune the physico-chemical properties of key catalytic residues, thus playing a fundamental role in enzymatic catalysis. Furthermore, these results highlight the importance of computational approaches to reveal potential, unexpected, functions of active site residues, thus guiding experiments.

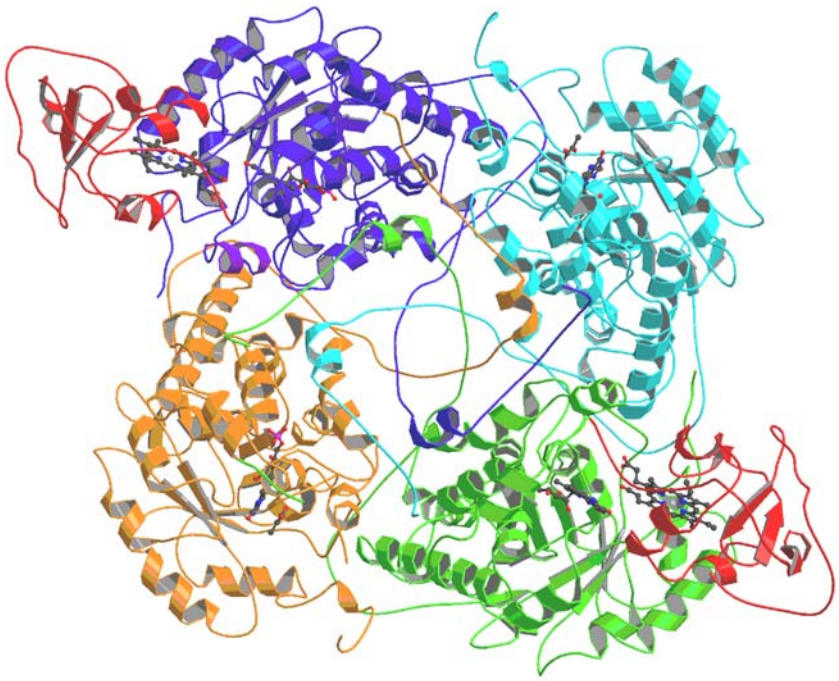

Figure 4.1.1: Crystal structure of Fcb2 from *S. cerevisiae* in the tetrameric form in the presence of pyruvate (Xia et al, 1990; PDB code 1fcb). Only two N-terminal protein domain containing heme b_2 (red) are shown. FDH domains are in contact through their C-terminal region. Cofactors and pyruvate moleculs are in ball-and-stick.

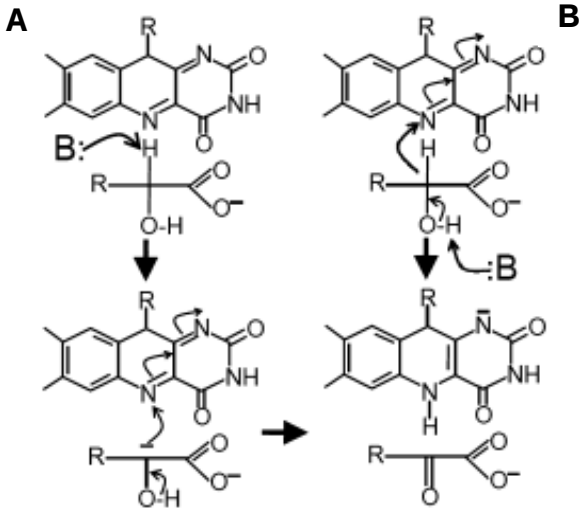

Schema 1: (A) The carbanion or proton abstraction (PA) mechanism. (B) The hydride transfer (HT) mechanism. The carbanion could evolve via either formation of a covalent intermediate at N5 or two consecutive single electron transfer steps. The active-site base (B) is only shown in the first part of each scheme.

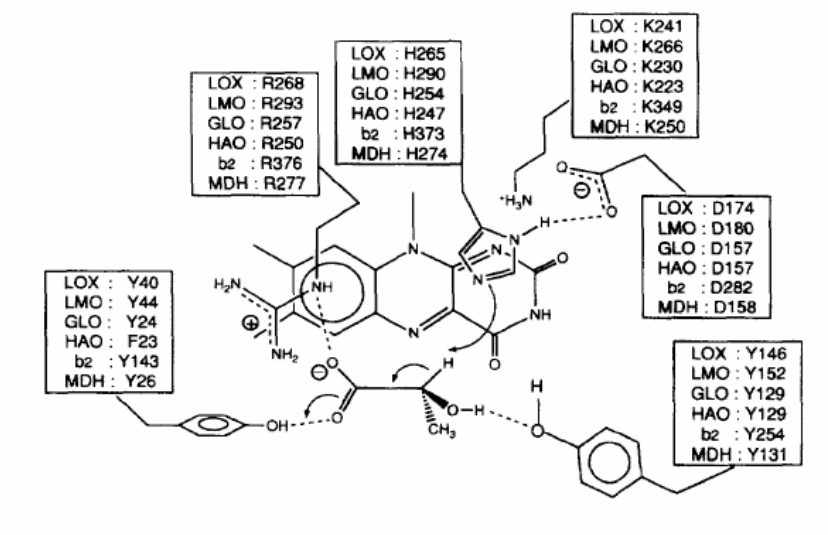

Figure 4.1.2: Conserved residues for the enzymes of the Fcb2 family. LOX: L-lactate oxidase; LMO: L-lactate monoxygenase; GLO: glicolate oxidase; HAO: long chain α-hydroxy acid oxidase; b_2: flavocytochrome b_2; MDH: mandelate dehydrogenase (Maeda-Yorita et al, 1995).

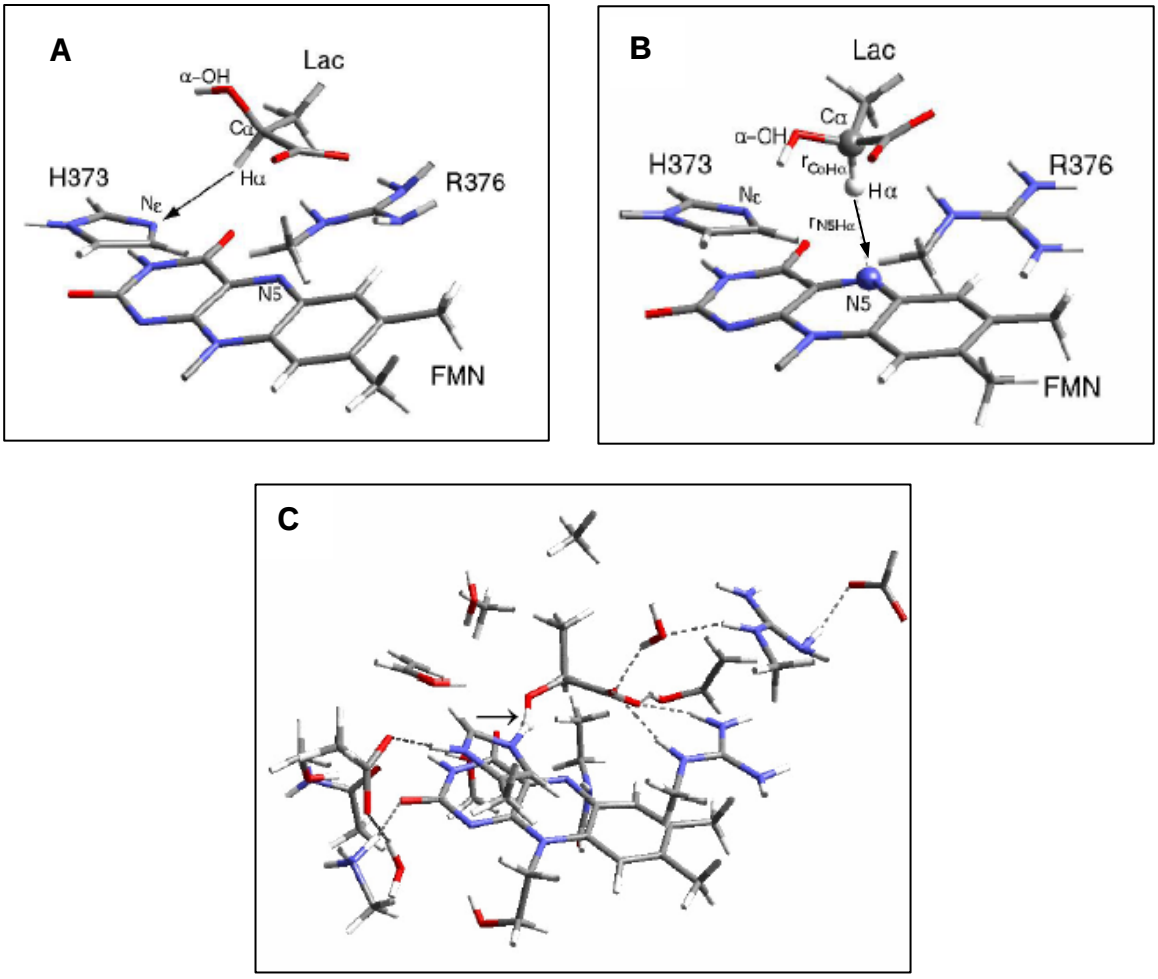

Figure 4.1.3: L-lactate in the PA-prone orientation (panel A) and in the HT-prone orientation (panel B). The arrows indicate the postulated Hα to H373 transfer (panel A) or to N_5 (panel B). Panel C: Representation of the minimum energy structure of the Fcb2 active site model in complex with the L-lactate obtained with computational simulations. The arrow indicates the sharing of Hα between substrate and H373 residue sometimes observed in the simulations.

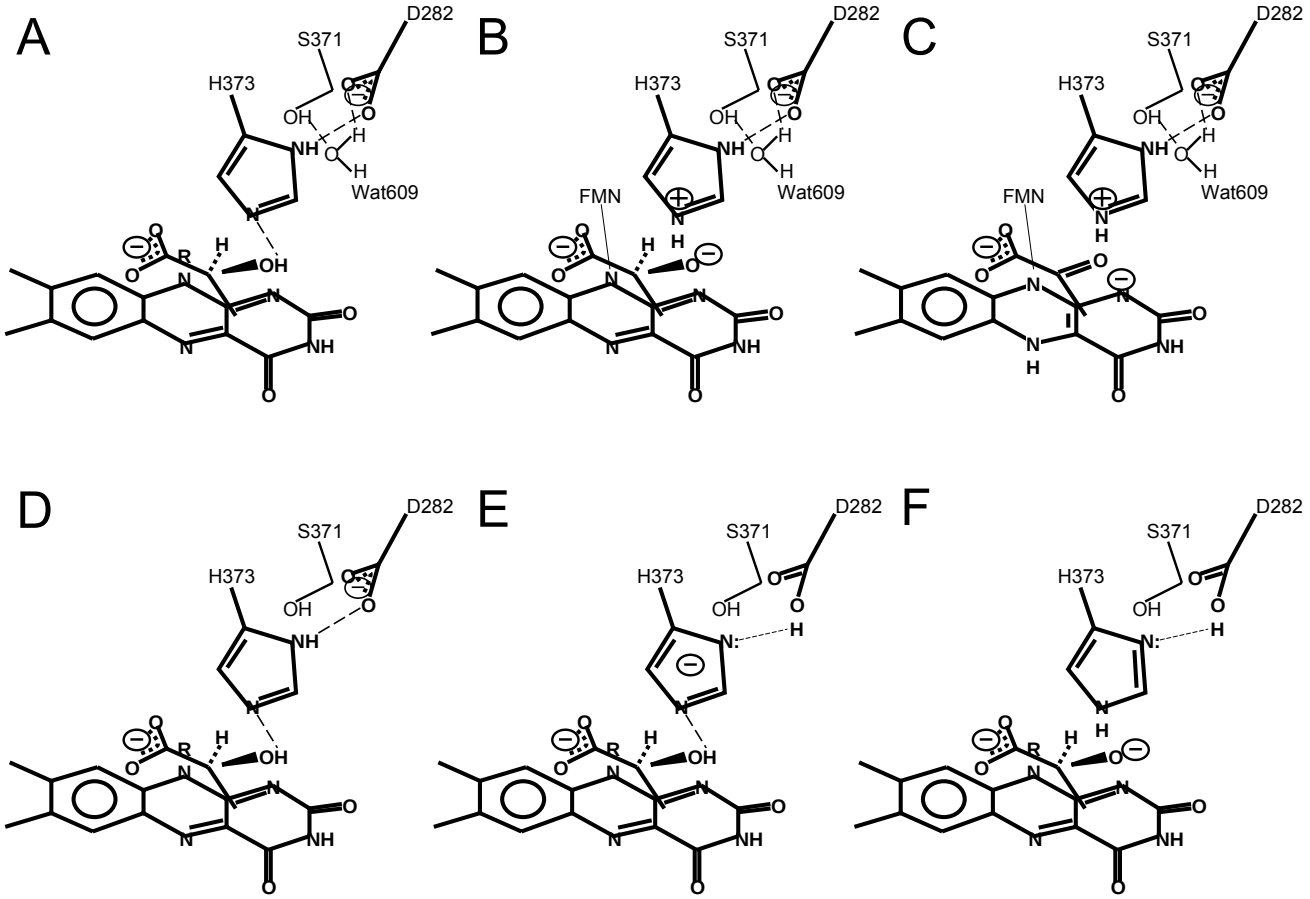

Figure 4.1.4 Scheme of the effect of Wat609 on the acidity of H373 in Fcb2 active site model. Panels A-C depict the ionization state and hydrogen bonding interactions of key active site residues in the Fcb2 active site modeled in (Tabacchi et al, 2009). Panel A: the Michaelis complex; panel B: just before the transitions state; panel C: at the end of the reaction. Panels D-F show the ionization state and hydrogen bonding interactions of the active site residues observed during molecular dynamics simulations of the Fcb2 active site model omitting Wat609 (Tabacchi et al, 2005 and 2009). Panel D: starting configuration of the Fcb2 active site model; panel E: during molecular dynamics simulations of the Michaelis complex at 300 K, proton transfer events from H373 Nδ to D282 carboxylate O(2) were observed leading to a negatively charged imidazolate ion and neutral D282 carboxyl group; panel F: during a series of constrained molecular dynamics done to test the reactivity of the Fcb2 active site model, transfer of the lactate αOH hydrogen (as a proton) to H373 Nε (forming a lactate alkoxide intermediate) concomitant with transfer of the H373 Nδ hydrogen (as a proton) to D282 was observed. For graphical purposes lactate is arbitrarily oriented, Ser371 and Wat 609 are drawn with thin lines to indicate that they are below D282. Potential hydrogen bonds are indicated with dashed lines.

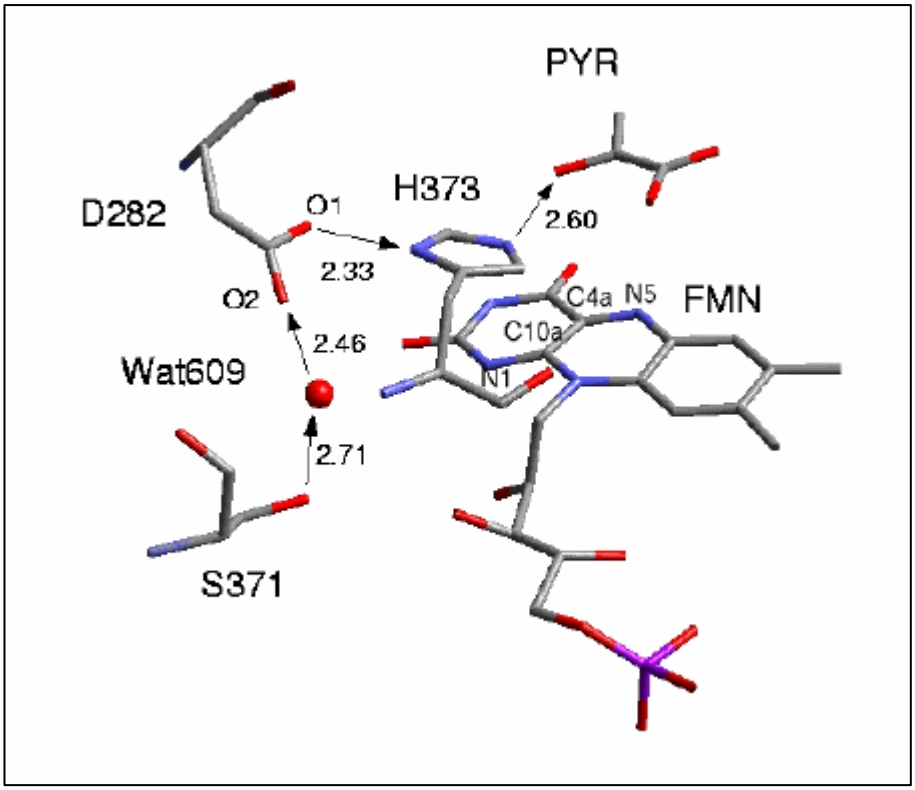

Figure 4.1.5: S371-W609-D282-H373-pyruvate-FMN hydrogen-bonded chain. Distances are in Å. The arrows indicate hydrogen bonds from the donor to the acceptor atom. PYR: pyruvate

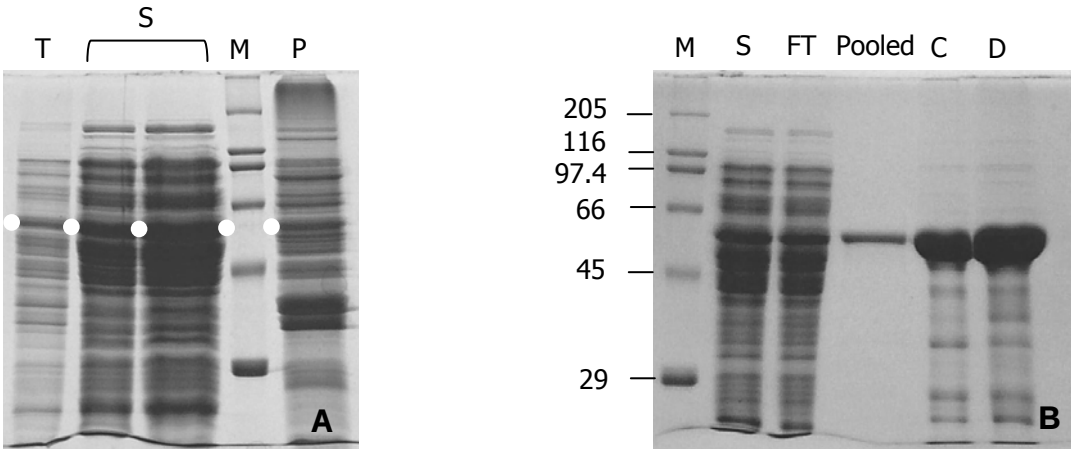

Figure 4.3.1: Fcb2 expression in *E. coli* HB101 cells and its purification on hydroxyapatite resin. Panel A: *E. coli* HB101 cells transformed with pDSb2 were grown in LB supplemented with 0.1 mM ampicillin at 37°C and expression was induced with 0.1 mM IPTG at an OD_{600} value of approximately 1. Cells were harvested after 16 h. An aliquot was used to prepare the total extract (T). The cells were homogenized to obtain the crude extract containing soluble proteins (S, 90 and 180 µg) and the pellet (P). White dots indicate the position of Fcb2 (57 kDa). Panel B: Crude extract of cells containing Fcb2 (S) was loaded on a hydroxyapatite column equilibrated in 30 mM (Na, K) phosphate buffer, pH 7.0, containing 1 mM EDTA. Non bound proteins were collected with the flow-through (FT). Fractions eluted with gradient of phosphate containing Fcb2 were pooled (Pooled, 6.3 µg), concentrated (C, 35 µg) and dialyzed against 100 mM (Na, K) phosphate buffer, pH 7.0, 1 mM EDTA, 20 mM DL-lactate and 0.1 mM FMN (D; 45 µg).

Table 4.3.1: Steady-state kinetic parameters of the lactate dehydrogenation reaction catalysed by Fcb2 and S371A-Fcb2 in the presence of FeCN. Assays were carried out at 25°C in 100 mM potassium phosphate buffer, pH 7.5, 1 mM EDTA in the presence of the indicated substrate concentration or concentration range. Enzyme concentration is expressed per bound FMN. The dissociation constant of the enzyme-sulfite complex was determined by spectrophotometric titrations of the enzyme forms. Fcb2 and Fcb2-S371A were expressed as pET23b derivatives (pET plasmid) and pDS derivatives (pDS plasmid). n.d.: not determined.

Enzyme	Plasmid	L-lactate, mM	FeCN, mM	K_{lac}, mM	K_{FeCN}, mM	k_{cat}, s^{-1}	$K_{sulfite}$, µM
Fcb2	pET	0.1-15	1	0.10 ± 0.01		128.0 ± 1.5	n.d.
		5	0.05-2		0.32 ± 0.005	151.5 ± 6.9	
	pDS	0.1-15	1	0.30 ± 0.03		394.8 ± 6.8	2.8 ± 0.1
		5	0.02-2		0.02 ± 0.002	364.6 ± 4.5	
S371A-Fcb2	pET	0.1-15	1	0.57 ± 0.03		22.6 ± 0.2	17.6 ± 1.7
		5	0.02-2		0.09 ± 0.014	22.7 ± 0.6	
	pDS	0.1-15	1	0.40 ± 0.02		29.2 ± 0.2	25.0 ± 1.5
		5	0.02-2		0.006 ± 0.001	26.8 ± 0.2	

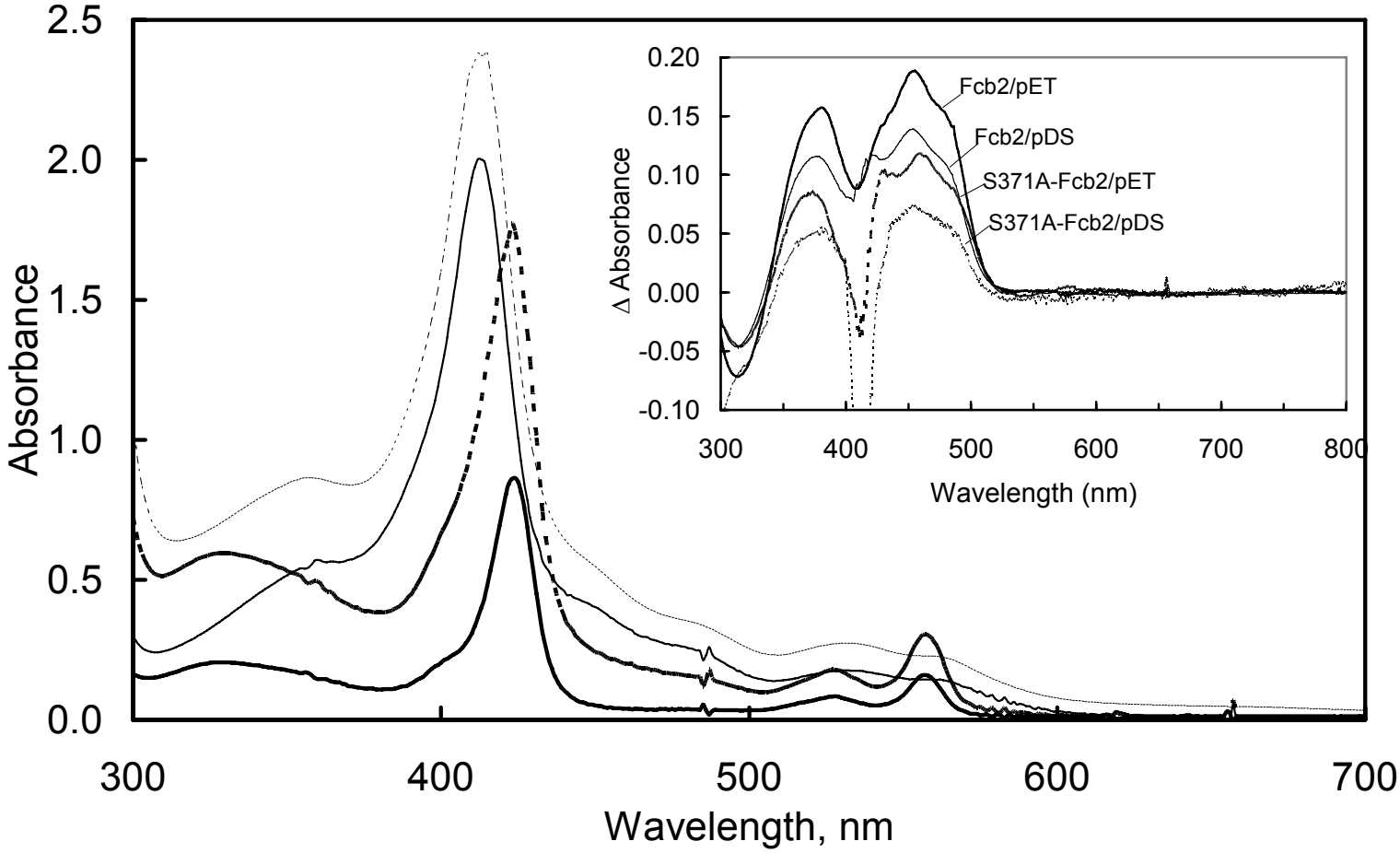

Figure 4.3.2: Spectra of Fcb2 (continuous lines) and Fcb2-S371A (dotted lines) produced from the pDS derivative in the reduced (thick lines) and oxidized (thin lines) forms. The wild-type and the S371A variant spectra in the reduced and oxidized forms result very similar, with identical maxima absorption peaks (328 nm, 424 nm, 527 nm and 557 nm for the reduced form; 359 nm, 412 nm, 447 nm, 480 nm, 531 nm and 562 nm for the oxidized one). Inset: Absorbance changes brought about by the formation of the FMN N(5)-sulfite adduct. The differences between the spectra of the free enzyme forms and those obtained after addition of 2 mM sulfite have been calculated. Thick continuous line: 20 μM Fcb2 produced from the pET-derivative (heme concentration: 4 μM, calculated FMN concentration: 17 μM); thick dotted line: 44 μM S371A-Fcb2 from the pET-derivative (heme, 9 μM; FMN, 11.2 μM); thin line: 19 μM Fcb2 from pDSb2 (heme, 15 μM; FMN, 13.4 μM); thin dotted line: 17.4 μM S371A-Fcb2 from pDSb2/S371A (heme, 14 μM; FMN, 7 μM).

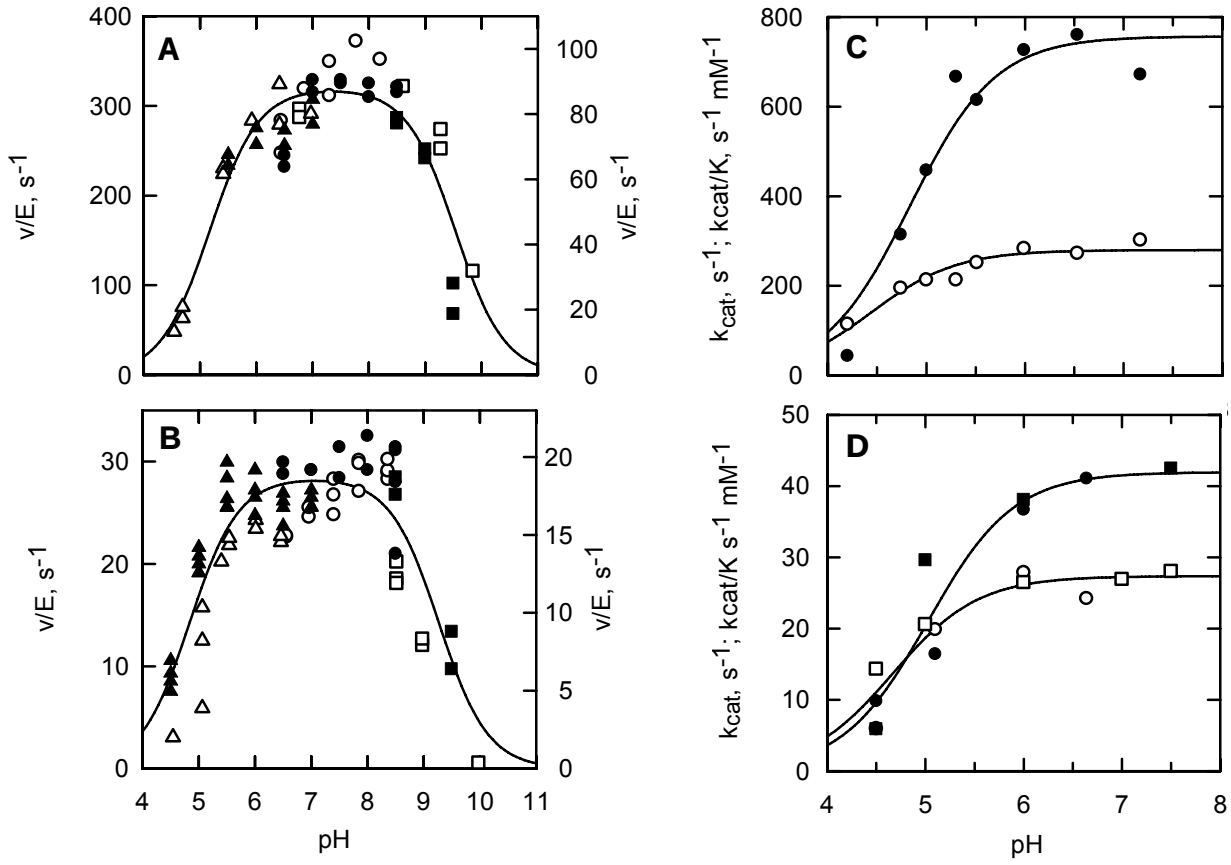

Figure 4.3.3: pH dependence of the L-lactate dehydrogenation reaction catalyzed by Fcb2 and Fcb2-S371A. Panels A and B: initial velocities (v/E) were determined at 25°C in the presence of 5 mM L-lactate and 1 mM FeCN with the buffers system of (Sobrado et al, 2001): 50 mM Bis-Tris/HCl (triangles), 150 mM Hepes/KOH (circles) and 50 mM ethanolamine/HCl (squares). Panel A: Fcb2 produced from pDSb2 (open symbols, left axis) and from pETFcb2 (closed symbols, right axis). Panel B: Fcb2-S371A produced from pDSb2-S371A (open symbols, left axis) and pETFcb2-S371A (close symbols, right axis). Panel C: pH dependence of k_{cat} (open circles) and k_{cat}/K_{Lac} (closed circles) of Fcb2 produced from pDSb2. Panel D: pH dependence of k_{cat} (open symbols) and k_{cat}/K_{Lac} (closed symbols) of the Fcb2-S371A produced from pDSb2-S371A (circles) or pETFcb2-S371A (squares). The curves show the fit of the data with Eq. 12 (Panel A and B) and Eq. 13 (Panel C and D) and the calculated parameters are reported in Table 4.3.2.

Table 4.3.2: Summary of the pKa values calculated from the pH dependence of the reaction catalyzed by Fcb2 and the S371A variant produced from the pDS derivatives. The data shown in Figure 4.3.3 were fitted with Eq. 12 or Eq. 13 as described in the figure legend.

Enzyme	Parameter	pK_{a1}	pK_a2	Limit (s^{-1} or $mM^{-1}s^{-1}$)
Fcb_2	v/E	5.2 ± 0.1	9.5 ± 0.1	320.0 ± 8.0
	k_{cat}	4.4 ± 0.1		279.9 ± 9.6
	k_{cat}/K_{lac}	4.8 ± 0.1		756.7 ± 41.5
Fcb_2-S371A	v/E	4.8 ± 0.1	9.3 ± 0.1	28.5 ± 0.7
	k_{cat}	4.7 ± 0.1		27.4 ± 1.3
	k_{cat}/K_{lac}	5.0 ± 0.1		42.0 ± 2.9

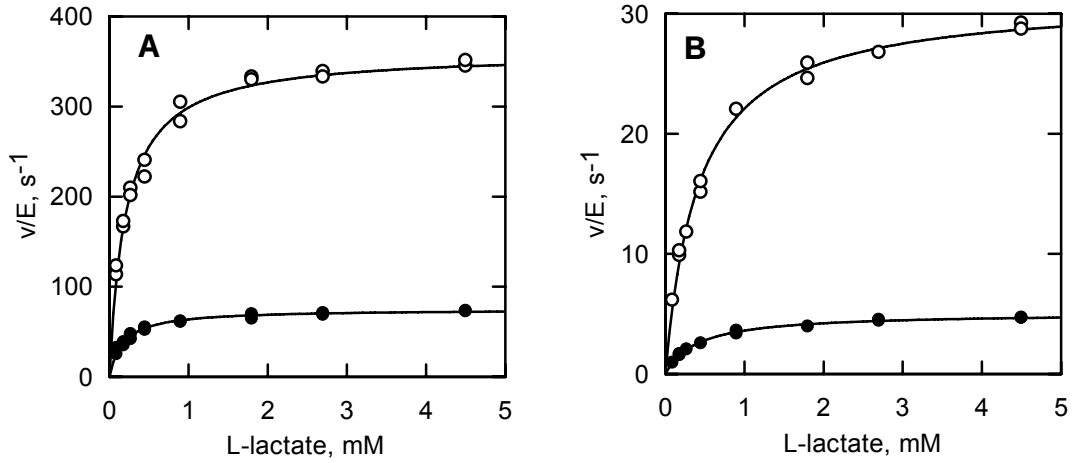

Figure 4.3.4: Determination of the primary kinetic isotope effect on lactate oxidation catalyzed by Fcb2 and Fcb2-S371A. Dependence of the initial reaction velocity of reactions catalyzed by Fcb2 (from pDSb2, Panel A) and by Fcb2-S371A (from pDSb2-S371A, Panel B) at 25°C in 100 mM potassium phosphate buffer, pH 7.5, in the presence of 1 mM FeCN and varying concentrations of L-[2-^{1}H]-lactate (open symbols) or L-[2-^{2}H]-lactate (closed symbols). The curves are the best fit of the data to the Michaelis Menten equations (see Table 4.3.3 for the calculated parameters).

Table 4.3.3: Summary of the primary kinetic isotope effects exhibited by the wild-type and the S371A forms of Fcb2. Initial velocities were measured at 25°C in 100 mM potassium phosphate, pH 7.5, in the presence of 1 mM FeCN and varying L-[2-^{1}H] or L-[2-^{2}H]-lactate using Fcb2 and S371A-Fcb2 expressed from the corresponding pDS derivative (see Figure 4.3.4).

Enzyme	Substrate	k_{cat}, s^{-1}	K_{Lac}, mM	k_{cat}/K_{Lac}, $mM^{-1}\,s^{-1}$	$^{D}k_{cat}$	$^{D}k_{cat}/K_{Lac}$
Fcb2	L-[2-^{1}H]-lactate	360.5 ± 4.0	0.21 ± 0.01	1716.5 ± 84.0		
	L-[2-^{2}H]-lactate	74.9 ± 1.0	0.18 ± 0.01	416.2 ± 23.8	4.8 ± 0.1	4.1 ± 0.3
Fcb2-S371A	L-[2-^{1}H]-lactate	31.4 ± 0.5	0.42 ± 0.02	74.6 ± 3.7		
	L-[2-^{2}H]-lactate	5.1 ± 0.1	0.41 ± 0.02	12.4 ± 0.6	6.2 ± 0.1	6.0 ± 0.4

REFERENCES

Aliverti, A., B. Curti, and M.A. Vanoni, *Identifying and quantitating FAD and FMN in simple and in iron-sulfur-containing flavoproteins.* Methods Mol Biol, 1999. **131**: p. 9-23.

Ashida, S., et al., *Expression of novel molecules, MICAL2-PV (MICAL2 prostate cancer variants), increases with high Gleason score and prostate cancer progression.* Clin Cancer Res, 2006. **12**(9): p. 2767-73.

Ballou, D.P., B. Entsch, and L.J. Cole, *Dynamics involved in catalysis by single-component and two-component flavin-dependent aromatic hydroxylases.* Biochem Biophys Res Commun, 2005. **338**(1): p. 590-8.

Balme, A. and F. Lederer, *On the rate of proton exchange with solvent of the catalytic histidine in flavocytochrome b2 (yeast L-lactate dehydrogenase).* Protein Sci, 1994. **3**(1): p. 109-17.

Battista, M.C., et al., *24-dehydrocholesterol reductase/seladin-1: a key protein differentially involved in adrenocorticotropin effects observed in human and rat adrenal cortex.* Endocrinology, 2009. **150**(9): p. 4180-90.

Battista, M.C., et al., *Seladin-1 expression in rat adrenal gland: effect of adrenocorticotropic hormone treatment.* J Endocrinol, 2007. **192**(1): p. 53-66.

Benvenuti, S., et al., *Estrogen and selective estrogen receptor modulators exert neuroprotective effects and stimulate the expression of selective Alzheimer's disease indicator-1, a recently discovered antiapoptotic gene, in human neuroblast long-term cell cultures.* J Clin Endocrinol Metab, 2005. **90**(3): p. 1775-82.

Benvenuti, S., et al., *Neuronal differentiation of human mesenchymal stem cells: changes in the expression of the Alzheimer's disease-related gene seladin-1.* Exp Cell Res, 2006. **312**(13): p. 2592-604.

Beuchle, D., et al., *Drosophila MICAL regulates myofilament organization and synaptic structure.* Mech Dev, 2007. **124**(5): p. 390-406.

Bevington, P.R., *Data reduction and error analysis for the physical sciences*. 1969, New York: McGraw-Hill.

Black, M.T., et al., *High-level expression of fully active yeast flavocytochrome b2 in Escherichia coli.* Biochem J, 1989. **258**(1): p. 255-9.

Blacklow, S.C., et al., *Triosephosphate isomerase catalysis is diffusion controlled. Appendix: Analysis of triose phosphate equilibria in aqueous solution by 31P NMR.* Biochemistry, 1988. **27**(4): p. 1158-67.

Bradford, M.M., *A rapid and sensitive method for the quantitation of microgram quantities of protein utilizing the principle of protein-dye binding.* Anal Biochem, 1976. **72**: p. 248-54.

Brouwer, A.C. and J.F. Kirsch, *Investigation of diffusion-limited rates of chymotrypsin reactions by viscosity variation.* Biochemistry, 1982. **21**(6): p. 1302-7.

Butt, T.R., et al., *SUMO fusion technology for difficult-to-express proteins.* Protein Expr Purif, 2005. **43**(1): p. 1-9.

Caldwell, S.R., et al., *Limits of diffusion in the hydrolysis of substrates by the phosphotriesterase from Pseudomonas diminuta.* Biochemistry, 1991. **30**(30): p. 7438-44.

Cenas, N., et al., *Potentiometric and further kinetic characterization of the flavin-binding domain of Saccharomyces cerevisiae flavocytochrome b2. Inhibition by anions binding in the active site.* Biochemistry, 2007. **46**(15): p. 4661-70.

Choe, S., et al., *The Arabidopsis dwarf1 mutant is defective in the conversion of 24-methylenecholesterol to campesterol in brassinosteroid biosynthesis.* Plant Physiol, 1999. **119**(3): p. 897-907.

Cole et al, *Removal of a methyl group causes global changes in p-Hydroxybenzoate hydroxylase.* Biochemistry, 2005**. 44**, 8047-58.

Cunane, L.M., et al., *Crystal structure analysis of recombinant rat kidney long chain hydroxy acid oxidase.* Biochemistry, 2005. **44**(5): p. 1521-31.

Cunane, L.M., et al., *Crystallographic study of the recombinant flavin-binding domain of Baker's yeast flavocytochrome b(2): comparison with the intact wild-type enzyme.* Biochemistry, 2002. **41**(13): p. 4264-72.

Current Protocols in Molecular Biology ed. F.M. Ausubel, Brent, R., Kingston, R.E., Moore, D.D., Seidman, J.G., Smith ,J.A., and Struhl K. 2005, Hoboken, NJ.: John Wiley & Sons, Inc. .

Data for biochemical research ed R.M.C. Dawson, D.C. Elliott, W.H. Elliott, K.M. Jones, 1969, Clarendon Press, Oxford.

Di Stasi, D., et al., *DHCR24 gene expression is upregulated in melanoma metastases and associated to resistance to oxidative stress-induced apoptosis.* Int J Cancer, 2005. **115**(2): p. 224-30.

Entsch, B., L.J. Cole, and D.P. Ballou, *Protein dynamics and electrostatics in the function of p-hydroxybenzoate hydroxylase.* Arch Biochem Biophys, 2005. **433**(1): p. 297-311.

Eser, B.E. and P.F. Fitzpatrick, *Measurement of intrinsic rate constants in the tyrosine hydroxylase reaction.* Biochemistry, 2010. **49**(3): p. 645-52.

Fassbender, K., et al., *Simvastatin strongly reduces levels of Alzheimer's disease beta -amyloid peptides Abeta 42 and Abeta 40 in vitro and in vivo.* Proc Natl Acad Sci U S A, 2001. **98**(10): p. 5856-61.

Fischer, J., T. Weide, and A. Barnekow, *The MICAL proteins and rab1: a possible link to the cytoskeleton?* Biochem Biophys Res Commun, 2005. **328**(2): p. 415-23.

Fitzpatrick, P.F., *Carbanion versus hydride transfer mechanisms in flavoprotein-catalyzed dehydrogenations.* Bioorg Chem, 2004. **32**(3): p. 125-39.

Fitzpatrick, P.F., *Substrate dehydrogenation by flavoproteins.* Acc Chem Res, 2001. **34**(4): p. 299-307.

Fraaije, M.W. and Mattevi, A. *Flavoenzymes: diverse catalysts with recurrent features.* Trends Biochem Sci, 2000. **25**(3): p. 126-32.

Fraaije, M.W., et al., *A novel oxidoreductase family sharing a conserved FAD-binding domain.* Trends Biochem Sci, 1998. **23**(6): p. 206-7.

Ghisla, S. and V. Massey, *Mechanisms of flavoprotein-catalyzed reactions.* Eur J Biochem, 1989. **181**(1): p. 1-17.

Ghisla, S., et al., *On the structure of flavin-oxygen intermediates involved in enzymatic reactions.* Eur J Biochem, 1977. **76**(1): p. 139-48.

Gondry, M. and F. Lederer, *Functional properties of the histidine-aspartate ion pair of flavocytochrome b2 (L-lactate dehydrogenase): substitution of Asp282 with asparagine.* Biochemistry, 1996. **35**(26): p. 8587-94.

Gondry, M., et al., *On the lack of coordination between protein folding and flavin insertion in Escherichia coli for flavocytochrome b2 mutant forms Y254L and D282N.* Protein Sci, 1995. **4**(5): p. 925-35.

Gondry, M., et al., *The catalytic role of tyrosine 254 in flavocytochrome b2 (L-lactate dehydrogenase from baker's yeast). Comparison between the Y254F and Y254L mutant proteins.* Eur J Biochem, 2001. **268**(18): p. 4918-27

Greeve, I., et al., *The human DIMINUTO/DWARF1 homolog seladin-1 confers resistance to Alzheimer's disease-associated neurodegeneration and oxidative stress.* J Neurosci, 2000. **20**(19): p. 7345-52.

Hung, R.J., et al., *Mical links semaphorins to F-actin disassembly.* Nature, 2010. **463**(7282): p. 823-7.

Joosten, V. and W.J. van Berkel, *Flavoenzymes.* Curr Opin Chem Biol, 2007. **11**(2): p. 195-202.

Klahre, U., et al., *The Arabidopsis DIMINUTO/DWARF1 gene encodes a protein involved in steroid synthesis.* Plant Cell, 1998. **10**(10): p. 1677-90.

Klinman, J.P. and Matthews, R.G., *Calculation of substrate dissociation constants from steady-state isotope effects in enzyme-catalyzed reactions.* J Am Chme Soc, 1985. **107** 1058-1060

Kolk, S.M. and R.J. Pasterkamp, *MICAL flavoprotein monooxygenases: structure, function and role in semaphorin signaling.* Adv Exp Med Biol, 2007. **600**: p. 38-51.

Labeyrie, F., A. Baudras, and F. Lederer, *Flavocytochrome b 2 or L-lactate cytochrome c reductase from yeast.* Methods Enzymol, 1978. **53**: p. 238-56.

Laemmli, U.K., *Cleavage of structural proteins during the assembly of the head of bacteriophage T4.* Nature, 1970. **227**(5259): p. 680-685.

Lederer, F. et al, *Which mechanism for (S)-2-hydroxy acid-oxidising flavoenzymes? A tale of a hisitidine and two protons* in Flavins and Flavoproteins, 2005. (Nishino T., Miura, R., Tanakura, M., Fukui, K. ed) pp 193-204, ArchiTechInc., Tokyo.

Lederer, F., A. Belmouden, and M. Gondry, *The chemical mechanism of flavoprotein-catalysed alpha-hydroxy acid dehydrogenation: a mutational analysis.* Biochem Soc Trans, 1996. **24**(1): p. 77-83.

Lederer, F., *Extreme pKa displacements at the active sites of FMN-dependent alpha-hydroxy acid-oxidizing enzymes.* Protein Sci, 1992. **1**(4): p. 540-8.

Lederer, F., *Flavocytochrome b2*, in Chemistry and Biochemistry of Flavoenzymes, 1991. (Müller, F. ed); CRC Press, pp153-241, Boca Raton.

Lederer, F., *Sulfite binding to a flavodehydrogenase, cytochrome b2 from baker's yeast.* Eur J Biochem, 1978. **88**(2): p. 425-31.

Leferink, N.G., et al., *The growing VAO flavoprotein family.* Arch Biochem Biophys, 2008. **474**(2): p. 292-301.

Lehoux, I.E. and B. Mitra, *(S)-Mandelate dehydrogenase from Pseudomonas putida: mechanistic studies with alternate substrates and pH and kinetic isotope effects.* Biochemistry, 1999. **38**(18): p. 5836-48.

Lindqvist, Y., et al., *Spinach glycolate oxidase and yeast flavocytochrome b2 are structurally homologous and evolutionarily related enzymes with distinctly different function and flavin mononucleotide binding.* J Biol Chem, 1991. **266**(5): p. 3198-207.

Lu, X., et al., *3beta-Hydroxysteroid-delta24 reductase is a hydrogen peroxide scavenger, protecting cells from oxidative stress-induced apoptosis.* Endocrinology, 2008. **149**(7): p. 3267-73.

Luciani, P., et al., *Expression of the antiapoptotic gene seladin-1 and octreotide-induced apoptosis in growth hormone-secreting and nonfunctioning pituitary adenomas.* J Clin Endocrinol Metab, 2005. **90**(11): p. 6156-61.

Luciani, P., et al., *Expression of the novel adrenocorticotropin-responsive gene selective Alzheimer's disease indicator-1 in the normal adrenal cortex and in adrenocortical adenomas and carcinomas.* J Clin Endocrinol Metab, 2004. **89**(3): p. 1332-9.

Maeda-Yorita, K., et al., *L-lactate oxidase and L-lactate monooxygenase: mechanistic variations on a common structural theme.* Biochimie, 1995. **77**(7-8): p. 631-42.

Magnusdottir, A., et al., *Enabling IMAC purification of low abundance recombinant proteins from E. coli lysates.* Nat Methods, 2009. **6**(7): p. 477-8.

Malakhov, M.P., et al., *SUMO fusions and SUMO-specific protease for efficient expression and purification of proteins.* J Struct Funct Genomics, 2004. **5**(1-2): p. 75-86.

Marblestone, J.G., et al., *Comparison of SUMO fusion technology with traditional gene fusion systems: enhanced expression and solubility with SUMO.* Protein Sci, 2006. **15**(1): p. 182-9.

Massey, V., et al., *The reactivity of flavoproteins with sulfite. Possible relevance to the problem of oxygen reactivity.* J Biol Chem, 1969. **244**(15): p. 3999-4006.

Massey, V., *Introduction: flavoprotein structure and mechanism.* FASEB J, 1995. **9**(7): p. 473-5

Massey, V., *The chemical and biological versatility of riboflavin.* Biochem Soc Trans, 2000. **28**(4): p. 283-96.

Mattevi, A., *The PHBH fold: not only flavoenzymes.* Biophys Chem, 1998. **70**(3): p. 217-22.

Molecular cloning, a laboratory manual, ed. T. Maniatis, E.F. Frisch, J. Sambrook, 1982. Cold Spring harbor Laboratory, U.S.A.

Mowat, C.G., et al., *Altered substrate specificity in flavocytochrome b2: structural insights into the mechanism of L-lactate dehydrogenation.* Biochemistry, 2004. **43**(29): p. 9519-26.

Muller, F. and V. Massey, *Flavin-sulfite complexes and their structures.* J Biol Chem, 1969. **244**(15): p. 4007-16.

Mushegian, A.R. and E.V. Koonin, *A putative FAD-binding domain in a distinct group of oxidases including a protein involved in plant development.* Protein Sci, 1995. **4**(6): p. 1243-4.

Nadella, M., et al., *Structure and activity of the axon guidance protein MICAL.* Proc Natl Acad Sci U S A, 2005. **102**(46): p. 16830-5.

Norby, J.G. and M. Esmann, *The effect of ionic strength and specific anions on substrate binding and hydrolytic activities of Na,K-ATPase.* J Gen Physiol, 1997. **109**(5): p. 555-70.

Palfey, B.A. and C.A. McDonald, *Control of catalysis in flavin-dependent monooxygenases.* Arch Biochem Biophys, 2010. **493**(1): p. 26-36.

Palfey, B.A. and V. Massey, *Flavin-dependent enzymes.* In: Comprehensive Biological catalysis. Academic Press. 2008. pp 82-154

Pasterkamp, R.J. and A.L. Kolodkin, *Semaphorin junction: making tracks toward neural connectivity.* Curr Opin Neurobiol, 2003. **13**(1): p. 79-89.

Pasterkamp, R.J. and J. Verhaagen, *Emerging roles for semaphorins in neural regeneration.* Brain Res Brain Res Rev, 2001. **35**(1): p. 36-54.

Pasterkamp, R.J. and J. Verhaagen, *Semaphorins in axon regeneration: developmental guidance molecules gone wrong?* Philos Trans R Soc Lond B Biol Sci, 2006. **361**(1473): p. 1499-511.

Pasterkamp, R.J. and R.J. Giger, *Semaphorin function in neural plasticity and disease.* Curr Opin Neurobiol, 2009. **19**(3): p. 263-74.

Pasterkamp, R.J., et al., *Evidence for a role of the chemorepellent semaphorin III and its receptor neuropilin-1 in the regeneration of primary olfactory axons.* J Neurosci, 1998. **18**(23): p. 9962-76.

Pasterkamp, R.J., et al., *Expression of the gene encoding the chemorepellent semaphorin III is induced in the fibroblast component of neural scar tissue formed following injuries of adult but not neonatal CNS.* Mol Cell Neurosci, 1999. **13**(2): p. 143-66.

Pedretti, A., et al., *Homology modelling of human DHCR24 (seladin-1) and analysis of its binding properties through molecular docking and dynamics simulations.* Steroids, 2008. **73**(7): p. 708-19.

Pennati, A., et al., *Role of the His57-Glu214 ionic couple located in the active site of Mycobacterium tuberculosis FprA.* Biochemistry, 2006. **45**(29): p. 8712-20.

Rao, K.S. and F. Lederer, *About the pKa of the active-site histidine in flavocytochrome b2 (yeast L-lactate dehydrogenase).* Protein Sci, 1998. **7**(7): p. 1531-7.

Reid, G.A., et al., *Probing the active site of flavocytochrome b2 by site-directed mutagenesis.* Eur J Biochem, 1988. **178**(2): p. 329-33.

Sambrook, J., Russell, D.W., *Molecular cloning: A Laboratory Manual*. Third ed. 2001, Cold Spring Harbor, NY: Cold Spring Harbor Laboratory Press.

Schmidt, E.F., S.O. Shim, and S.M. Strittmatter, *Release of MICAL autoinhibition by semaphorin-plexin signaling promotes interaction with collapsin response mediator protein.* J Neurosci, 2008. **28**(9): p. 2287-97.

Schmidt, E.R., R.J. Pasterkamp, and L.H. van den Berg, *Axon guidance proteins: novel therapeutic targets for ALS?* Prog Neurobiol, 2009. **88**(4): p. 286-301.

Segel, I.H., *Enzyme kinetics*. 1975, New York: Wiley & Sons.

Sheely, *Glycerol viscosity tables.* Indusrial and engineering chemistry,1932. **24,** 1060-4

Siebold, C., et al., *High-resolution structure of the catalytic region of MICAL (molecule interacting with CasL), a multidomain flavoenzyme-signaling molecule.* Proc Natl Acad Sci U S A, 2005. **102**(46): p. 16836-41.

Sobrado, P. and P.F. Fitzpatrick, *Solvent and primary deuterium isotope effects show that lactate CH and OH bond cleavages are concerted in Y254F flavocytochrome b2, consistent with a hydride transfer mechanism.* Biochemistry, 2003. **42**(51): p. 15208-14.

Sobrado, P., S.C. Daubner, and P.F. Fitzpatrick, *Probing the relative timing of hydrogen abstraction steps in the flavocytochrome b2 reaction with primary and solvent deuterium isotope effects and mutant enzymes.* Biochemistry, 2001. **40**(4): p. 994-1001.

Suzuki, T., et al., *MICAL, a novel CasL interacting molecule, associates with vimentin.* J Biol Chem, 2002. **277**(17): p. 14933-41.

Tabacchi et al, *Ab initio molecular dynamics studies of flavocytochrome b2 reduction* in Flavins and Flavoproteins (Nishino, T., Miura, R., Tanokura, M., Fukui, K., eds) pp 281-287, ArchiTect Inc, Tokyo

Tabacchi, G., et al., *Does negative hyperconjugation assist enzymatic dehydrogenations?* Chemphyschem, 2007. **8**(9): p. 1283-8.

Tabacchi, G., et al., *L-lactate dehydrogenation in flavocytochrome b2: a first principles molecular dynamics study.* FEBS J, 2009. **276**(8): p. 2368-80.

Terman, J.R., et al., *MICALs, a family of conserved flavoprotein oxidoreductases, function in plexin-mediated axonal repulsion.* Cell, 2002. **109**(7): p. 887-900.

Urban, P. and F. Lederer, *Intermolecular hydrogen transfer catalyzed by a flavodehydrogenase, bakers' yeast flavocytochrome b2.* J Biol Chem, 1985. **260**(20): p. 11115-22.

van Berkel, W.J., N.M. Kamerbeek, and M.W. Fraaije, *Flavoprotein monooxygenases, a diverse class of oxidative biocatalysts.* J Biotechnol, 2006. **124**(4): p. 670-89.

Ventura, A. and P.G. Pelicci, *Semaphorins: green light for redox signaling?* Sci STKE, 2002. **2002**(155): p. pe44.

Waterham, H.R., *Defects of cholesterol biosynthesis.* FEBS Lett, 2006. **580**(23): p. 5442-9.

Waterham, H.R., et al., *Mutations in the 3beta-hydroxysterol Delta24-reductase gene cause desmosterolosis, an autosomal recessive disorder of cholesterol biosynthesis.* Am J Hum Genet, 2001. **69**(4): p. 685-94.

Wijnands, R.A., et al., *The importance of monopole-monopole and monopole-dipole interactions on the binding of NADPH and NADPH analogues to p-hydroxybenzoate hydroxylase from Pseudomonas fluorescens. Effects of pH and ionic strength.* Eur J Biochem, 1984. **139**(3): p. 637-44.

Williams, C.H., Jr., et al., *Methodology employed for anaerobic spectrophotometric titrations and for computer-assisted data analysis.* Methods Enzymol, 1979. **62**: p. 185-98.

Wolozin, B., *A fluid connection: cholesterol and Abeta.* Proc Natl Acad Sci U S A, 2001. **98**(10): p. 5371-3.

Xia, Z.X. and F.S. Mathews, *Molecular structure of flavocytochrome b2 at 2.4 A resolution.* J Mol Biol, 1990. **212**(4): p. 837-63.

Xia, Z.X., et al., *Three-dimensional structure of flavocytochrome b2 from baker's yeast at 3.0-A resolution.* Proc Natl Acad Sci U S A, 1987. **84**(9): p. 2629-33.

Zhou, Y., R.A. Gunput, and R.J. Pasterkamp, *Semaphorin signaling: progress made and promises ahead.* Trends Biochem Sci, 2008. **33**(4): p. 161-7